Theoretical study of the preparation of quantum degenerate mixtures for precision atom interferometry

Von der QUEST-Leibniz-Forschungsschule

der Gottfried Wilhelm Leibniz Universität Hannover

zur Erlangung des Grades

Doktor der Naturwissenschaften

- Dr. rer. nat. -

genehmigte Dissertation
von

Katerine Posso Trujillo

May 10, 2018

Referent: Prof. Dr. Ernst M. Rasel
Institut für Quantenoptik, Hannover, Deutschland
Korreferent: Prof. Dr. Reinhold Walser
Institut für Angewandte Physik, Darmstadt, Deutschland
Tag der Disputation: 13.11.2015

Zusammenfassung

In dieser Arbeit werden quantenentartete Gemische auf ihre Eigenschaften als Quellen für Präzisionsatominterferometer zum Test des Einsteinschen Äquivalenzprinzips untersucht. Um die notwendige Auflösung zu erreichen, sollen die Interferometriezyklen auf mehrere Sekunden ausgedehnt werden. Die bekannten Hauptbeiträge an systematischen Effekten, die bei realistischen Aufbauten auftreten, sind hierbei berücksichtigt, und für einige werden Strategien zur Unterdrückung präsentiert. Die Gemische die hier betrachtet werden, sind Bose-Einstein-Kondensate aus ^{87}Rb/^{85}Rb und ^{87}Rb/^{41}K. Eine simultane Absenkung der Expansionsraten beider Komponenten in den Temperaturbereich von weniger als 100 pK ist notwendig, um einerseits freie Entwicklungszeiten der Kondensate von 10 s zu ermöglichen, und andererseits systematische Fehler zum Beispiel verursacht durch die atomare Bewegung in den Wellenfronten der Lichtfelder zu unterdrücken.

Um diese Anforderungen erfüllen zu könnnen, wurde die Rolle der Wechselwirkung der Teilchen untereinander betrachtet, die von ihrer einfachen Durchstimmbarkeit mit Hilfe von Feshbach-Resonanzen profitiert. Neben der Manipulierbarkeit der Wechselwirkung wurden Delta-Kicks zur Kollimation untersucht, durch die der Einfluss der führenden systematischen Fehler unterdrückt wird. Neben dem oben genannten Gemisch wurden auch die Gemische ^{87}Rb/^{39}K und ^{87}Rb/^{170}Yb untersucht. Das ^{87}Rb/^{87}K-Gemisch wurde als Kandidat für Hochpräzisionsatominterferomtrie in Mikrogravitation identifiziert. Das Yb-basierte Gemisch hat den vorteil, dass die Wechselwirklung ohne zusätzliche Feshbachfelder durchgeführt werden kann. Für die Delta-Kicks wurde eine Vielzahl an Fallengeometrien untersucht, wie etwa die Dipolfalle, chip-basierte Potentiale, sowie das TOP-Fallenpotential (engl.: Time-Orbiting-Potential), um Majorana-Verluste zu verhindern. Die Berechnungen wurden mit Hilfe der Gross Pitaevskii Gleichung und Skalierungstheorie vorgenommen.

Schlagwörter: delta-kick-Kühlung, STE-QUEST, Äquivalenzprinzip Tests, Atominterferomtrie

Abstract

In this thesis, quantum degenerate mixtures have been studied for their use as source for precision atom interferometry operating over several seconds and employed for testing the Einstein's equivalence principle. The main leading systematic effects naturally emerging in realistic systems have been taken into account, for which some mitigation strategies have been presented. The main mixtures studied here are the condensed pairs of ^{87}Rb/^{85}Rb and ^{87}Rb/^{41}K which were proposed for space missions. A simultaneous reduction of the expansion rates to an ultra-low energy regime of less than 100 pK in both components is needed to achieve the targeted accuracy of 10^{-15}. To reach such a performance one has to consider the effects arising from the interparticle interactions. In our choices, however, they can be modified by exploiting Feshbach resonances. Besides the convenient tuning of interactions, therefore delta-kick collimation sequences have been efficiently applied reducing the impact of most leading systematic errors. Other mixtures studied are: ^{87}Rb/^{39}K and ^{87}Rb/^{170}Yb. The ^{87}Rb/^{41}K mixture has been identified to be most suitable candidate for high precision atom interferometry measurements in micro-gravity. The Yb-based mixture was found to be promising because the interactions are naturally matched. Moreover, the study covered a multitude of trap geometries for Delta-kick collimation such as dipole traps, chip based potentials to reach the low kinetic expansion energies required and to reduce systematic errors, as well as time orbiting potential traps to prevent Majorana losses. The calculations were carried out by solving the Gross Pitaevskii equations and by performing a generalization of a scaling theory for describing the dynamics of expanding condensates mixtures. Key words: BEC mixtures, delta kick collimation, STE-QUEST, equivalence principle tests, atom interferometry.

Key words: BEC mixtures, delta kick cooling, STE-QUEST, equivalence principle tests, atom interferometry.

Acknowledgements

My time as a PhD student at IQ has been greatly enriched by the help of some people. This is the opportunity to thank to people who have contributed to make this work possible.

Foremost I want to gratefully thank to Naceur for his guidance during these years, I appreciate his vast knowledge and his assistance in writing reports and the reading of the full document, I've learned a lot from him.

My sincere thanks also goes to Dr. Ernst M. Rasel for his support, my supervisor who provided me an opportunity to join his team.

For this dissertation I would like to thank my reading and oral defense committee members: Dr. Walser, Dr. Hammerer and Dr. Rasel.

Many thanks to Holger Ahlers for the valuable discussions and his continuous support during the time of this work.

I would also like to thank to Felix and Sebastian, the QPORT team for discussions about other topics in Physics.

I would like to acknowledge the useful interactions with Christian Schubert and for reading part of this thesis.

Thank you very much to Mrs. Faber, Mrs. Göldner-Pauer, Mrs. Pfenning, Mrs. Ohlendorf and Mrs. Thiele-Bode for their kind assistance.

I have to also acknowledge Felix, Peter, Victor, Vicente, Juan D and Logan for reading and criticizing different parts of this document, I appreciate their collaboration.

I thank to Dennis for the figure.

I would like to acknowledge the financial support from the Deutscher Akademischer Austauschdienst DAAD throughout my PhD studies, and for making the life of the granted students easier, a great organization. Special thanks goes to my referat Silke Hamacher, a very diligent, friendly and kind person.

A special mention deserves Victor. He has been my good friend. thanks a lot for the enriching discussions and the permanent support and encouragement that he has given me, and especially for make me laugh so much!.

Vicente for the long conversations about Physics, Politics and life, and the constant communication that we had on the phone and on my visits to Hamburg, thanks for being my friend.

Very special thanks to Matías B. everything started with him, a very special person and great physicist.

My friends in Colombia for making me always part of their lifes, Maria Elena, Edwin, Juan D and Boris, and around the world Luzka, Emerson, Juan and Laura. With that I got a necessary distraction.

I need to thank to my Colombian group in Hannover, this small group has been a source of friendship, thanks for the wonderful weekends, cooking, laughing, listening music, singing and sometimes dancing or talking about work.

Thanks to my friends in Berlin throughout the years for their support and distractions, really great moments we spent together.

Finally, I would like to acknowledge my wonderful family. My Mom the most important person in my life, my Dad, always supporting and motivating me. Viviana and Yamileth my great sincere company in the proper moments while being away from home and a different culture. And now I have to thank them in Spanish ...

Mil gracias a mi familia, en especial a mi madre por hacerme sentir la motivacion después de escucharla al teléfono, a mi padre por su constante apoyo, a mis hermanas Yamileth y Viviana por acompanarme via telefónica mientras caminaba sola de regreso a casa, a todos mis hermanos y hermanas por confiar siempre en mí, apoyarme y tenerme en cuenta al tomar decisiones a pesar de la distancia, a mis sobrinos y sobrinas por hacerme sentir esa alegría que siempre necesito, a mi tío y abuela por sus buenos deseos.

Contents

CHAPTER 1

Introduction

Atomic or molecular quantum degenerate gases constitute an exceptionally promising type of model systems allowing to simulate condensed matter systems. Since the first observations of Bose Einstein condensation in 1995 [1, 2], the creation and utilization of quantum degenerate gases has become a widely used technique to access the world of quantum many body physics [3], quantum information processing [4] or in researching in fundamental physics [5, 6, 7] (e. g. tests for effects on General Relativity).

Bose-Einstein condensation is a quantum phenomenon. Quantum mechanics asserts that all matter exhibits properties of both, particles and waves, as predicted by de Broglie [8]. Similarly as with light, such phenomena as atomic diffraction [9] and interference [10] can be observed. The wave-like nature makes it possible to develop matter wave interferometers [11] to obtain interference fringes whose phase is easily influenced by gravity, therefore offering a promising tool for a variety of precision measurements. The flexibility provided by cold atoms and Bose-Einstein condensates (BECs) makes them ideal for atom interferometry.

Bose-Einstein condensation was predicted in 1924, when S. N. Bose sent a paper in which he derived the Planck's law for black-body radiation to Einstein [12], who generalized that theory to a gas of identical particles with conserved number, predicting as well the multi-occupancy of the lowest quantum state, or ground state. More precisely, it was predicted that at low temperatures almost all the particles of a bosonic system would occupy the lowest quantum state when the wave functions of the particles, namely the order parameters, start to overlap. The atom wave functions overlap creating a macroscopic wave. The BEC appears when the temperature of a bosonic gas is lowered below a critical value, or its density is increased such that the corresponding de Broglie wavelength λ_{dB} increases ($\lambda_{dB} \sim T^{-1/2}$) reaching a point where it approaches the inter-particle mean separation at a critical temperature T_C.

The first Bose Einstein condensates in a dilute vapor of ^{87}Rb were experimentally produced in June 1995 in the group of Carl Wieman and Eric Cornell [1] in JILA. In the experiment a sample of ^{87}Rb atoms was cooled in a magneto-optical trap, then loaded into a magnetic trap and the very low temperatures reached by further evaporation. By removing the trap, the condensate was allowed to expand to be illuminated with laser light and then imaged. Also, in September 29, 1995, a BEC in sodium was observed for the first time in Ketterle's group [2].The advances reached in this field have provided the possibility to explore the world of quantum phenomena at macroscopic regimes. The discovery of BECs has been distinguished with the Nobel prize in Physics in 2001 [17, 18].

After the first realization of BECs, mixtures of condensates have attracted the attention of the increasing cold-atom community. In 1997, came the first experimental realization of mixtures with BECs of two hyperfine states, $|2,-2\rangle$, $|1,-1\rangle$ of ^{87}Rb in a magnetic trap, performed in JILA [20]. Several experiments have been done, using different hyperfine states of the same atom [21, 22, 23, 24, 25], different isotopes [26, 27], and different elements [28, 29, 30], or thermal mixtures of alkaline-earth with alkali metals [31]. Before long, and motivated by the first experimental realisation of a mixture of condensate, the first theoretical study of binary mixtures of BECs was published by Shenoy [32]. After Shenoy's publication, a large variety of theoretical studies with different approaches appeared, for instance, weak and strong phase separation have been observed (topological properties of ground and excited states, phase transitions) [33, 34, 35, 36, 37, 38, 39, 40, 41, 42, 43, 44, 45, 46] as well as fundamental quantum mechanics or collective excitations [47, 48, 49].

Since the condensates have relatively low densities, most of the theoretical studies have been based on an effective mean field theory which provides an accurate description of the static and dynamics of such systems. The appropriate model consists in a coupled set of Gross-Pitaevskii equations [50, 51, 52, 53] which are also called non-linear Schrödinger equations (NLS) [54]. The non-linearity in the NLS is set by a mean-field pseudo-potential which represents the two-body collisions, repulsive or attractive [55]. Condensates of large number of atoms with attractive interactions cannot be created [56], they would collapse at a certain density. For certain species, the interactions can be tuned to be repulsive by using the so-called Feshbach resonances.

The study on Fano-Feshbach resonances was done by Fano as suggested by Fermi [14, 15, 16] between 1935 and 1936. Independently, Feshbach reported about them in [57, 58]. The idea of using magnetic Fano-Feshbach resonances to tune interactions in ultracold atomic gases was first suggested in 1993 [60], and first experimentally demonstrated in 1998 [61]. Fano-Feshbach resonances in a condensate were experimentally observed in [59, 62, 63].

Feshbach resonances have opened new possibilities for ultracold-atom experiments, for instance, they have been used to create new single-component condensates [64, 65, 66]. Many of the experiments performed with mixtures, have benefited from Feshbach resonances to control the intra- or inter- species interactions and the collisional properties of the atoms to induce the appearance of a specific phase, relying on the particular research interests.

Besides the interest of theorists in multi-component condensates, these systems have a wide applications such as the realization of spinor condensates, quantum control protocols, or quantum many-body phenomena. In recent years, high-precision atom interferometry (AI) experiments have benefited from the ultraslow expansion and unique coherence properties [67] of BECs. Research with AI points to highly accurate tests of the weak equivalence principle.

The principle of atom interferometers is similar to that of optical interferometers [68], which were developed in the $19th$ century [69, 70, 71, 72]. The idea of AI was patented in 1973 [73]. Since then, the field of AI evolved quickly and several early demonstrations have been performed [74, 75, 76, 77]. A widely used configuration is the Mach-Zehnder geometry which was proposed between 1891 [78] and 1892 [79]. The first cold-atom based interferometer using stimulated Raman diffraction and laser cooled atoms was realized by Chu and co-workers[80] who used it to measure the acceleration of gravity.

The high precision of atom interferometry-based sensors makes them an exquisite tool for performing tests of fundamental theories [81, 82, 83, 84, 85, 86, 87, 88] as well as for a variety of applications such as metrology, geodesy or inertial navigation.

One timely challenge is to verify the weak equivalence principle (WEP) or universality of free fall (UFF) [89] by tracking the acceleration of two different testmasses in free fall using matter-wave interferometry [90, 91]. This experimental test [92] is important in the context of Grand Unification theory [93] to falsify some of the competing models, which predict a violation at different levels of the UFF [94, 95].

The simultaneous operation of a dual-species (or isotopes) atom interferometer (AI) was proposed [83, 96] to perform a WEP test with a precision going beyond the best reported values using classical bodies [97, 98]. The sensitivity of an atomic inertial sensor scales quadratically with the time spent by the atoms inside the interferometer [90] limiting ground-bound WEP tests [99, 100] and motivating the drive for long free expansions. Several platforms are therefore considered for such an increase, such as droptowers [101, 102], fountains [5, 103], parabolic flights [104] and spacecraft [105, 106]. An unprecedented sensitivity is expected when the interferometry time can be extended across seconds.

Recently, AIs fed with single-species Bose-Einstein condensates (BEC) [17, 18] were operated in long-time regimes [5, 6, 7] by taking advantage of the delta-kick collimation (DKC) technique [107, 108, 109] to reduce the expansion rates of the atomic cloud.

These demonstrations point towards a high-accuracy WEP test when combined with a second species in a differential atom interferometry measurement [110]. The source of such an interferometer would naturally be a binary atomic mixture.

Quantum mixtures of ultracold gases received a surge of theoretical [32, 39] and experimental [20, 21, 111] interest since the early years of BEC manipulation revealing extremely rich and interesting physics.

According to the motivation of this study, we consider dual-species quantum degenerate mixtures. Such systems yield very rich physics, where the interplay between the intra/inter-species interactions gives rise to different phases [34, 37, 112], and where a quantum test of the equivalence principle has been recently proposed [114, 115].

The aim of this work is to prepare ensembles of BEC mixtures with large number of atoms but able to stay compact after a long expansion time, and stable in the trap until expansion in spite of their attractive interactions. Such preparation may provide suitable quantum degenerate atomic sources to be used in precision atom interferometry experiments. To accomplish that, some topics have been selected to develop in this work, which give the following structure to this thesis:

In chapter 2 the necessary tools to theoretically treat a single-component BECs are presented. Here such a condensate is prepared for being a stable and compact source, suitable for measurements of long interrogation time. The chapter starts with a mathematical description of Bose Einstein condensates and some specific atomic species proper for being used in precision interferometry measurements are considered. The main purpose of this description is how to engineer compact and stable samples by following the dynamics of the ensembles. The condensates that have been studied are: ^{87}Rb, ^{85}Rb, ^{41}K, ^{39}K. Large condensates made of ^{85}Rb or ^{39}K have inherently attractive interactions, the interactions are then modified by using Feshbach resonances. For such systems, the static ground sate and dynamical properties are described. To guarantee the compactness of the samples, the delta-kick collimation technique is applied. The study has been extended to include more realistic trapping potentials, eg. time-averaged orbiting potentials and chip-based potentials for ^{87}Rb, the results are contrasted with the well known harmonic potential and the differences in ground state and time-expansion are detailed.

In chapter 3 the results for engineering optimal condensate mixtures are described in a general form. First, a theoretical description of the mean-field Gross Pitaevskii equations for mixtures of condensates is presented. Secondly we generalize a scaling theory which describes classically the dynamics of an atom cloud. This approach is important for making a preliminary control of the dynamics of the atomic cloud, it helps to choose quickly the proper DKC procedure applied to an ensemble. For each system studied, the resulting ground sates and dynamic properties of the following ensembles are discussed: ^{87}Rb/^{85}Rb, ^{87}Rb/^{41}K, ^{87}Rb/^{39}K, and ^{87}Rb/^{170}Yb. For the highly miscible interacting systems, such as ^{87}Rb/^{39}K, and ^{87}Rb/^{170}Yb, the Thomas Fermi ground state solutions are calculated. For the mixture ^{87}Rb/^{85}Rb, weakly and strongly interacting regime are considered. In all cases, the free expansion and the effect of delta-kick collimation are simulated. The miscibility and stability of the ensembles could be tuned thanks to the existence of the Feshbach resonances.

Chapter 4 is devoted to the application of the ensembles in precision atom interferometry to test for instance the universality of free fall, benefiting from the features found in the previous chapters 2 and 3. First, a brief discussion about the state of the art of tests of the weak equivalence principle is done, following with a presentation of the basic concepts of matter wave interferometry. The side effects of magnetic and gravity gradients on ^{87}Rb/^{85}Rb and ^{87}Rb/^{41}K ensembles are considered and the regimes where they are crucial, which account for a possible implementation in space-based measurements. Some of the results of the work appearing in chapters 3 and 4 are published in [105, 115, 116], and a more detailed presentation of the results is in preparation [117].

Finally in the Outlook, a compendium of results and a discussion of prospects for new calculations on completing the preparation of the atomic sources in AI are presented, this is: how to improve the efficiency on the delta-kick collimation procedure applied to single-component or binary BECs in realistic trap potentials. As well as including some corrections to the Gross-Pitaevskii equations to account for fluctuations due to the large

scattering lengths present in some ensembles.

In appendix A the calculation of the chemical potential of a miscible two-component mixture of BECs is shown which is crucial for the extension of the scaling approach used along this thesis, as well as for the employed calculation of the static ground state in the Thomas-Fermi approximation.

Another important intermediate calculation that has been used is the reduction of the GPE to a 1D problem for which the chemical potential is required, which has to be calculated, as presented in appendix B.

Finally, in appendix C an explanation of the numerical methods used to find the numerical solutions of the equations for obtaining the ground states and the expansion of the ensembles, these are the time step split operator method used to solve the GPE and the fourth-order Runge-Kutta employed to solve the coupled differential equations resulting from the scaling approach is done.

CHAPTER 2

Single-component BEC

The bosonic quantum field operators can be written according to Bose commutation relations

$$\begin{aligned}\left[\hat{\Psi}(\vec{r}'),\hat{\Psi}^\dagger(\vec{r})\right] &= \quad \delta(\vec{r}'-\vec{r}),\\ \left[\hat{\Psi}^\dagger(\vec{r}'),\hat{\Psi}^\dagger(\vec{r})\right] &= \quad [\hat{\Psi}(\vec{r}'),\hat{\Psi}(\vec{r})]=0\end{aligned} \tag{2.1}$$

For dilute gases considered here, the many body Hamilton operator is given by

$$\hat{H} = \hat{H}_0 + \hat{H}_{int}, \tag{2.2}$$

where

$$\hat{H}_0 = \int d^3\vec{r}\,\hat{\Psi}^\dagger(\vec{r})\left[-\frac{\hbar^2}{2m}\nabla^2 + V(\vec{r})\right]\hat{\Psi}(\vec{r}), \tag{2.3}$$

and

$$\hat{H}_{int} = \int d^3\vec{r}\,\hat{\Psi}^\dagger(\vec{r})\hat{\Psi}^\dagger(\vec{r})\; g\;\hat{\Psi}(\vec{r})\hat{\Psi}(\vec{r}). \tag{2.4}$$

The term $\hat{H}_0$ describes the system in absence of interactions. The first term is the kinetic energy, and the second term refers to the trapping potential.

The interacting hamiltonian is represented by $\hat{H}_{int}$ which describes the interactions due to collisions between the atoms, where the interaction strength is characterized by g. Those are dominated by s-wave scattering collisions $g = \dfrac{4\pi\hbar^2 a}{m}$, defined in terms of the scattering length a which can be tuned using the Feshbach collision resonances.In this very dilute regime, the effective range of the particle interactions is much smaller than the inter-particle spacing $|a| \ll a_{sep}$ or equivalently, $a \ll \rho^{-1/3}$, ρ being the spatial density determined from $\langle\vec{r}|\hat{\rho}|\vec{r}\rangle = \langle\hat{\Psi}^\dagger(\vec{r})\hat{\Psi}(\vec{r})\rangle = \rho(\vec{r})$.

When the trap is turned off, the gas expands rapidly, and the dynamics of the BEC can be followed by solving the time-dependent Gross–Pitaevskii equation (TD-GPE)

$$i\hbar\frac{\partial\Psi(\vec{r},t)}{\partial t} = \left(-\frac{\hbar^2}{2m}\nabla^2 + V(\vec{r}) + Ng|\Psi(\vec{r},t)|^2\right)\Psi(\vec{r},t) \tag{2.5}$$

This Gross-Pitaevskii equation is an essential tool to study the ground state and the dynamics of interacting condensates. [50, 51, 52, 53].

2.0.1 Thomas-Fermi approximation

When the number of particles in the gas is very large, the interacting term predominates and the GPE can approximately be solved by neglecting the kinetic energy term, and for a harmonic trapping potential, one arrives into the Thomas-Fermi approximation (TFA). It is a good approximation for highly repulsive interactions except close to the edges of the trap since the wave functions exhibit a Gaussian shape, and gives quick hints to infer the radius of the atomic cloud.

Then, neglecting the kinetic energy term in the GPE eq. (2.5), one finds

$$\Psi(\vec{r}) = \left[\frac{\mu - V(\vec{r})}{Ng}\right]^{1/2}, \tag{2.6}$$

where μ is the chemical potential, which for the system in 3D is well known it has the form:

$$\mu = \frac{\hbar\bar{\omega}}{2}\left(\frac{15Na}{a_{ho}}\right)^{2/5} \quad \text{, where } \bar{\omega} = (\omega_x\omega_y\omega_z)^{1/3} \tag{2.7}$$

$$\text{, and } a_{ho} = \sqrt{\tfrac{\hbar}{m\omega}} \tag{2.8}$$

Within the TFA, the extension of the cloud in a harmonic trap, $V(\vec{r})$ eq. (2.6) is defined by the boundary of the condensate, this is $\Psi = 0$, which is found to be

$$R_i^2 = \frac{2\mu}{m\omega_i^2}, \qquad i = x,y,z \tag{2.9}$$

and normalizing the wave function eq. (2.6), the size of the cloud eq. (2.9) is found to be

$$(R_xR_yR_z)^{1/3} = 15^{1/5}\left(\frac{Na}{\bar{a}}\right)^{1/5}, \qquad \bar{a} = \sqrt{\frac{\hbar}{m\bar{\omega}}} \quad \text{(harmonic length)}. \tag{2.10}$$

TFA is a good approximation for describing condensates with a very large number of atoms as will be seen in next section.

2.0.2 Scaling approach

If a BEC is subjected to a time-dependent external potential, eq. (2.11)

$$V(\vec{r},t) = \sum_{j=x,y,z}\frac{1}{2}m{\omega_j}^2(t)r_j^2. \tag{2.11}$$

the evolution of the gas within the TFA can be described by scaling the sizes of the condensate [128, 129] eq. (2.10) with a time-dependent scaling parameter which is derived using the following classical argument:

Consider a classical interacting gas with a spatial density ρ_{cl} in which each particle experiences a classical force eq. (2.12)

$$F_{cl}(\vec{r},t) = -\nabla\left(V(\vec{r},t) + g\rho_{cl}\right) \tag{2.12}$$

At $t = 0$ the gas is in equilibrium, and the condition $F_{cl} = 0$ is satisfied if the classical density ρ_{cl} can be replaced by the TFA $n_{TF}(\vec{r},t)$, thus classical and the quantum solution for the steady state density coincide in the Thomas-Fermi limit.

When $t > 0$ the gas starts expanding experiencing a dilation, this means all particles of the expanding cloud move along a trajectory given by

$$r_j(t) = \lambda_j(t) r_j(0) \quad j = x,y,z. \tag{2.13}$$

With this ansatz eq. (2.13) and substituting the force eq. (2.12) into the Newton's second law, the equations of motion for the particles are obtained

$$m\ddot{r}_j(t) = \frac{-\partial V(\vec{r},t)}{\partial r_j} - \frac{\partial g \rho_{cl}(\vec{r},t)}{\partial r_j} \tag{2.14}$$

The evolution of the density ρ_{cl} is obtained from the equation of the trajectory eq. (2.13)

$$\rho_{cl}(\vec{r},t) = \frac{1}{\lambda_x(t)\lambda_y(t)\lambda_z(t)} \rho_{cl}(\{\frac{r_j}{\lambda_j}\},0) \tag{2.15}$$

Substituting eq. (2.15) into eq. (2.14) we obtain the gradient $\nabla \rho_{cl}(t=0) = -\dfrac{\partial V(t=0)}{\partial r_j}$ at $t = 0$, implies

$$m\ddot{\lambda}_j(t) = \frac{-\partial V(\vec{r},t)}{\partial r_j} + \frac{1}{\lambda_j(t)\lambda_x(t)\lambda_y(t)\lambda_z(t)} \frac{\partial V(\vec{r},0)}{\partial r_j} \tag{2.16}$$

Inserting the trapping potential in eq. (2.17), one can write the trajectory eq. (2.13) as a solution of the equation of motion with the scaling parameters satisfying

$$\ddot{\lambda}_j(t) = \frac{\omega_j^2(0)}{\lambda_j(t)\lambda_x(t)\lambda_y(t)\lambda_z(t)} - \omega_j^2(t)\lambda_j(t) \tag{2.17}$$

The solution of these equations gives the evolution of the BEC, which are still not analytically solvable but far easier to solve than the TDGPE eq. (2.5).

2.0.3 Ground states and release dynamics

This work is mainly focused on preparing sources for precision atom interferometry experiments to test the equivalence principle[1], for which is necessary to first study systems consisting of single or two-component species of condensates at zero temperature. The first sample considered is a gas of ^{87}Rb in the $|F = 1, m_F = -1\rangle$ state, which is an alkali metal that due to its scattering properties [130] it is a natural choice for producing a stable condensate due to the repulsive interactions between its particles,because it is easily cooled at temperatures at the order of tens of nanokelvin. Being a gas with repulsive interactions, the ground state properties and the dynamics ^{87}Rb can be perfectly described by the theories presented in the first sections of this chapter. The solutions TD-GPE for a very large number of atoms allows one to obtain the wave function which is well approximated to the TFA solution. This makes possible to follow the dynamics with the classical equations obtained within the scaling approach.

Ground state of a BEC of ^{87}Rb

To find the ground state of our systems or equivalently the in-trap density profiles, the TD-GPE is numerically solved by using the time-Step Split Operator method (tSSO)

1 see Chapter 4

with the Fast Fourier transform (FFT), which are carefully described in Appendix C.

Lets calculate first the wave function in fig. 2.2 of the ground state of a quantum degenerate gas of $N = 10^6$ atoms of ^{87}Rb trapped in a spherically symmetric harmonic potential of frequencies $\omega_x = \omega_y = \omega_z = 2\pi \times 40$ Hz. The repulsive interactions are characterized by a scattering length $a = 99a_0 = 5.2383$ nm, with a_0 the Bohr radius.

For spherically symmetric potentials the GPE equations have been written in polar spherical coordinates[1] (lower dimensions) to simplify the calculations reducing notoriously the computation time. To test the feasibility of the dimension reduction of the equations, the results presented here are obtained from solving the 3D and 1D spherical TD-GPE.

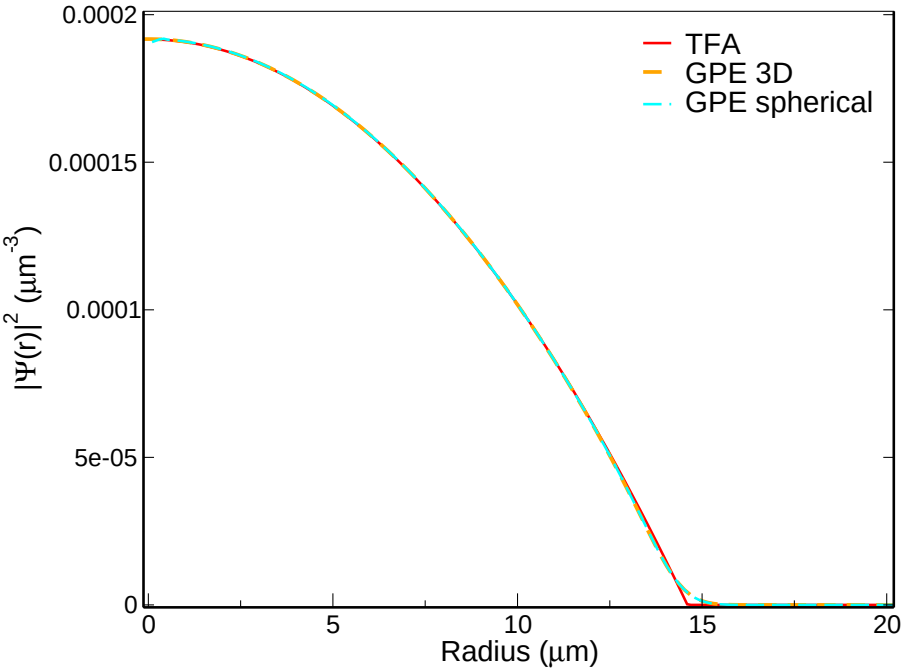

Figure 2.1: Comparison of results for ground state of $N = 10^6$ atoms of ^{87}Rb by solving the spherical coordinates GPE (cyan dashed line) and the full 3D GPE (green dotted line) and TFA (red solid line). The trapping frequencies are $\omega_x = \omega_y = \omega_z = 2\pi \times 40$ Hz.

Release dynamics of a BEC of ^{87}Rb

The ^{87}Rb can be used in environments that require a reduced size of the condensate after long expansion times, as it is required by the experiments that motivated this study. The evolution of the mean position of an outer particle in the gas is calculated as a function of time. For a standard expansion, at very long times, the TFA is not a good approximation to the condensate's wave function since the interactions have decreased sufficiently to make the dilution absolutely important, increasing the kinetic energy, therefore the scaling approach will not describe accurately the wave packet evolution, only numerics provide the exact wave function evolution.

1 For a well detailed deduction of the 1D dimension reduction of the problem see [**Adhikari2012**]

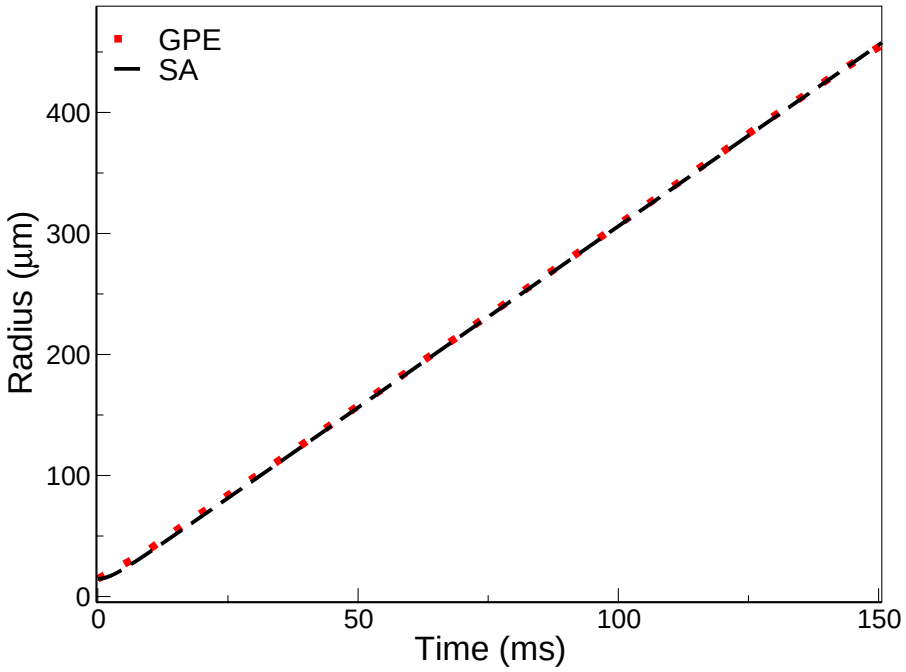

Figure 2.2: Short-time expansion of a BEC consisting of $N = 10^6$ atoms of ^{87}Rb released from a harmonic trap of frequencies $\omega_x = \omega_y = \omega_z = 2\pi \times 40$ Hz. The results by solving the spherical coordinates GPE (red dots), this is the radius of the solution of eq. (2.9), calculated as the evolution of $[\int r^2 |\Psi(r)|^2 dr]^{1/2}$, and the scaling approach (solid blue line), are contrasted showing a perfect agreement.

2.1 BECs with attractive interactions

2.1.1 Feshbach resonances

Feshbach resonances were experimentally observed in a condensate in 1998: [59, 63, 64, 65, 66] and in mixtures [62].

Lets consider two atoms having different states and inelastically colliding. The interaction between two neutral atoms is approximated by a Lennard Jones potential which has bound states. The atoms involved in such collisions can be in different internal states and there can be multiple channels contributing to the scattering potential, the entrance and closed channels (blue and black curve in fig. 2.3 respectively) are not the same. The scattering state is coupled to the last bound state of the potential.

A Feshbach resonance occurs when the energy of the bound state matches the kinetic energy of the two free atoms. Assuming the kinetic energy as finite, such a degeneracy happens only when the bound state lives in a potential that has a higher threshold energy than that of the colliding atoms. For the specific case of ultracold gases of alkali metal atoms which have low collision energy, one deals mostly with atoms in the GS, meaning that the entrance and closed channels are given by different hyperfine states, and the difference in energy of these states come from the different Zeeman shifts in an external magnetic field. Therefore it is possible to tune the closed channel into resonance with the entrance channel by changing the magnetic field.

When the colliding atoms are in the lower hyperfine state, the interatomic potential related to the higher hyperfine level has a bound state as it is shown by the thick red line in fig. 2.3

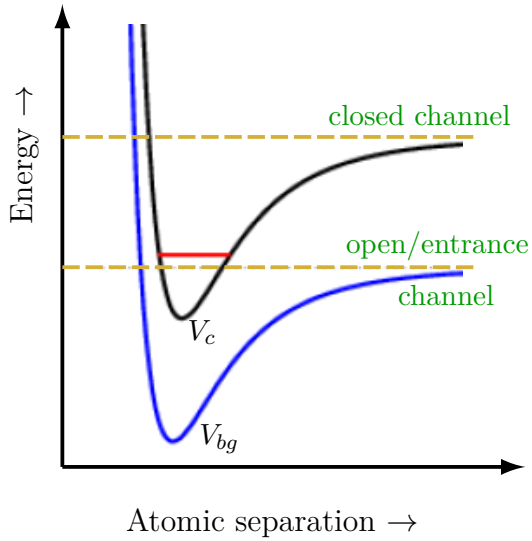

Figure 2.3: Interatomic potentials involved in a Feshbach resonance. Thick black and blue lines are the closed and open potentials as a function of the inter-atomic separation of the two colliding atoms. The threshold energies of the potentials are depicted as gold dashed lines. A bound sate in the higher potential is shown as a thick red line. The phenomenon occurs when two atoms colliding with energy E in the open channel are resonantly coupled to a molecular bound state E_c from the closed channel.

Fig. 2.3 depicts the potential energy as a function of the inter-atomic separation, on the left figure. The asymptotes are called collision channels, the red thick line indicating the bound state of the higher potential appears almost degenerate with the threshold energy of the lower potential. If the two atoms start a collision in the lower channel with kinetic energy much smaller than the energy separation of the two channels, the atoms are not able to exit the collision in the higher channel due to energy conservation. Therefore the higher channel is energetically "closed" while the lower is "open".

Making use of the tunability of the scattering length with changing the magnetic field, one induces a change of the character of inter-particle interactions from attractive to repulsive for the particular atoms: ^{85}Rb and ^{39}K as well as for reducing the strength of the the interaction between atoms of ^{41}K and ^{87}Rb. This dependence of the s-wave scattering length with the magnetic field B in the vicinity of the resonance has been found [62] to be

$$a(B) = a_{bg}\left[1 - \frac{\Delta B}{B - B_0}\right], \tag{2.18}$$

where a_{bg} is the background scattering length, associated with the last bound state in the entrance channel potential. B_0 is the position of the resonance and defines the magnetic field B at which the s-wave scattering length diverges. ΔB is the width of the resonance in magnetic field.

This is a procedure extensively used by the community of experiments on BECs to manipulate the interactions for the different species. There are other experimental procedures to tune the interactions by optical means proposed in 1996 [131, 132] and observed in 2000 [133], for experimental details of the procedure see e.g. the dissertation [134], this type of resonance would always be applied besides the magnetic resonances that can only be applied for specific atomic spin states.

Feshbach resonances of ^{85}Rb and ^{39}K

The systems considered in this work have interactions sufficiently strong for the formation of a condensate through evaporative cooling [1], and at the same time weak enough to be well described by the mean field theory. Interactions are crucial for the properties of the BEC, for instance in the spatial size of the condensate, in the contribution to the average energy per atom, or in deciding whether the condensate is stable or not, among others

In the case of ^{85}Rb, interactions can been tuned to a highly repulsive regime with

a scattering length $a_{85} = 900a_0$ reached with the application of $B \approx$158.8 G, since at B=0 G the scattering length is $a_{85} = -443a_0$. In a similar way it has been extracted the magnetic field needed to induce the repulsive interactions ^{39}K that initially has a scattering length $a_{39} = -33a_0$, To reach a scattering length of $a_{39} = 100a_0$ a magnetic field $B \approx$414.1 G has to be used.

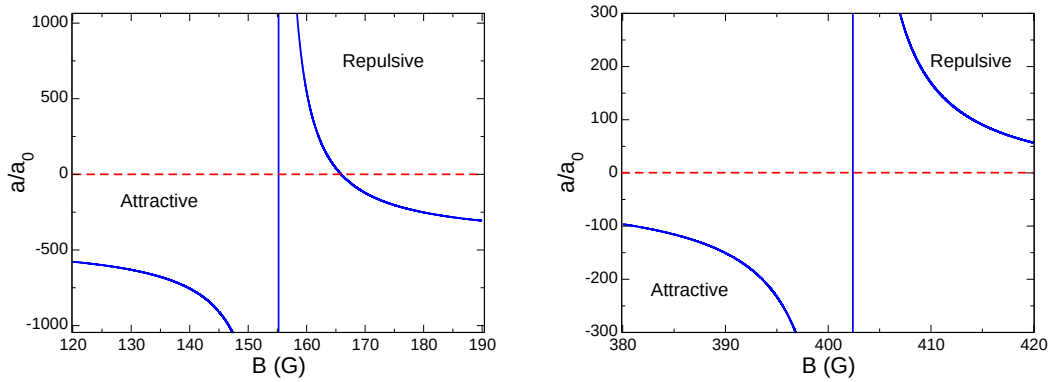

Figure 2.4: Feshbach resonances considered. Scattering length vs. magnetic field B. The figure on the left shows the broad resonance for ^{85}Rb which is around B=155 G, see [165]. The figure on the right is the Feshbach resonance for ^{39}K located at B=402 G, see [166].

2.1.2 Critical number of particles

A condensate having attractive inter-particle interactions tends to contract in order to minimize its energy. If the condensate is put in a magnetic (or optical trap) there comes to play an additional energy which is the zero-point kinetic energy which competes with the attractive interaction trying to spread out the condensate and preventing it from collapse. For this energy to win, it should necessarily be larger than the interactions, which is not always possible; for strong interactions, their effect cannot be compensated by such a kinetic energy. In that case, the collapse is avoided only if the number of atoms does not exceed a certain critical value which was found by Ruprecht et *al.* [135] as being

$$N_{cr} = k\frac{\bar{a}}{|a|} \tag{2.19}$$

where $\bar{a}$ is the harmonic oscillator length, $|a|$ is the absolute value of the scattering length, and k is a dimensionless parameter which for a spherically symmetric trap, has been found [136] $k = 0.5746$.

For the particular trap used, for ^{85}Rb with a trapping frequency $\omega_{x,y,z} = 2\pi \times 40$ Hz this critical number of atoms is $N_{cr} = 103$ atoms, and ^{39}K and frequencies $\omega_{x,y,z} = 2\pi \times 11.95$Hz, is $N_{cr} = 3813$ atoms.

If the number of atoms exceeds the critical value, the condensate is not metastable anymore and the density increases at the center of the trap minimizing the interaction energy. The contraction produced in the density can be balanced for a gas with sufficiently weak attractive interactions, or by having a gas small enough. Such cases are depicted in fig. 2.5.

This exemplified case for a small number of ^{85}Rb gas however is a general expected behavior of the density in terms of interactions. Beyond these conditions, the kinetic energy is not able to compensate the attractions and the condensate is forced to collapse to minimize the energy, resulting in several successive isotropic contractions and expansions

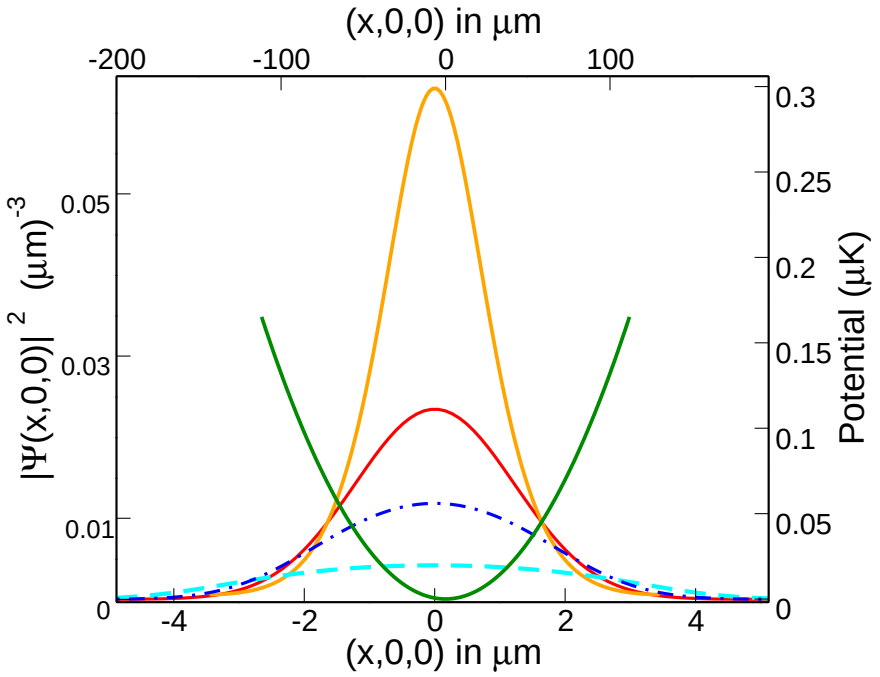

Figure 2.5: Harmonic trapping potential and density profiles as a function of position. A condensate consisting of $N = 10^3$ atoms of ^{85}Rb is trapped in a spherically symmetric harmonic potential (green solid line) of frequencies $\omega_{x,y,z} = 2\pi \times 40Hz$. A non interacting BEC has a Gaussian-like density profile (red solid line), the same BEC turning the interactions to repulsive with a scattering length $a_{85} = 44a_0$ exhibits a broader spatial density (blue dashed line), by increasing the interactions in the repulsive regime, $a_{85} = 300a_0$ the density gets much broader(cyan dashed line) and by turning the interactions to attractive to a value of $a_{85} = -30a_0$ (yellow line) it is possible to appreciate the increasing in the peak density as a consequence on the accumulation of particles in the central region.

around the center, at the peak density. This phenomenon can be understood taking into account that when the peak density gets very high, the inelastic collisions become important inducing losses by two-body dipolar collisions and three-body recombination processes [132]. First the condensate shrinks as a consequence of the negative pressure resulting from the fact that the kinetic energy is lower than the attractive interaction energy. The subsequent explosion is provoked by the kinetic energy gained due to the atomic losses, becoming larger than the interaction energy. Collapse and explosion were experimentally observed in ^{85}Rb by Donley in 2001 *et al.* [64].

2.1.3 Stable BECs at long expansion time at $B = 0$

By using a similar criterion of energy compensation as that used to determine the critical number of atoms of eq. (2.19), now during the dynamics of an initially repulsive BEC one can extract a critical size of the condensate to continue evolving in a stable regime although the Feshbach magnetic field that tuned the interactions is removed leaving the interactions again attractive.

A system of (^{85}Rb atoms is prepared in the hyperfine state $|F = 2, m_F = -2\rangle$) or ^{39}K, in which under a homogeneous bias magnetic field the interactions are now strongly repulsive, and the condensate is in a safe region where no collapse will occur. But it is not necessary to keep the magnetic field permanently on during the time of flight evolution; after achieving the repulsive regime, the Feshbach field can be turned off, and

the condensate will evolve in a repulsive regime.

To find the time when the magnetic field has to be put off, the simple energy criterion proposed is as follows: at the moment of removing the magnetic field, the kinetic energy should be greater than the mean field energy,

$$\mu - U_{MF} - V_{trap} > U'_{MF} \tag{2.20}$$

U_{MF} is the condensate mean field energy with the Feshbach field on (scattering length $a > 0$) and U'_{MF} (scattering length $a' < 0$) is the condensate mean field energy with the Feshbach field off with a strength of the interaction given by g', these are:

$$U_{MF} = \frac{2gN}{\pi^{3/2}(\lambda(t)R_0)^3} \qquad U'_{MF} = \frac{2g'N}{\pi^{3/2}\left(\lambda(t)R_0\right)^3} \tag{2.21}$$

R_0 is the in-trap initial radius of the condensate. Then the time-dependent radius of the cloud as:

$$\lambda(t)R_0 > \left[\frac{2N\left(|g| + |g'|\right)}{\pi^{3/2}\left(\mu - V_{trap}\right)}\right]^{1/3} \tag{2.22}$$

with $\lambda(t)R_0$ being a classical determination of the increasing in time of the size of the condensate that is going to be detailed in sect. 2.1.5. Thereby to estimate the time is straightforward. These estimations have been done for the two attractive samples considered.

It is interesting to observe how all contributing terms of the energy behave during these regimes, since they are used to predict the time of a safe removal of the magnetic field preventing the system to undergo in collapse. These are shown in fig. 2.6 for ^{85}Rb and in fig. 2.7 for ^{39}K.

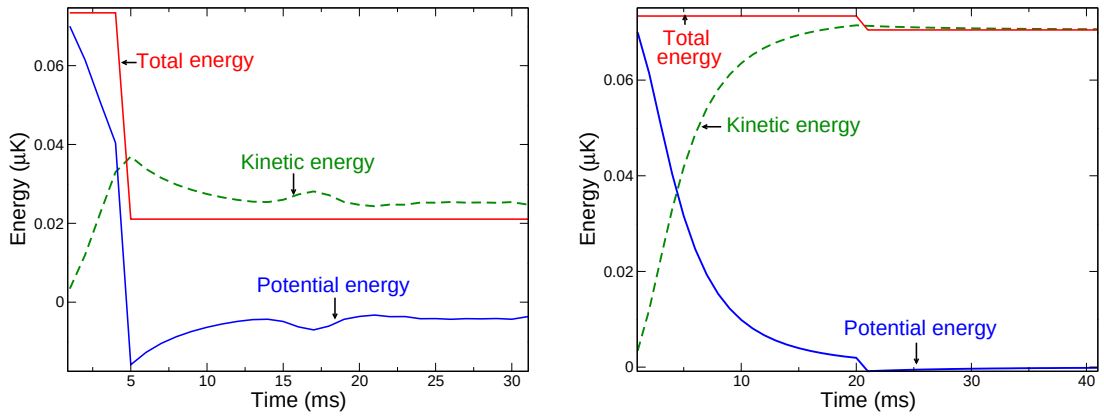

(a) Shutting off the magnetic field at t=4 ms. **(b)** Shutting off the magnetic field at t=20 ms.

Figure 2.6: Evolution of energy terms in a cloud of $N = 10^6$ atoms of ^{85}Rb,a spherically symmetric harmonic trap of frequencies $\omega = 2\pi \times 40.0$ Hz has been used. Fig. (a) is showing the effect of shutting off the magnetic field at $t = 4$ ms. In fig. (b), the magnetic field is left for $t = 20$ ms allowing the condensate to be stabilized in spite of the attractive interactions observed in the conservation of the energy.

A similar analysis is valid for both systems (^{85}Rb and ^{39}K), fig. 2.6(a) and fig. 2.7(a) show the "unsafe“ regime at times earlier than the threshold for stability calculated from eq. (2.22), the kinetic energy (green dashed lines) are not able to compensate the

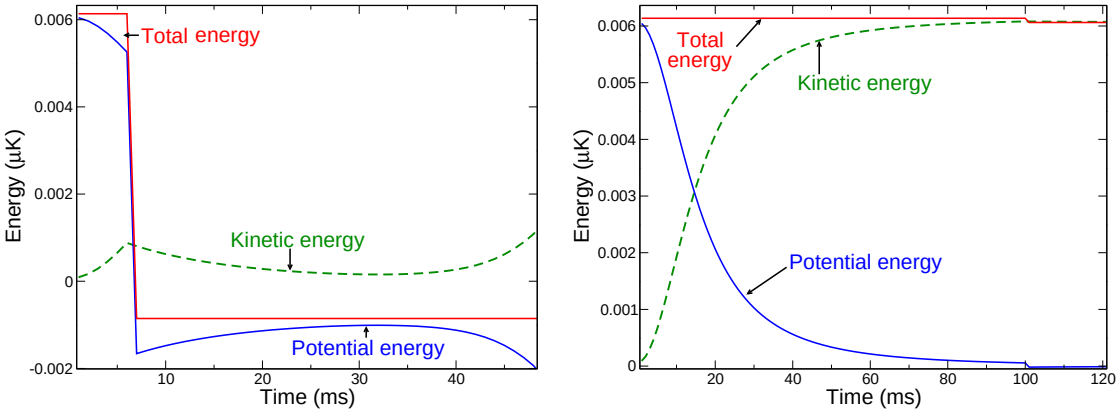

(a) Shutting off the magnetic field at t=6 ms.

(b) Shutting off the magnetic field at t = 100ms.

Figure 2.7: Evolution of energy terms in a cloud of $N = 10^6$ atoms of ^{39}K, a spherically symmetric harmonic trap of frequencies $\omega = 2\pi \times 11.95$ Hz has been used. Fig. (a) is showing the effect of shutting off the magnetic field at a time t=6 ms, before the predicted one. It is clear from the red line that the total energy is far from being conserved. Fig. (b) is showing an stable regime where the total energy is conserved.

the strength of the attractive interaction energy (blue solid lines) before shutting the magnetic field off at t=4 ms and at $t = 6ms$ for ^{85}Rb and ^{39}K respectively. There can be seen a dramatic loss of the total energy (red solid lines).

The systems are stable at zero magnetic field after $t = 20$ ms (^{85}Rb) and $t = 100$ ms (^{39}K) as can be seen from the conserved total energy (red solid lines) in fig. 2.6(b) and fig. 2.7(b)

The necessity of leaving the magnetic field on for longer times in ^{39}K compared to ^{85}Rb can be understood from the ratio between kinetic and interaction energies, which is higher in ^{39}K, and the system will need more time to gain the sufficient kinetic energy to compensate the attractive interactions.

The time for having stable BECs can be extracted directly observing at the moment of the kinetic energy overcomes the attractive interaction in fig. 2.6(b) and fig. 2.7(b) which corresponds to that obtained from eq. (2.22). All results obtained can be corroborated by the survival curves shown in what follows fig. 2.8(a) and fig. 2.8(b).

Based on the discussion at the beginning of this section, the treatment of an attractive BEC without the inclusion of loss terms can lead to a nonlinear diffusion instead of the expected wave propagation. This is marked by the non conservation of energy which is a signature of the alternating collapses and explosions occurring in an attractive self-interacting BEC.

Different timings for shutting off the magnetic field B have been considered in fig. 2.8, the duration of the magnetic field on where ^{85}Rb and ^{39}K BECs are observed to be stable are t= 10 ms and t= 100 ms respectively. The results coincide with the relations between the kinetic and interaction energy and the total energy conservation in fig. 2.6 and fig. 2.7.

2.1.4 Stable ground state of ^{85}Rb and ^{39}K

For analyzing the appropriateness of using such attractive gases is necessary first of all to find the ground state density profiles by solving the GPE identically to the previous case of ^{87}Rb.

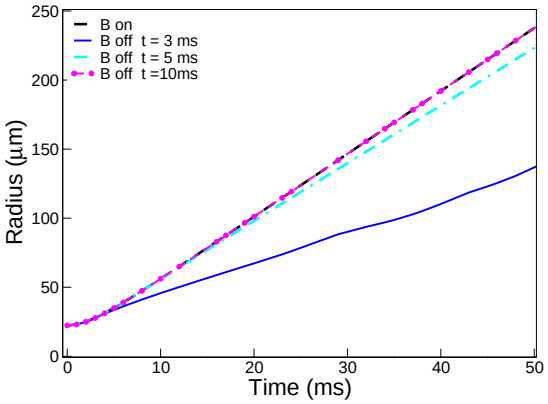

(a) Determination of minimum stability time for a BEC of ^{85}Rb.

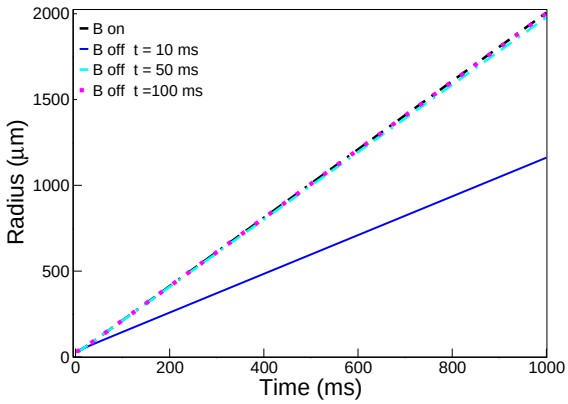

(b) Determination of minimum stability time for a BEC of ^{39}K.

Figure 2.8: Expansion curves for different timings of shutting off the Feshbach field. The time of removing the magnetic field B for leaving a stable BEC (perfect overlap with that of having B permanently on) are t= 10 ms (^{85}Rb) and t=100 ms (^{39}K)

A gas of ^{85}Rb with 10^6 atoms is trapped in a spherically symmetric harmonic potential of frequencies $\omega = 2\pi \times 40$ Hz. For $N = 10^6$ atoms of ^{39}K in a harmonic trap with frequencies $\omega = 2\pi \times 11.95$ Hz which is not highly attractive at B=0 G, but still not possible to condense for such a large number of particles.

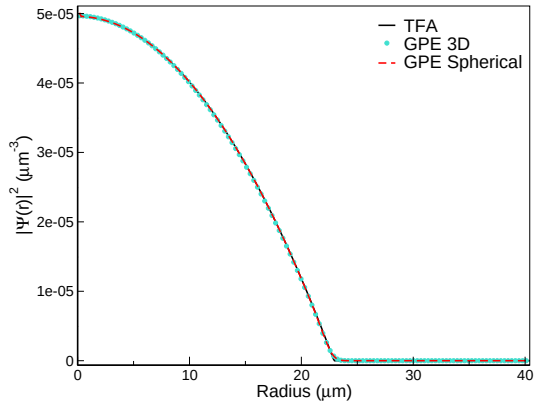

(a) ^{85}Rb. B= 158.8 G.

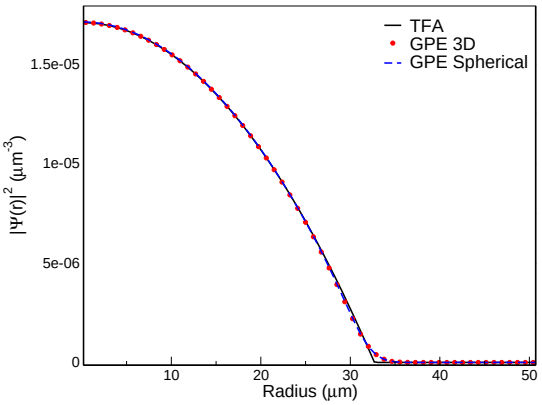

(b) ^{39}K. B≈ 415 G.

Figure 2.9: Ground state of $N = 10^6$ atoms each case with repulsive interactions. Comparing results obtained by solving GPE in 3D and spherical coordinates with the approximated TF.

Compared to the previous analyzed case of ^{87}Rb, the magnitude of the mass of ^{85}Rb isotope is close to ^{87}Rb but ^{85}Rb has been chosen more strongly repulsive making the cloud wider. In the case of ^{39}K the scattering length has been tuned in the same way as for ^{87}Rb, which occupies a larger space as an effect of it smaller mass. These effects are all important making the choice of one sample over the other depending on other factors that will be discussed in Chapter 3.

Having guaranteed that the gases will be stable during the entire time of flight by having controlled the interactions via Feshbach resonances, I proceed to study the dynamics.

2.1.5 Free expansion and magnetic lens effect on BECs

An interacting BEC initially in a trap potential is suddenly released to freely expand for long time. After a long-time expansion, the condensate reaches a large size which may surpass the typical sizes of the chamber containing it, making necessary to control the expansion. There are different strategies to achieve it, these are for example to adiabatically reduce the potential strength for which it requires a long time to fulfill the adiabaticity condition or to suddenly remove the trap potential whose efficiency has been experimentally demonstrated [6, 7] without the restriction to meet the adiabatic criterion, this is the well known delta kick cooling technique [107] which will be outlined below.

Delta kick cooling technique (DKC)

In 1997 Ammann *et al.*[107] presented a technique for cooling the atoms far below the photon recoil temperature by narrowing the momentum distribution with the application of a subsequent pulsed potential to the atoms, a similar technique is implemented to an ensemble of atoms by using a magnetic or optical field to produce the impulse which will significantly lessen their velocity standard deviation meaning a temperature reduction at the nK regime and prevent the cloud to reach a large size. The narrowing of the velocity standard deviation is achieved with the manipulation of the phase-space density.

The description is going to be presented in one dimension, but it can be extended to 3D. Initially, at time $t = 0$ the BEC trapped in a harmonic potential $U(\mathbf{r}) = \sum_i^N \frac{1}{2} m\omega_i^2 \mathbf{r}_i^2$ of angular frequency ωAt $t = 0$ the trap is removed, and for a later time, $t > 0$, the condensate is allowed to freely expand during a time T after which the trap is pulsed on again during a very short time $\delta(t - T)$. As an effect of the pulse, each atom experiences a momentum kick or quick force which depends on position as $(F \propto -dU/dx)$ to the atoms, their momentum will change by $\Delta p \propto dU/dx \propto -m\omega^2 x\delta(t - T) \propto x \propto p$.

$$F(x) \cdot \delta(t - T) = -\frac{\partial U(x)}{\partial x} \cdot \delta(t - T) = -m\omega^2 x \cdot \delta(t - T) \tag{2.23}$$

In phase space A classical gas initially trapped by a potential $U(x)$ expands, and atoms having different momentum will move away from the center of the trap. During the expansion, a correlation between position and momentum develops $\Delta p \propto x$ as shown in eq.2.23. After a long enough time when the interactions are lessening and the momentum p varies linearly with x, $p = mx/T$, showing that the distribution in position get stretched.

By using such a harmonic-like potential which gives a kick $\propto x$, this will produce a larger force on an atom the further it is from the center of the trap, these atoms are precisely the ones with the highest speeds. By this fact, a kick produced by a harmonic-like potential can lead to all atoms have a speed close to zero.

The rms velocity decreases by a factor x_i/x_f producing a temperature reduction of $(x_i/x_f)^2$, where x_i and x_f are the sizes of the cloud at the moment of starting the kick and after a total expansion time respectively. The cooling reached with the application of such a kick can be schematically understood from the phase-space density.

The simple classical explanation given above coincides with a quantum mechanical description. Starting with an initial wave packet on the ground state $\Psi(x)$ created in $U(x)$ which is suddenly shut off, the subsequent broadening of $|\Psi(x)|^2$ (see fig. 2.10 (a)) is governed by the time evolution operator $U_T = exp\left[-i\hat{p}^2 T/2m\hbar\right]$. After some free expansion, the phase of $\Psi(x)$ is proportional to x^2.

By giving a kick to the wave packet, the $x-$ distribution maintains its original width, and the effect of the harmonic kick corresponds to rotating the phase space volume back onto the position axis, in this way lowering the expansion temperature; by Liouville's theorem, the area of the phase space stays constant during the free expansion as well as when the kick is applied, giving

$$x_f v_f = x_0 v_0 \quad \therefore \quad v_f = v_0 x_0 / x_f, \tag{2.24}$$

which means that the longer the cloud is allowed to freely expand before applying the kick, the narrower the final distribution is in momentum, leading to lower temperatures T due to the relation $\frac{1}{2}k_B T = \frac{1}{2}mv^2$. The effect of the kick in the phase space is sketched in fig. 2.10 (b).

In real-space, $\phi = m\omega^2 \delta t x^2 / 2\hbar^2$. The spatial dependence of this phase is analogous to the phase factor that acquires a field due to the presence of a lens, see for instance, [137]. It is also possible that the kick applied is strong enough to be used to counteract the motion of the atoms, this is the case shown in fig. 2.10 (c).

Matching the phase acquired by the system during free expansion to that gained by applying DKC, gives $\Delta x \Delta p \sim \hbar/2$; in contrast with the broadening of $|\Psi(x)|^2$ by a factor, the $|\Psi(p)|^2$ gets narrower by the same factor, therefore the energy will reduce by the square of this factor, lowering in this way the temperature. The DKC technique is widely used in this thesis. To study the effect of DKC on the expansion of atomic clouds of for instance: ^{87}Rb, ^{85}Rb, ^{41}K and ^{170}Yb, numerical simulations are performed by two methods. The first one is by solving the TD-GPE eq. (2.5) with tSSO method for real time (see Appendix C, and the second one is the coupled differential equations describing the scaling approach eq. (2.17). For the regime of interactions used in this work (scattering lengths much shorter than the interparticle separation), collision rates have been considered as negligible.

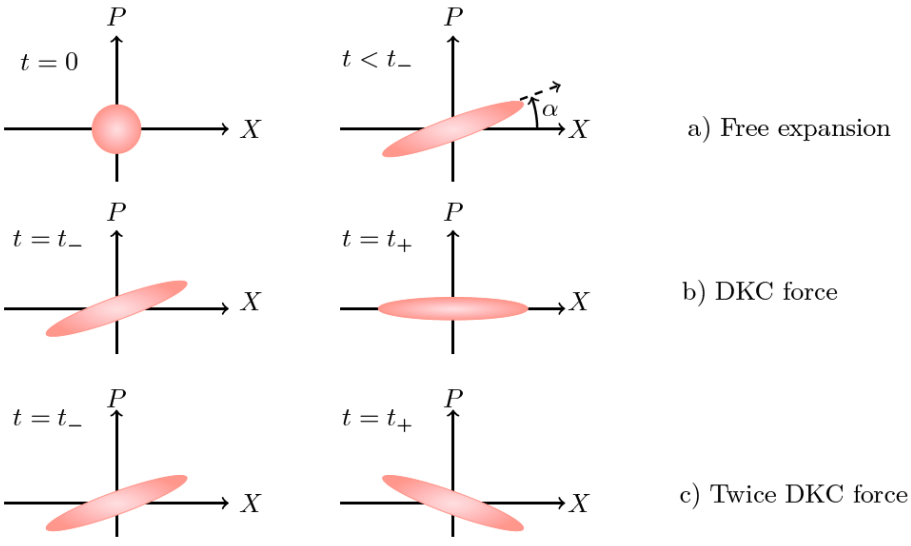

Figure 2.10: Use of a linear kick force to squeeze. successive steps of free evolution (a) followed by the application of a DKC (b), and doubling the strength of the DKC to counteract the motion of the atoms (c), analogous to focusing an optical beam.

An analogy to Gaussian optics To make the effect of a DKC more easily understandable a description similar to [138] is presented here. A light source is located at the focal point of a convex lens, the light passing through the lens is collimated along the x-direction fig. 2.11(a), by increasing the power of the lens which is inversely proportional to the focal length, without changing the position of the lens nor that of the light source, the beams crossing the lens will go to a focal point effecting the light starts expanding again, as in fig. 2.11(b).

But on the contrary, if the power is reduced, the light will expand more. The kick given to an atomic cloud by a DKC can be considered as a lens for atoms which will collimate in time, unlike the $x-$direction in the case of light, therefore the radius of the expanding cloud will remain constant.

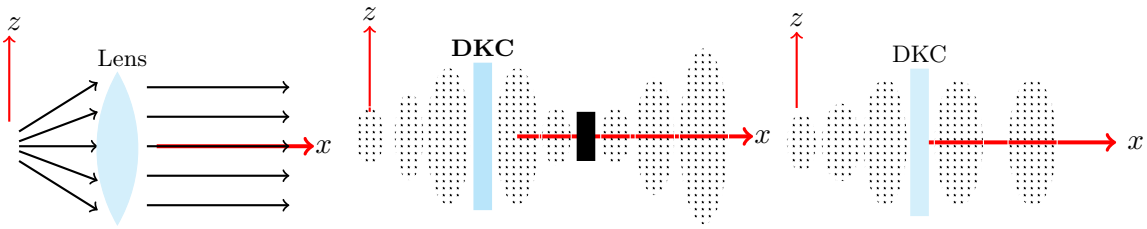

(a) Beam collimated. Beam's waist located at the focal point.

(b) Atomic cloud passing through a focus. A too strong DKC is applied.

(c) Atomic cloud collimated. Atom's expansion is stopped by DKC.

Figure 2.11: Analogy between the effect of a DKC applied to an atomic cloud and a collimating lens on a light source. In (a) a light beam's waist is located at the focal point. Light beam is no longer expanding in $z-$direction after passing through the lens. (b) shows a cloud kicked too hard. The velocity (and temperature) of the atoms increase after passing through a focus. (c) shows an atomic cloud expanding in $z-$direction with time before DKC is applied. After DKC the cloud's expansion is stopped.

2.1.6 DKC on ^{87}Rb

When the trap is suddenly switched off at t=0, it is still remaining the interaction energy (mean field energy) which gives rise to the expansion of the atomic gas, i.e., this potential energy is transformed into kinetic energy of the particles, after some time all this mean field has been transformed as can be seen in the right side in fig. 2.6 and fig. 2.7 making the condensate expanding linearly in time.

With DKC technique it is possible to produce several effects, when it is applied at the proper timing and the right duration, it is possible to highly collimate the cloud as can be seen in the black line of fig. 2.12, or on the other hand, one is able to produce the opposite effect by applying DKC for a long time to make the cloud reach a focal point, and consequently diverging to a large size as is the case of the red dashed line. In addition, to reduce the expansion of the condensate even more by waiting a longer time to re trap the atoms, as it is the particular case depicted in the dashed blue line fig. 2.12 being unfeasible in most high precision measurements due to the the large size of the cloud at the moment of re trapping which largely surpasses the dipole trap capabilities, in this case the DKC can be improved if a multi-lensing method is used.

By the reasons explained above, it has been chosen the application of DKC at a starting time $t^{start} = 48.0\ ms$ and with a duration of t_{dur}=0.302 ms. In this case the expansion of the condensate is notoriously reduced as it is expected, since the role of the pulse is to take out a considerable part of the kinetic energy reducing the expansion rate of the gas.

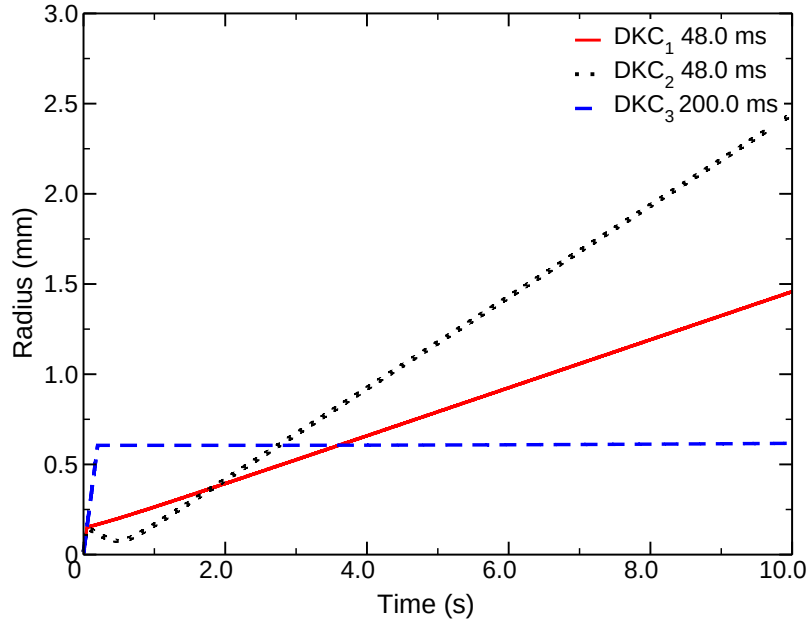

Figure 2.12: DKC regimes in ^{87}Rb. $N = 10^6$ atoms are being re-trapped (DKC) at different times and with with different durations effecting the reduction or the increment of the size of the expanding cloud. The red dashed line describes the case when the DKC is applied during t_{dur}=0.34 ms, starting at $t^{start} = 48.0$ ms, the black line is for a DKC duration of t_{dur}=0.302 ms starting at same time as previous case, and the flattening effect shown in dashed blue line is produced by waiting longer time to start applying DKC, this time is $t^{start} = 48.0$ ms and with a duration of t_{dur}=0.077 ms.

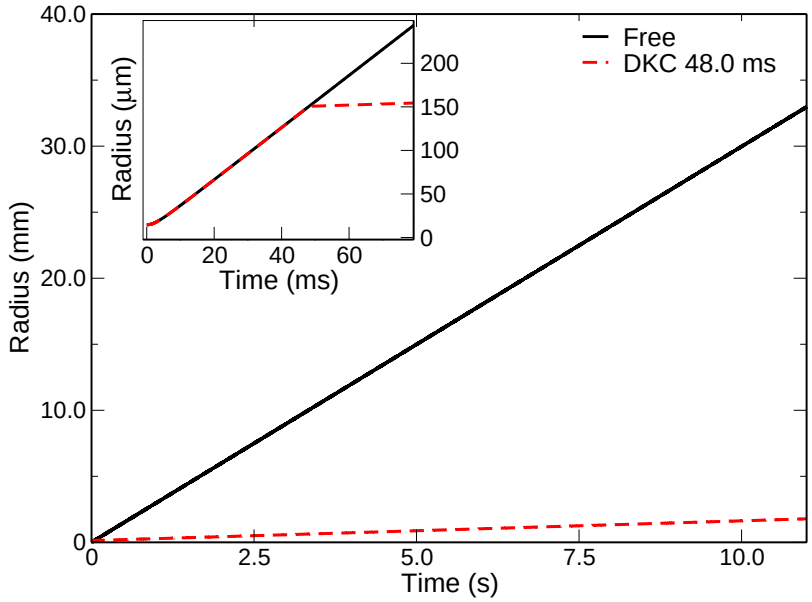

Figure 2.13: Radius of the long-time expanding $N = 10^6$ ^{87}Rb atoms including the application of DKC. The black line corresponds to a free expansion and the red line has the effect of DKC applied after 48 ms of expansion, with a short duration of 0.302 ms. The inset is a zoom of the first 150 ms of expansion showing clearly the effect of the DKC procedure. The frequencies of the DKC traps as well as the initial trap are $\omega = 2\pi\times40$ Hz.

In fig. 2.13 one can see the good agreement of the two approaches which originates from the fact that we are considering large ensembles for which the interactions play an important role, giving validity of the neglecting of the kinetic energy assumed in the TFA implicit in the SA. Additionally due to the fact that the duration of the DKC is not sufficiently long to destroy the condensate, it remains as gaussian-shaped which can be approximated for long expansion times to the parabolic shape proper of the TFA.

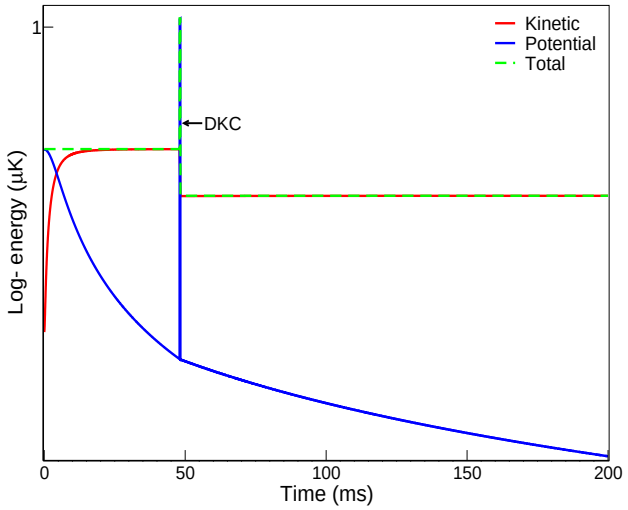

Figure 2.14: Effect of DKC on the energy of an expanding cloud of ^{87}Rb. After releasing the atoms the kinetic energy start increasing at expenses of the reduction of the interactions and the sudden switch-off of the trap. After some fixed time the atoms are re trapped during a short time by suddenly switching on the trap, increasing the potential energy and removing most of the kinetic energy. The potential energy here is the sum of the trapping potential and the inter-atomic interactions.

The atoms expand slowly and isotropically as a consequence of the kinetic energy gained which can be observed in the expansion and energy curves above in fig. 2.14. This is also easily appreciated in the zoom in shown in the inset of fig. 2.13 .

In the description of the condensate, interactions play an important role in observing not only the steady state but in the dynamics too. It can be tricky computationally, since they modify the momentum distribution in this way: repulsive interactions produce a broadening of the wave function in real space and therefore a narrowing in reciprocal space making the grid needed to calculate big enough to scan the total space occupied by the gas, but also fine enough to respect the requirements of the reciprocal space.

2.1.7 DKC on ^{85}Rb

The same operating regime of DKC and trap configuration done for ^{87}Rb is utilized in the highly interacting ^{85}Rb with scattering length $a = 900a_0$.

Unlike what happens in ^{87}Rb, here the strong interactions produce a larger size of the condensate, but it is not more difficult to control the expansion with DKC, since it is usually applied when the gas is moving uniformly.

2.1.8 Multiple pulse and anisotropic traps

Experimental realizations may require the use of anisotropic traps which makes the collimation of an atomic cloud equally efficient in all directions extremely difficult to reach. The anisotropic trap that is being discussed here consists of a harmonic trap with different strengths in all directions. More confined directions are more easily collimated, leaving the DKC almost having no effect on the cloud in the less confined direction. Applying a DKC procedure with a long duration is needed in order to collimate in the weaker direction causing the size and speed of the cloud in the stronger confined direction increase abruptly, simulating the effect of a focus in an optical lens. For these situations is required to apply a multiple-pulse DKC.

The time-evolution of the radius in the three spatial directions of a condensate created

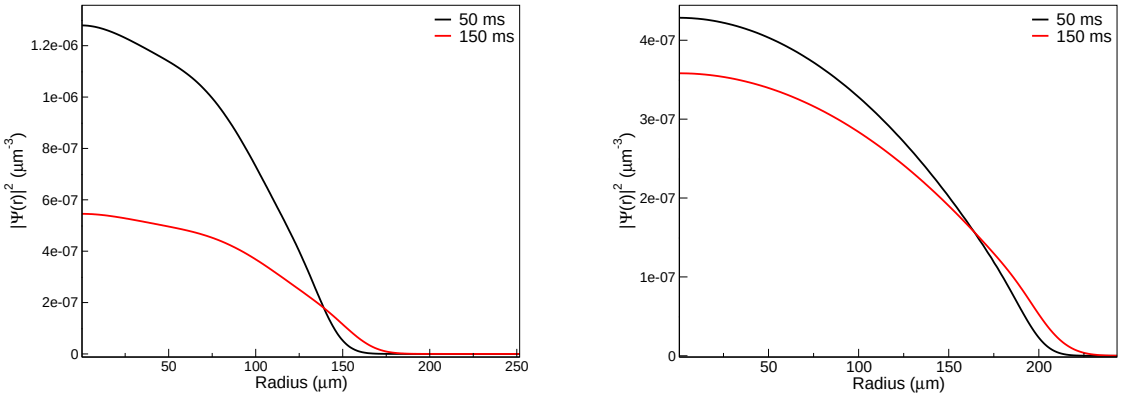

Figure 2.16: Density profiles at different expansion times, with DKC procedure of fig. 2.17. A Feshbach field is hutted off at 10 ms, showing the stability predicted from the energy curves. The calculation is carried out in spherical coordinates. The black line shows the condensate expanded 2 ms after applying DKC, the red line shows the expansion 100 ms after DKC, at which the condensate keeps nearly the same size.

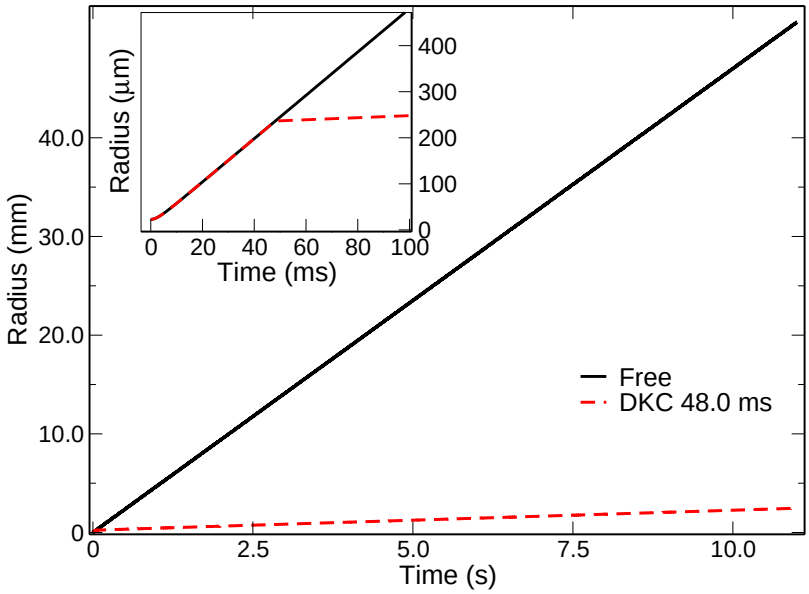

Figure 2.17: Radius of the expanding 10^6 ^{85}Rb atoms, free expansion and DKC. The interactions are tuned to repulsive with a scattering length $a = 900a_0$. The black line corresponds to a free expansion and the red line corresponds to the same trap and DKC configuration as in ^{87}Rb. The inset is a zoom of the first 100 ms of expansion.

and DKC subjected in a anisotropic harmonic trap is depicted in fig. 2.18(a). The more weakly confined direction (x) in red is possible to be collimated only with a strong DKC pulse, which in this case has been applied at t_1^{start}=68.5 ms during t_{dur}^1=5.76 ms but while doing this, the other two directions go into the analogous of a focal point, causing the sizes and the expansion rates to reach very large values, requiring to be re-trapped for a second time, this has been done at t_2^{start}=240.0 ms during t_{dur}^2=1.528 ms, producing the desired collimation and the reduction of the expansion rates to a very low values as shown in fig. 2.18(b).

The atoms start expanding freely when released from the trap until reaching a constant speed (1), auspicious to apply the first pulse, the motion of the atoms in all directions gets reversed (3) due to the very strong DKC, corresponding to what has been described

in sect. 2.1.5. After such a fast expansion (3), greater than had atoms before applying DKC, the atomic speed gets constant (4) and finally is dramatically lowered (5) due to the application of a less stronger DKC.

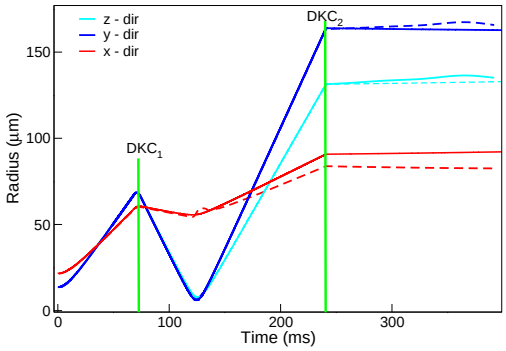

(a) Time-evolution of the radius. Green vertical lines indicate the times when DKC was applied.

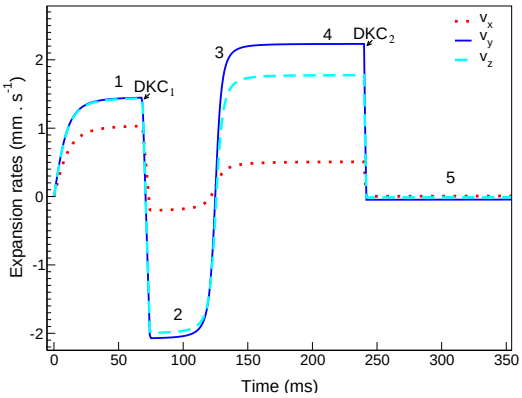

(b) Expansion rates.

Figure 2.18: A BEC consisting of $N = 10^6$ atoms of ^{87}Rb prepared in an anisotropic harmonic trap of frequencies $(\omega_x,\omega_y,\omega_z) = 2\pi \times (7.56,12.01,11.88)$ Hz is subjected to the following two-pulse DKC sequence: t_1^{start}=68.5 ms, t_{dur}^1=5.76 ms, t_2^{start}=240.0 ms t_{dur}^2=1.528 ms. In (a) solid lines show the scaling approach results and the dashed lines are for the numerical solution of GPE in all three directions, the times when the DKC pulses are applied are indicated with vertical green lines. The effect of DKC on the expansion rates is shown in (b) with the same colors for the three directions as in (a).

Another way of observing the dramatic changes in the dynamics of the cloud as an effect of the application of strong pulses can be done by calculating the σ_v-velocity standard deviation curves in all directions which is shown in fig. 2.19. When the atomic cloud released the trap $\sigma_v = \langle v^2 \rangle - \langle v \rangle^2$ increases reaching a constant value until the first long-duration DKC is applied at t_1^{start}=68.5 ms which introduces a sharp reduction of σ_v. At the subsequent free expansion the atoms have a constant velocity, which is lost with the application of the second pulse effecting initially a fast expansion to continue moving slowly, leaving the system in a very low temperature regime, and low velocity.

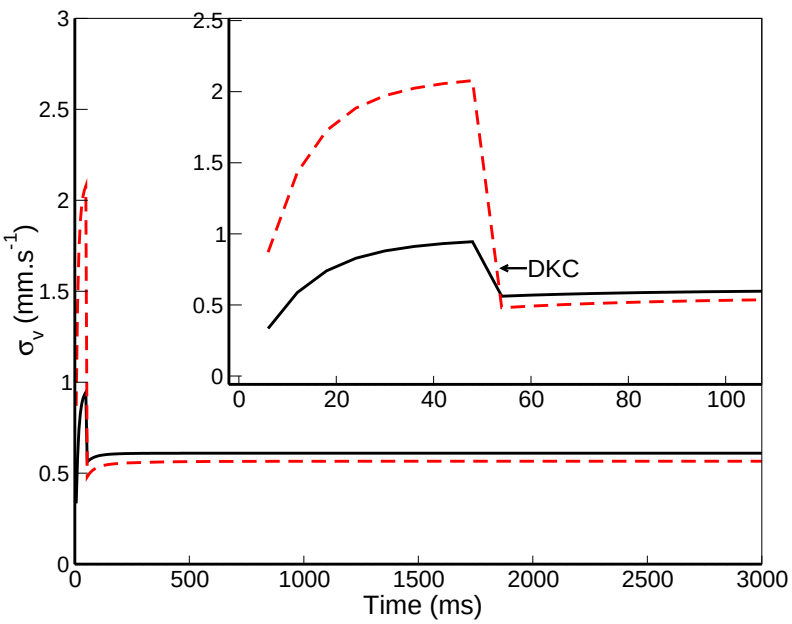

Figure 2.19: The σ_v-velocity standard deviation of a condensate cloud of $N = 10^6$ atoms of ^{87}Rb in an anisotropic harmonic trap of frequencies $(\omega_x,\omega_y,\omega_z) = 2\pi \times (7.56,12.01,11.88)$ Hz subjected to the two-pulse DKC sequence: t_1^{start}=68.5 ms, t_{dur}^1=5.76 ms, t_2^{start}=240.0 ms t_{dur}^2=1.528 ms.

2.2 Approaching realistic traps

Most features of a quantum gas as density, size, energy and phase space density are highly dependent of the trapping potential (frequencies and geometry) which makes it essential to make a choice for the kind of traps used.

In this section I discuss some of the trapping procedures going beyond harmonic traps.

Aside from the optical dipole trap used which is approximated by Gaussian profiles, it has been studied the atomic gases trapped in microscopic magnetic traps on chips [139], and in time-averaged orbiting potentials [140, 141, 142].

First, it is presented the physical principles of each of them in order to understand the ground state and the dynamics features emerging for the condensates.

2.2.1 Optical dipole traps

The use of Optical dipole traps (ODT) for trapping atoms was originally introduced by Letokhov [143], who proposed that the atoms might be trapped at 1D at the nodes or anti-nodes of a standing wave with a large detuning from resonance. Shortly after, in 1970 Ashkin [144] demonstrated the trapping of particles with lasers combining the action of radiation pressure and dipole forces. Since their appearance, ODT are widely used in experiments of cold atoms. Some of them are found in [65, 145, 146, 147, 148, 149].

The fundamental principle of optical dipole trapping is based on the momentum transfer from photons to the atom by the electric dipole interaction with far detuned light. An atomic gas with a higher refraction index than its surrounding medium is shined with a light beam which produces a bending of the light when it passes through it inducing a change in momentum. This refraction results in a net force that makes the target move to the center of the trap [150].

The depth of the trap is determined by the shift of the energy of the system due to the field. Typical depths reached in ODT are less than 1 mK. Optical trapping is a powerful tool in the context of Feshbach resonances since as it is understood from sect. 2.1.1 is desirable to have a uniform magnetic field in the vicinity of the resonance which is non-achievable with magnetic traps. It must be understood that the BECs of this study

are produced in dipole traps unless something else is specified as it will be seen below in this section.

See for more details, e.g. [150, 151, 152, 153], or for a qualitative explanation [**ucsd**].

Ground state and Dynamics of a system of $N = 10^6$ atoms of ^{87}Rb in a Dipole trap

In fig. 2.20(a), a dipole trapping potential is compared to a harmonic trap with the corresponding frequency in a fully spherical symmetry, these frequencies are $\omega_{x,y,z} = \omega = 2\pi \times 31Hz$. Harmonic potentials have been used to simulate experimentally implemented trapping potentials, such an approximation seems to work very well for obtaining the ground state density profiles (see fig. 2.20(b)), as well as for freely propagating the wave-packet of a system of $N = 10^6$ condensed atoms of ^{87}Rb.

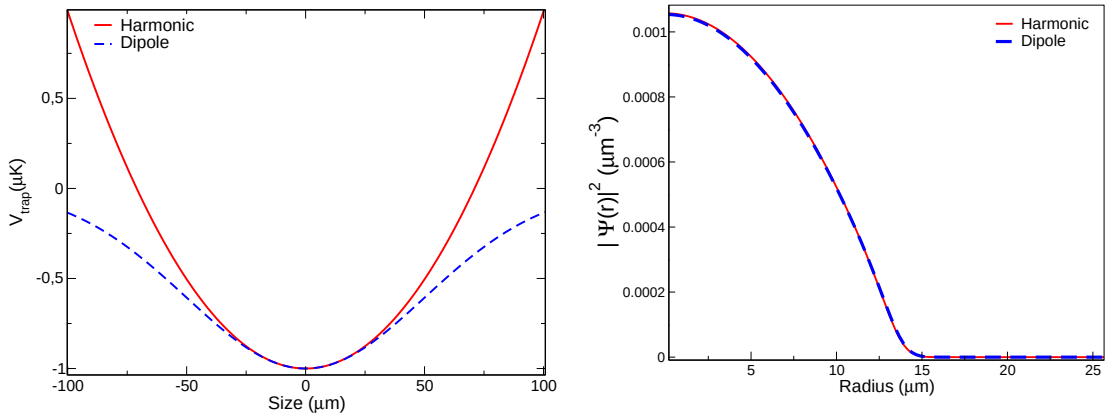

(a) Optical dipole trap and Harmonic trap potentials.

(b) Ground state density profiles.

Figure 2.20: An optical dipole trap is shown by the dashed blue line, the red solid line corresponds to the harmonic potential in fig. 2.20(a). Matching of the ground state density profiles of a system of $N = 10^6$ condensed atoms of ^{87}Rb prepared in a dipole trap (red dashed line) and in a spherically symmetric harmonic trap (solid blue line) in 2.20(b). The trapping frequencies $\omega = 2\pi \times 31$ Hz.

The nearly perfect matching of the time-evolution of the radius in free expansion by preparing the system in a harmonic trap (blue solid line) and in a dipole trap (blue dashed line) which are exactly super-imposed as shown in fig. 2.21 is due to the fact that the ground sate wave function at time $t = 0$ is sufficiently narrow to be completely located in a small region of the traps where both of them are parabolic-shaped. The density profiles for this situation after a time t=100 ms of evolution are shown in fig. 2.21.

The free expansion of the wave function after a total time of 100 ms with the two trapping potentials match very well as can be observed in fig. 2.22

When a DKC procedure is applied, the shape of the trapping potential strongly influences the geometry of the expanding wave packets, this is clear from fig. 2.21. At the moment of applying DKC, whenever the size of the cloud is large enough to allow the condensate explore the characteristic wings of the dipole potential, the geometry of the density profiles is affected by such wings (see red and green lines). However, if the DKC is applied at early times and with a short duration (cyan lines), the condensate should expand more similarly to as being trapped by a harmonic potential. The studied cases are for three equal effective DKC at meaningful starting times, these are: t^{start}=10.0 ms during t_{dur}=1.25 ms (radius of the cloud < beam waist), t^{start}=35.8 ms during t_{dur}=0.805 ms (radius of the cloud < beam waist) and t^{start}=48.0 ms during t_{dur}=0.302 ms (radius of the cloud < beam waist). The time-evolving density profiles at different

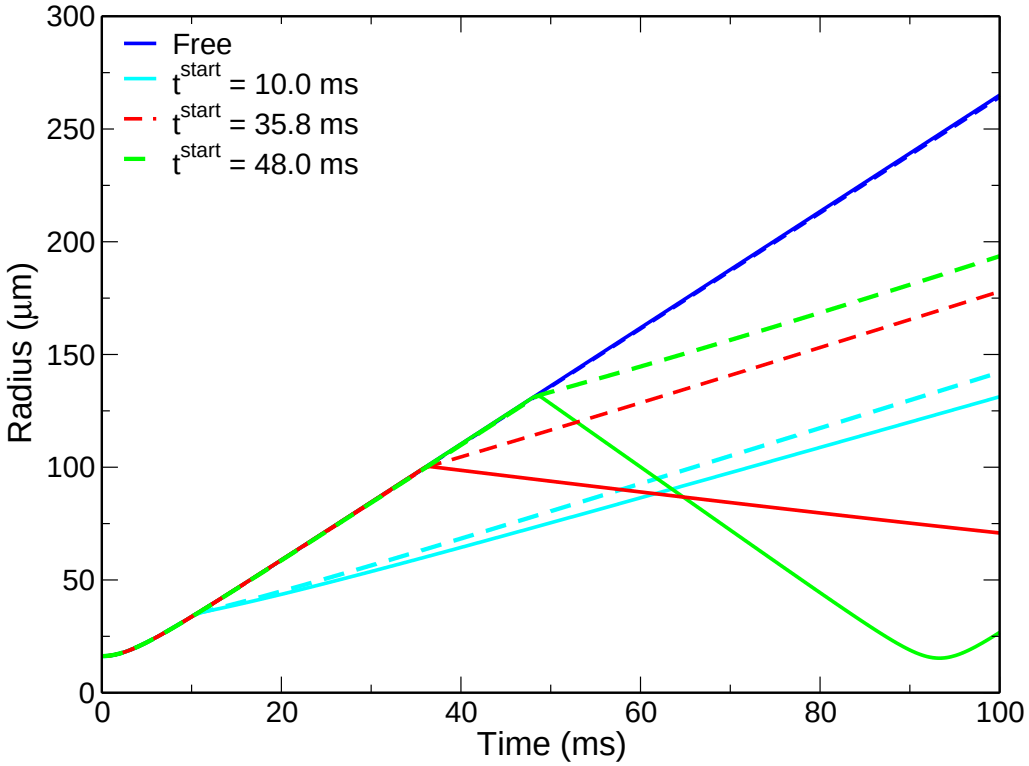

Figure 2.21: Time-evolution of a condensate cloud of $N = 10^6$ atoms of ^{87}Rb in a dipole trap (dashed lines) and in a harmonic trap (solid lines). When the system goes in free expansion, the time-evolution of the radius perfectly overlap (blue lines). A DKC procedure applied at t^{start}=48.0 ms during t_{dur}=0.32 ms (red lines) shows the discrepancies by trapping with the two potentials. By applying a DKC at t^{start}=10.0 ms during t_{dur}=1.25 ms the evolutions are more comparable.

times is shown in fig. 2.23. When the DKC starts (t =10 ms), the wave functions (blue curves) coincide with each other. Such wave functions somewhat differentiate from each other at times t =50 ms (red curves) and t=100 ms (cyan curves), and the shapes are similar.

As a conclusion, it is worth noticing that the expansion of the cloud subject to DKC is very different in the harmonic and dipole potential cases. Moreover, the later the DKC pulse ia applied, the larger the cloud is and the more prominent the effect of anharmonicities is.

2.2.2 Magnetic traps

The principle of magnetic traps relies on the dependence on the dipole moment of the state-dependent force in an inhomogeneous field $\vec{B}$ [154]. The magnetic traps used which are mainly static, are variations of Ioffe-Pritchard trap. They have basis in the coupling $U = -\hat{\vec{M}} \cdot \vec{B}$ between the atomic magnetic moment operator $\hat{\vec{M}}$ and the magnetic field $\vec{B}$. They operate in a regime where $\hat{\vec{M}}$ of the atoms is aligned with $\vec{B}$ and follow adiabatically the direction of $\vec{B}$ during the atomic motion; leading to $|\vec{\mu}|B$, where $\mu =$ is the projection of the magnetic moment operator, which is a constant depending on the atomic Zeeman sublevels.In the quantum picture,the projection of the magnetic momentum of an atom on a given axis is quantized and can be expressed $\mu = m_F g_F \mu_B$ where g_F is the Landé factor. m_F the magnetic quantum number or the hyperfine magnetic sub-level and μ_B is

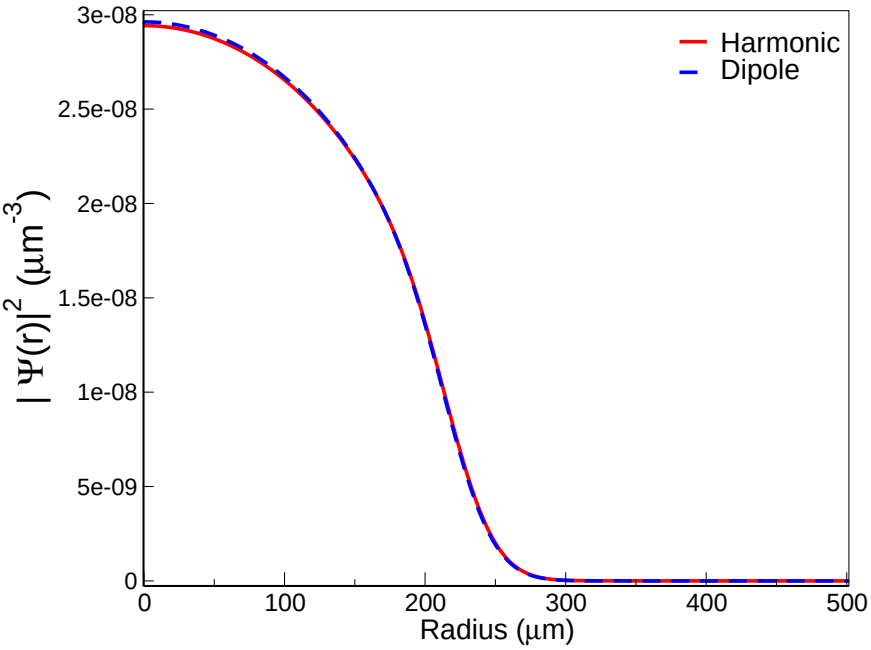

Figure 2.22: Density profiles of the free expansion corresponding to the blue lines of fig 2.21. When the system expands freely, the wave functions for a ground state initially prepared in a dipole (dashed blue line) and in a dipole trap (red solid line) are perfectly superimposed.

the Bohr magneton. The energy is written now

$$|\vec{\mu}|B = m_F g_F \mu_B |\vec{B}| \tag{2.25}$$

Depending on m_F, the atoms will be attracted or repelled from a magnetic field extrema (minimum or maximum). However static magnetic field maxima are forbidden by Maxwell's equations in free space (see for instance [155], so that only low-field seekers can be trapped in the minima of the magnetic field. This low field seeker is not the lowest state, the system does not suffer spontaneous decay, spin-changing collisions that induce decay and trap losses.

Typically these traps reach depths of about 100 mK. This trapping mechanism has strong limitations due to the fact that it depends on the internal atomic states therefore the trapping geometries are bounded to the use of arrangement of coils. One of the simplest magnetic traps is the Quadrupole trap.

Quadrupole traps

Quadrupole traps use two co-axial coils configured as an anti-Helmholtz pair, in which the magnetic field vanishes at some point. By considering an axial symmetry about z-direction, and a magnetic gradient B' along the x and y axes, and a gradient along z-axis is -2B' ($\nabla \cdot \vec{B} = 0$).The magnetic field created is

$$\vec{B} = B'\,(x, y, -2z)\,; \qquad |\vec{B}| = B'\left(x^2 + y^2 + 4z^2\right)^{1/2} \tag{2.26}$$

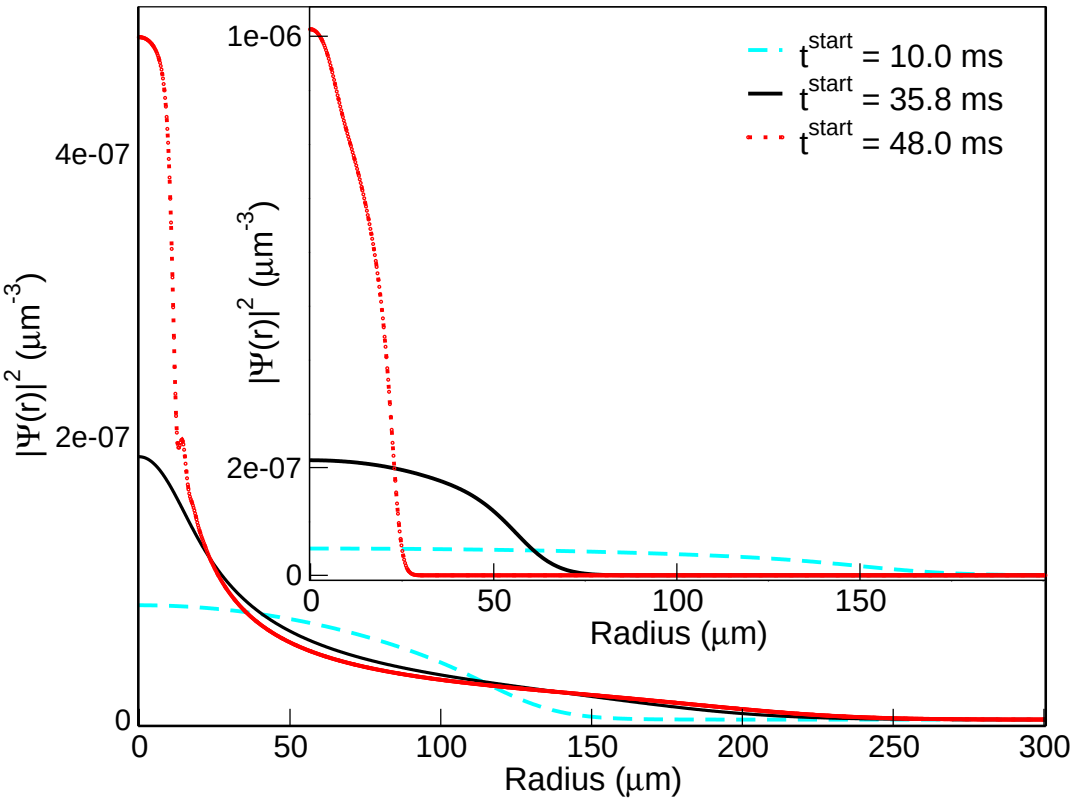

Figure 2.23: Time-evolution of the density profiles of a system of $N = 10^6$ condensed atoms of ^{87}Rb in a dipole trap (main figure) and in a harmonic trap (inset) of corresponding frequencies $\omega = 2\pi \times 31$ Hz. Three different configurations of DKC has been applied at t^{start} =10.0 ms during t_{dur}=1.25 ms, at t^{start}=35.8 ms during t_{dur}=0.805 ms and at t^{start}=48.0 ms during t_{dur}=0.302 ms. The geometry of the trap effect the time-evolution of the density, this is especially seen for the lens at t^{start}=48.0 ms.

with a linear spatial dependence. The magnetic moment of the atoms trapped precesses around the local field direction at the Larmor frequency

$$\omega_l = \frac{m_F g_F \mu_B |\vec{B}|}{\hbar} \tag{2.27}$$

The local magnetic field changes with the motion of the atoms, if this change is adiabatic with respect to ω_l, the atoms can stay in their low-field seeking state, but in experimental setups, a moving atom in a time-dependent field will induce transitions. The low-field seeking states make transitions to high-field seeking states, provoking them to be ejected from the trap, limiting the life-time of the atom in the trap, which is actually controlled by two mechanisms, leading to the trap loss. Firstly losses are produced by collisions with the background gas. Secondly, produced by the Majorana spin flips near the center of the trap. Such spin flips result from the fact that the direction of the field changes heavily and the spin orientations become nearly degenerate. Thus an atom passing through the zero-point in the magnetic field it no longer has a well defined quantization axis and its spin is flipped, and consequently it is ejected from the trap. This spin flip transition makes the trap having a 'hole' at zero magnetic field.[156].

This inconvenient is solved for instance by applying an oscillating bias magnetic field (TOP trap), or in general, by working with configurations without a zero field at the minimum.

2.2.3 Time-averaged orbiting potential (TOP)

The first experimental realization of a BEC was achieved in a TOP trap was made in 1995 [1]. TOP traps were designed to suppress Majorana losses occurring near the trap center by adding to the quadrupole field a rotating transverse spatially uniform field which effectuates a continuous motion of the location of the point where the field vanishes. This effect is easily seen from relation (2.29, sketched in fig. 2.24, when the magnetic field is given by eq. (2.28)

$$\vec{B}_{TOP} = B_0\,(\cos(\omega t), \sin(\omega t), 0) \tag{2.28}$$

the frequency ω is slow compared to the transition frequencies. Together with the quadrupole field, give the instantaneous field:

$$\vec{B} = \left(B_0\cos(\omega t) + B'_x x, B_0\sin(\omega t) + B'_y x, -2B'_z\right) \tag{2.29}$$

The magnitude of the total field is

$$|\vec{B}| = \left[\left(B_0\cos(\omega t) + B'_x x\right)^2 + \left(B_0\sin(\omega t) + B'_y y\right)^2 + 4B'^2_z z^2\right]^{1/2} \tag{2.30}$$

For $B'_x = B'_y = B'_z$ and averaging on time over a rotation period, $B_{TOP} = \frac{1}{T}\int_0^T B(t)dt$. Considering short distances from the vertex of the quadrupole field ($r \ll B'/B_0$) and substituting this field in eq. (2.30) one can find that the TOP potential results in a 3D axially symmetric, harmonic potential which never vanishes, filling the hole in the trap :

$$U_{TOP} \approx m_F g_F \mu_B \left[B_0 + \frac{B'}{4B_0}\left(x^2 + y^2 + 8z^2\right)\right] \tag{2.31}$$

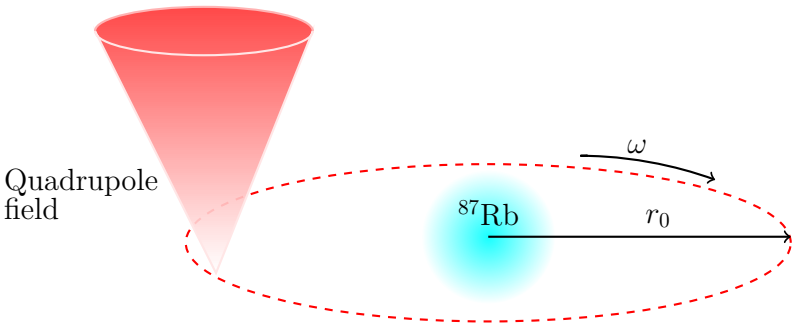

Figure 2.24: A slow-frequency rotating transverse bias field $\vec{B}_{TOP}$ added to the quadrupole trap ($\partial_r B_{quad}$), shifting the 'hole' from the center of the trap to $r_0 = \frac{|\vec{B}_{top}|}{\partial_r B_{quad}}$, the hole rotates in the so-called *circle of death*.

With the analogy to a typical harmonic potential, the frequencies are found to be

$$\omega_\rho = \left(\frac{M_F \mu_B B'^2}{8mB}\right)^{1/2}, \omega_z = \left(\frac{M_F \mu_B B'^2}{mB}\right)^{1/2} \tag{2.32}$$

leaving the typical relation between frequencies in the TOP trap: $\omega_z = \sqrt{8}\omega_\rho$.

In the presence of an anharmonicity generated by the gravity g (acting along $z-$axis) there is a linear dependence in the trap confinement, whose effect on the system depends on the shape of the potential. For a harmonic-type potential, the gravity will just displace the center of the trap, but as the approximation has been done for short distances, such a harmonic behavior extends only to $r = B_0/B'$. For a sufficiently strong gravitational force or a weak trap, the minimum will be displaced to a new equilibrium position by more than B_0/B' entailing a considerable modification of the trap geometry, since the magnetic force at the distance r is related to the gravitational force by:

$$\frac{\partial U}{\partial B} B' \leq mg \tag{2.33}$$

The transverse and linear frequencies will be respectively corrected as

$$\omega_\rho = \frac{1}{\sqrt{8}} \left(\frac{m_F \mu_B B'^2}{mB_0}\right)^{1/2} (1+\eta^2)^{1/2}(1-\eta^2)^{1/4} . \tag{2.34}$$

$$\omega_z = \left(\frac{m_F \mu_B B'^2}{mB_0}\right)^{1/2} (1-\eta^2)^{3/4} \tag{2.35}$$

with $\eta = \dfrac{mg}{m_F \mu_B B'}$. The equilibrium position is now $z_{grav} = -r\dfrac{\eta}{2(1-\eta^2)^{1/2}}$.

In the particular operation conditions of [6], a cloud of $N = 2 \times 10^5$ atoms of ^{87}Rb is trapped in a TOP potential created with the following physical parameters:

- $B'_z = 20.9$ G/cm
- $m_F = 1$
- $B_0 = 0.28$ G (initial)

resulting $\eta = 0.72965$, and the initial trap frequencies: $\omega_\rho = 2\pi\times$ 18.24 Hz and $\omega_z = 2\pi\times$ 28.495 Hz. It is expected the center of the trap to be displaced from the center of the trap.

Due to gravity, the ratio between the frequencies is now $\omega_z = \sqrt{2.44412}\omega_\rho$, instead of $\sqrt{8}$.

The cloud is not allowed to expand freely, rather the trap is shallowed by tunning the magnetic field into $B_0 = 6.9$ G, producing the new frequencies: $\omega_\rho = 2\pi\times$ 3.67 Hz, $\omega_z = 2\pi\times$5.74 Hz, being trapped during 162 ms and then released.

The experimental configuration considered in this case shows that the trap for long distances is far from being harmonic, since it has been found that it can be approximated

by a second kind elliptic integral E[1]

$$V(\rho,z) = gmz + 2\left(\sqrt{1-B}\cdot E[\frac{2B}{-1+B}] + \sqrt{1+B}\cdot E[\frac{2B}{1+B}]\right) \tag{2.36}$$

with $B = \dfrac{2B'B_0\rho}{B_0^2 + B'^2(4z^2+\rho^2)}$. This gives an extended form

$$\begin{aligned} V(\rho,z) = gmz + \frac{\mu_B}{\pi}\Bigg(&\sqrt{4B'^2z^2 + (B_0 - B'\rho)^2}\cdot E\left[\frac{-4B'B_0\rho}{4B'^2z^2 + (B_0 - B'\rho)^2}\right] \\ &+\sqrt{4B'^2z^2 + (B_0 + B'\rho)^2}\cdot E\left[\frac{4B'B_0\rho}{4B'^2z^2 + (B_0 + B'\rho)^2}\right]\Bigg) \end{aligned} \tag{2.37}$$

From the last expression is straightforward to see that the argument of the first integral is negative for any set of values, corresponding to the second term in eq. (2.40). The transformation to a positive argument elliptic integral is done by identifying:

$$k = \frac{2B}{-1+B}\ . \tag{2.38}$$

Therefore it is found

$$E(k) = E(\frac{2B}{-1+B}) = \sqrt{\frac{1+B}{1-B}}E(\frac{2B}{1+B}) \tag{2.39}$$

which can be noted is exactly the second integral in eq. (2.40). Now the potential simplifies to

$$V(r,z) = gmz + 4\left(\sqrt{1+B}\cdot E[\frac{2B}{1+B}]\right) \tag{2.40}$$

equivalently

$$V(\rho,z) = gmz + \frac{\mu_B}{\pi}2\sqrt{4B'^2z^2 + (B_0 - B'\rho)^2}\cdot E\left[\frac{-4B'B_0\rho}{4B'^2z^2 + (B_0 - B'\rho)^2}\right] \tag{2.41}$$

The relaxation of the trap is schematically represented by the trapping potentials sketched in fig. 2.25. The condensate is fabricated in the trap characterized by the potential shown in solid line in the radial (red line) and in the axial direction (black line) and created with the following physical parameters a magnetic field $B_0 = 0.28$ G and a magnetic gradient $B'_z = 20.9$ G/cm. After having the ground state, it is transferred to a shallower trap engineered by the

Producing a ground state centered at the minimum of the trap, described by the density profiles of the ground state wave function in the transverse and axial directions. The position of the peak density in the radial direction corresponds to the 0 of the coordinates position as it is shown in the black curve in fig. 2.26 and in z direction as an effect of the gravity the center is displaced to a new equilibrium position to the left negative values of position (red line) as it is expected from the trap geometry in solid lines in fig. 2.25.

1 Definition and properties of elliptic integrals can be found in [157]

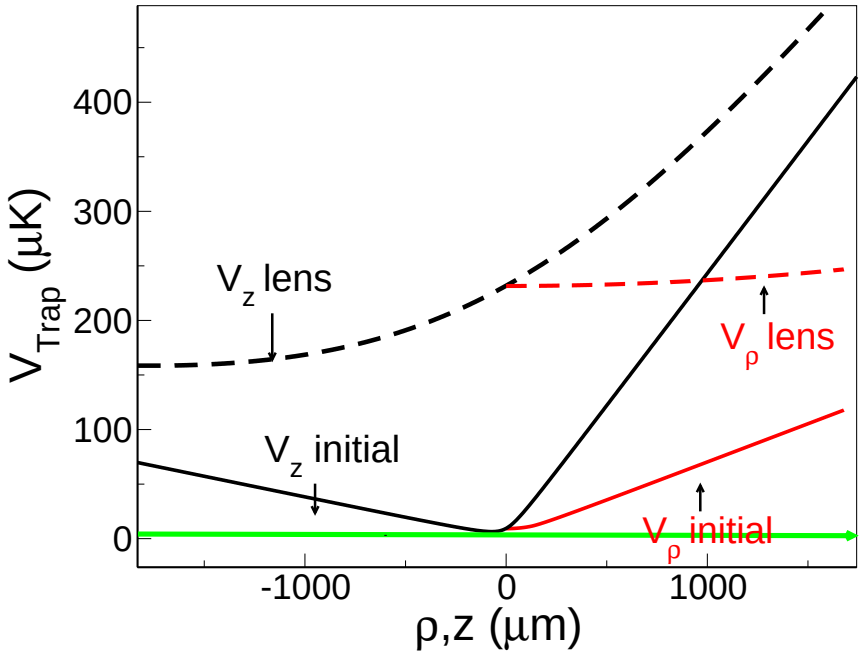

Figure 2.25: The system is initially trapped in the potential represented by the solid lines in axial z and transversal ρ directions. The dynamics of the condensate starts in the potential represented by dashed lines. The atoms stay trapped during 162 ms and then it will expand freely. The chemical potential indicated by the green line has the value 0.05746957 μK.

The condensate prepared in the TOP trap is allowed to expand in a shallower trap characterized by a magnetic field B_0 =6.9 G of eq. (2.41) and shown by dashed lines in fig. 2.25 during 162 ms as it is shown in fig. 2.25. After this time, it is entirely free to continue expanding for long times, of which we show here the first 200 ms of evolution. This protocol is proper for being applied in experiments.

A BEC in a shallower trap expands and its size oscillates in the radial direction as shown in fig. 2.27(a), if spatially-varying forces are not applied. After release, the expansion in the radial direction is linear, this is shown by the red triangles. In the axial direction, the size evolution is strongly influenced by the gravity acceleration as shown by the blue dots. The smaller values are for the condensate reaching the edge of the trap, which are the limits of the grid used for the computations. The two directions have been treated independently. This coincides with the minima in the time evolution of the position of the condensate sketched in fig. 2.27(b). While being trapped, the BEC moves along a large region of a size of the order of 5 mm. This figure also shows that after releasing completely the BEC, the position in z-direction increases and decreases as a consequence of the grid size considered, since it is expected the atoms to fall under the influence of gravity.

There is another experimental realization that is considered in this work to simplify the formation of the BEC in miniaturized systems, this is by using a microscopic magnetic trap on an atom chip.

2.2.4 Microscopic magnetic traps on a chip

The chip-based atom trap superpose quadrupole and a static field which leads to a non-vanishing magnetic minimum. The power of these devices lies in the flexibility of the magnetic fields that can be created.

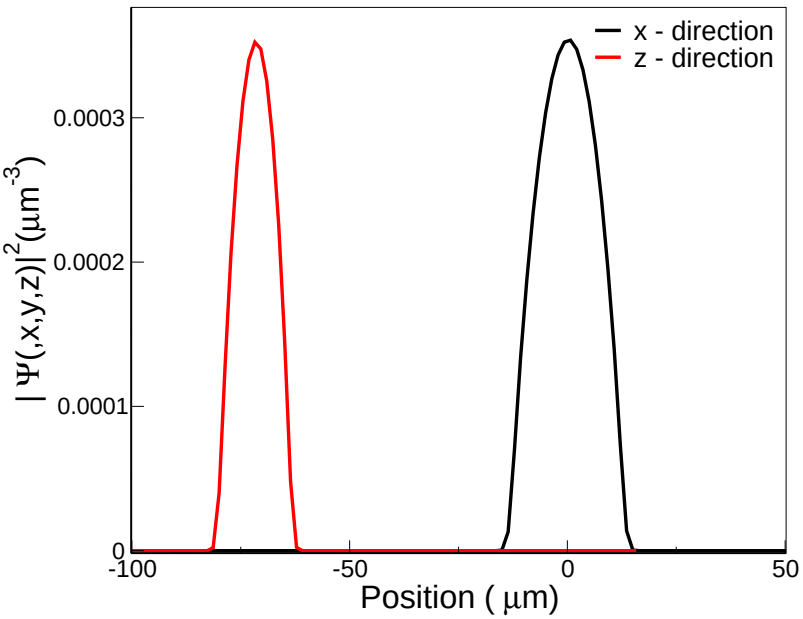

Figure 2.26: Density profile of the ground state wave function of a condensate consisting of $N = 2 \times 10^5$ atoms of ^{87}Rb trapped in the TOP trap created with a magnetic field $B_0 = 0.28$ G and a magnetic gradient $B'_z = 20.9$ G/cm, characterized in fig. 2.25. The black curve shows the density along the radial direction and the red curve show it in the longitudinal direction where gravity is acting. The two profiles are symmetric with respect to the position of the minimum of the trap in the respective direction. Gravity acceleration for these calculations has been considered as being $g = 9.81m \cdot s^2$.

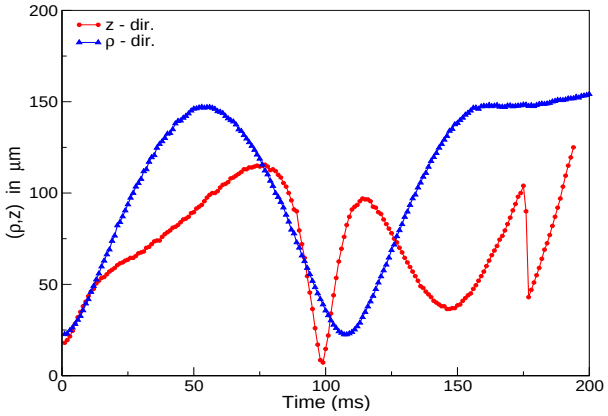

(a) Time evolution of the radius in the transverse (blue triangles) and longitudinal (red dots) directions.

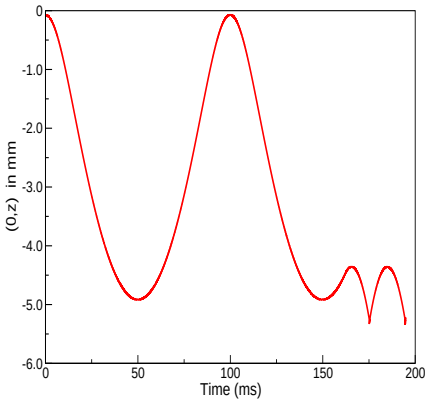

(b) Variation of position of the peak density in the longitudinal direction where gravity is acting.

Figure 2.27: Time-evolution of the size (radius defined by eq. (2.9)) of a condensate consisting of $N = 2 \times 10^5$ atoms of ^{87}Rb prepared in the TOP trap created with a magnetic field $B_0 = 0.28$ G and a magnetic gradient $B'_z = 20.9$ G/cm, expands during the first t =162 ms in a shallow trap created by the new magnetic field $B_0 = 6.90$ G, after this time, the condensate is freely expanding, completing a total evolution time of t=200 ms. In (a) is shown the radius of the atomic cloud in each direction. The change of position of the peak density in the longitudinal direction as a consequence of the gravity acting on the BEC is shown in (b).

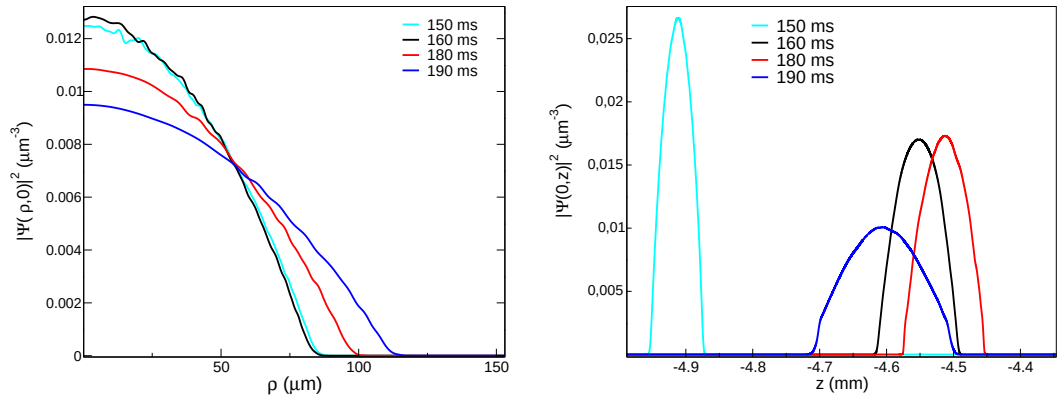

(a) Time evolution of the density profile in the radial direction.

(b) Time evolution of the density profile in the longitudinal direction.

Figure 2.28: The time evolving of a BEC of ^{87}Rb in a TOP trap is depicted. A DKC protocol by shallow the trap is applied during the first 162 ms of expansion. The density profiles before and after removing the trap are shown. The motion of the cloud due to gravity is appreciated. In $r-$direction the density is slightly distorted because the cloud is large and explores a large region of the trap.

The atom chip setup provides a fast creation of condensates due to the large trap frequencies achieved. The application of condensates on atom chips is what matters here is the quantum test of the weak equivalence principle by the QUANTUS collaboration [114], and more particularly the MAIUS project [158], which is going to be operated with the trap configuration shown in fig. 2.29 corresponding to a data set taken from MAIUS for the three spatial directions. The simulation data and the interpolated potential used to numerically study the dynamics of a system of 10^5 condensed atoms of ^{87}Rb are plotted below in fig. 2.29, which in detail is: For the $x-$direction which is the most symmetric, the simulation data points are depicted as brown dots and the fitted polynomial as yellow solid lines, in both cases, with and without the presence of the gravity acceleration, left and right side figures respectively. The $y-$direction, where the gravity acceleration is applied is shown with dark green triangles (data from the simulation) and gray solid line (fitted polynomial) which as can be seen, it is the most asymmetric direction, and its ground state and the dynamics are going to be studied in more detail in a 1D approximation; finally, the $z-$direction is displayed, the simulated values in magenta triangles and its respective polynomial fitting in cyan solid line.

Effective 1D calculation of the ground state and dynamics of $N = 10^5$ condensed atoms of ^{87}Rb in the gravity-direction

A condensed cloud of $N = 10^5$ atoms of ^{87}Rb is trapped in an effective 1D potential corresponding to the y-direction which has a highly non-trivial symmetry. It is expected to deviate most from a conventionally used harmonic potential.

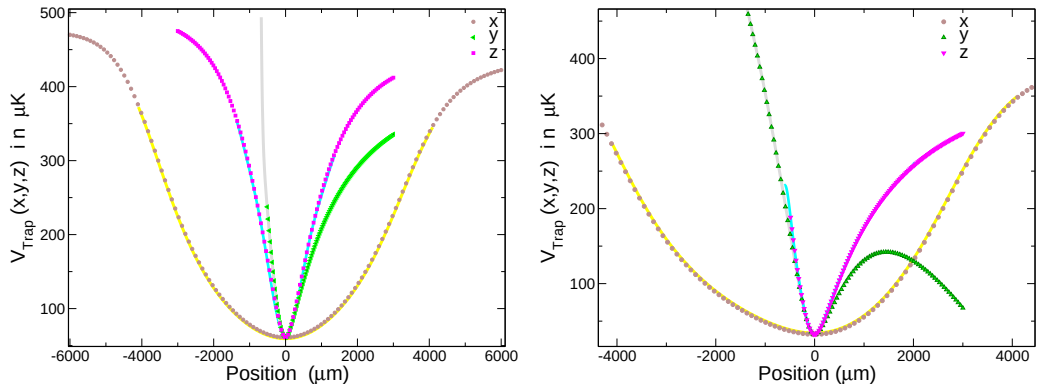

Figure 2.29: Trap potential on a chip. Figures on the left show the pure frequencies configuration to create the potential in each spatial direction. The curves on the right are under the influence of gravity which is applied in y-direction. The experimental values (from MAIUS project, not published yet) are depicted by dots: brown, green and magenta for the $x-$, $y-$ and $z-$ directions respectively, and their corresponding polynomial fitting used for the numerical simulations are shown in yellow, gray and cyan solid lines.

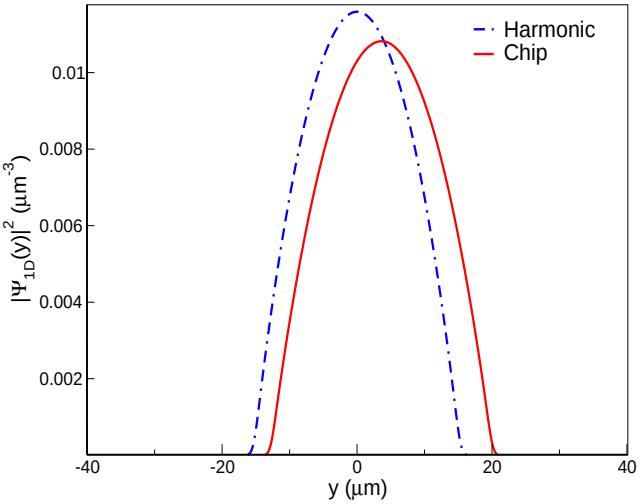

Figure 2.30: For comparison, the ground state density profiles of a cloud of $N = 10^5$ condensed atoms of ^{87}Rb prepared in a chip-based potential trap depicted in red solid line. Dashed blue line shows the ground state density profile of the same system prepared in a harmonic trap. The density of the atomic cloud in the chip potential is not fully symmetric and shows an offset of $\sim 3\mu m$ with respect to the harmonic case. Functions are solutions of the GPE.

We are interested in comparing the ground state and the time-evolution of the atomic cloud prepared in a harmonic trap and in a chip-based potential between each other, not in TF solutions since the deviations with respect to harmonic solutions have been already shown in former cases of this chapter. The ground state density profile of the atomic cloud in such a potential is contrasted with a calculation of the same system performed for a harmonic potential. In the former case, the potential is steeper on the left side effecting the condensate wave function to be only slightly displaced to the right side, see the potential in fig. 2.29, shown here by the red solid curve in fig. 2.30, which differs from the harmonic case shown by the blue dashed line in fig. 2.31 and fig. 2.32. This effect should be important for the dynamics besides the conditions of re-trapping the atomic cloud in a DKC procedure.

Now, the condensate is allowed to freely expand for a time t^{start} =25 ms when a DKC is applied during t_{dur}=0.23 ms to continue propagating during a total time of 1 s. The time-evolution in the two cases is very different from each other as can be seen from the radius as a function of time, the final radius of the cloud in a chip-based potential is larger by $\sim$ 186 μm than that of the harmonic potential, this is clearly seen in the blue

dashed line in figs. fig. 2.31 and fig. 2.32.

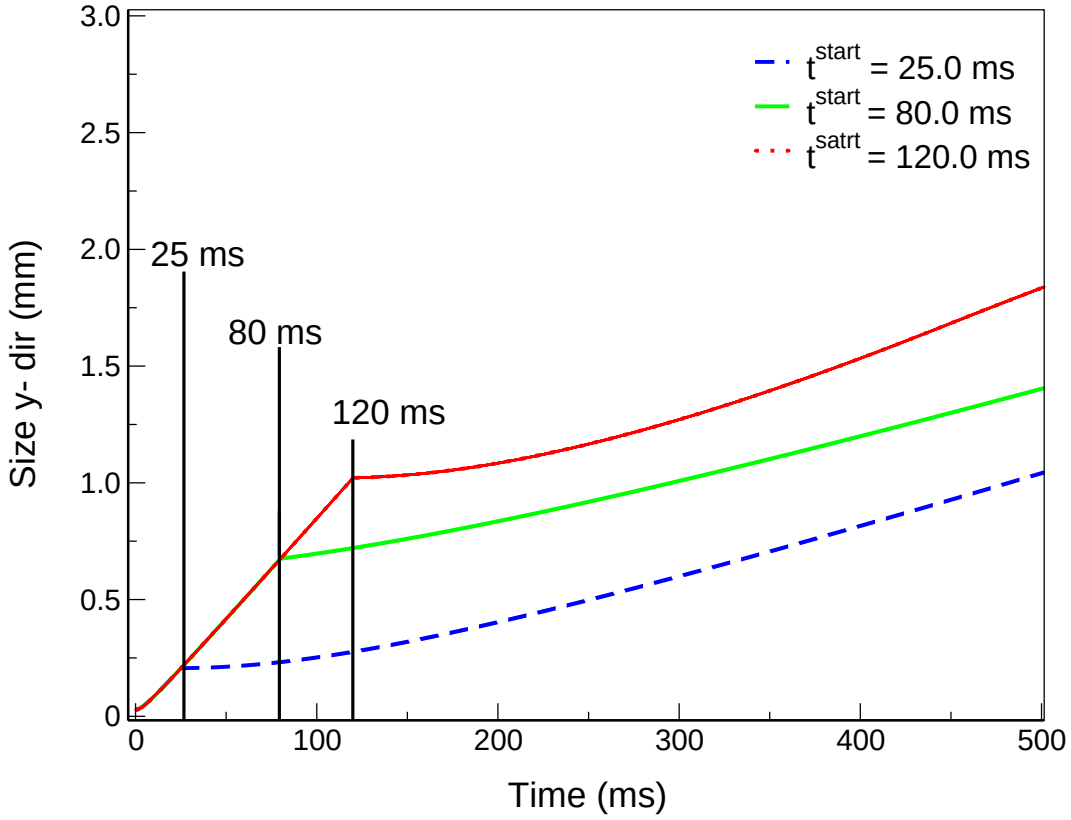

Figure 2.31: Time-evolution of the y-width = $[\int\ y^2\ |\Psi(y)|^2\ dy]^{1/2}$) with a DKC applied. Expansion of a condensed cloud of $N = 10^5$ atoms of ^{87}Rb trapped in a chip-based potential. A total expansion time of 500 ms has been considered. Three cases of DKC are shown in the main figure: t^{start}=25.0 ms, t^{start}=80.0 ms and t^{start}=120.0 ms..

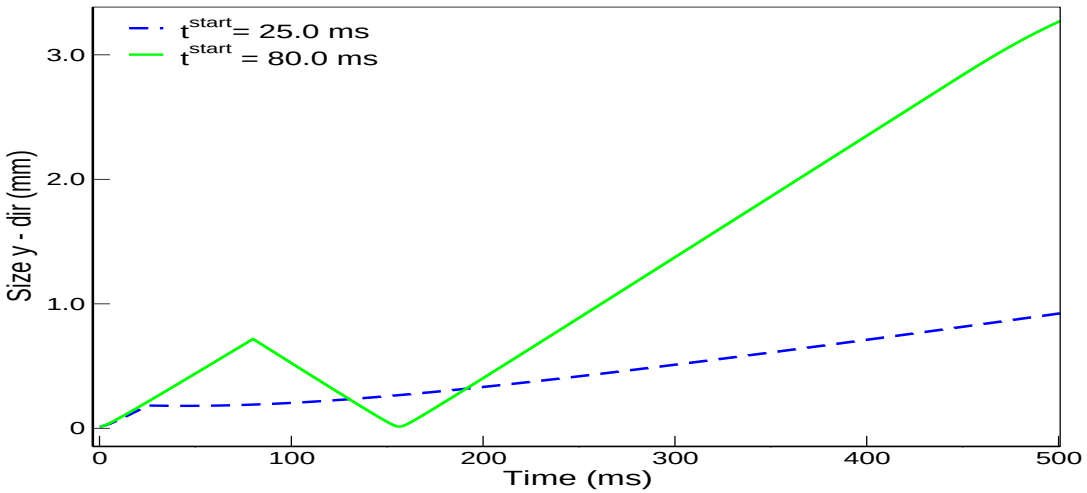

Figure 2.32: Time-evolution of the radius (the less symmetric direction $1/2\sqrt{\sigma_y^2}$)with a DKC applied. Expansion of a condensed cloud of $N = 10^5$ atoms of ^{87}Rb trapped in a harmonic potential. A total expansion time of 500 ms has been considered. Two cases of DKC protocols are shown, at t^{start}=25.0 ms (dashed blue line) and at t^{start}=80.0 ms (green solid line).

By applying a DKC protocol, the results obtained from considering a chip-based potential are further away from what is obtained by using the common harmonic potential, even if the condensate is allowed to freely expand for a short time before applying the DKC, this is when the system does not yet occupy a large region of the trap, such a case is depicted in fig. 2.31 and fig. 2.32 by the dashed blue line.

An interesting situation for experiments is to apply the DKC at later times, the condensate will be more influenced by the shape of the potential, there have been considered two cases with different starting times of the DKC and with the same effect, these are shown by the green solid line with t^{start}=80.0 ms and t_{dur}=0.1 ms, and the red solid line with t^{start}=120.0 ms and t_{dur}=0.09 ms, in figs. fig. 2.31 and fig. 2.32. The time-evolution of the radius of the condensate subjected to a harmonic potential is shown in the inset for the two former cases, the latter is not needed due to the evident discrepancy observed in the second case. The evolution of the cloud by considering these two traps dramatically differ from each other. The time-evolution of the radius also shows that the starting time and duration to apply the DKC is not producing an equally efficient collimation for both cases, showing that the harmonic potential is no longer a good guide to study the dynamics of the BEC.

An efficient DKC includes an optimal duration to produce a highly collimated cloud lowering the speed of the atoms by some orders of magnitude, this can be obtained equally by the three equivalent DKC protocols of the figure above, however it is important to take into account the shape of the density profile. When DKC is applied at t^{start}=25.0 ms the condensate expands undistorted, which is not the case for t^{start}=80.0 ms which shows a cloud strongly affected by the tightening of the cloud and the asymmetry of the trap with the appearance of side wiggles. This is another indication of the inconvenience of using a harmonic case as an approximation for non-symmetric potentials at large sizes.

The non-trivial symmetric expansion is manifested in the motion of the peak-density observed in fig. 2.33 and fig. 2.34 does not necessarily mean a displacement of the wave function, it is mainly due to the distortion effected by the trap geometry and the need of the system to reach equilibrium. The two first cases discussed above are shown. The oscillations observed in the first case is due to the fact that the condensate at the moment of applying DKC is not yet linearly expanding, but some interaction energy remains in the system, this is detailed in fig. 2.34 where the corresponding density profiles at the times indicated by numbers in fig. 2.33 are displayed.

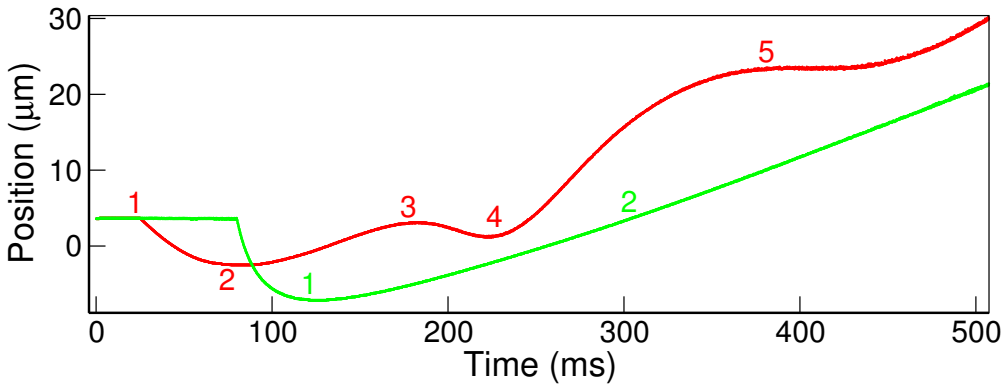

Figure 2.33: Position of the peak density when two different DKC protocol are applied. The red line shows the shift of the maximum value of the density profile before and after a DKC started at t^{start} = 25.0 ms during t_{dur}=0.23 ms. A more stable position of the maximum is observed in the green curve by waiting a longer time to apply the DKC at t^{start}=80.0 ms during t_{dur}=0.1 ms. The numbers characterize interesting moments whose wave functions are shown below.

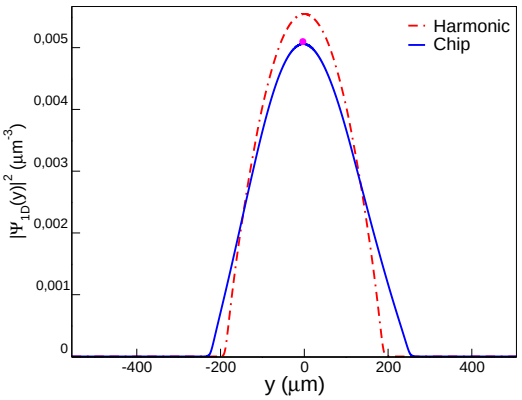

(a) Density profiles at t =80 ms. (2) t^{start}=25.0 ms.

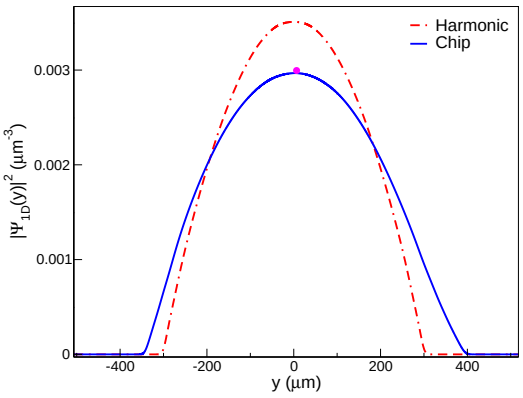

(b) Density profiles at t =180 ms. (3) t^{start}=25.0 ms.

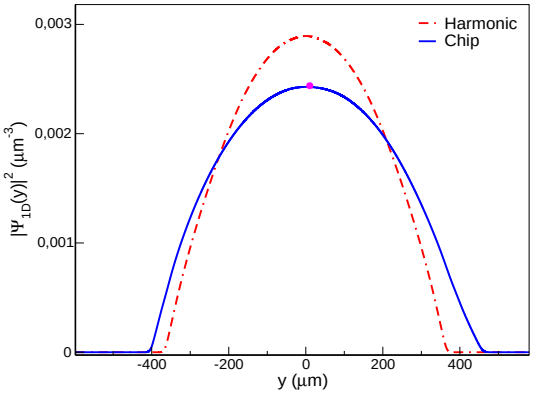

(c) Density profiles at t =220 ms. (4) t^{start}=25.0 ms.

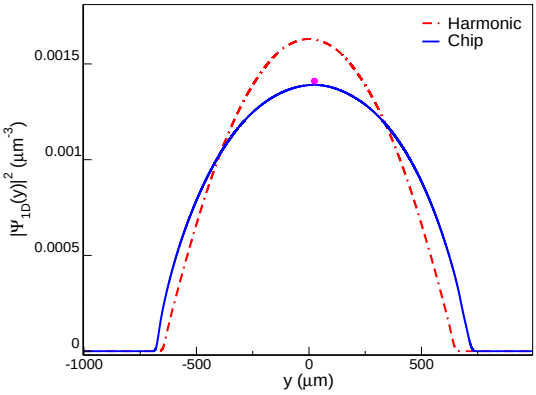

(d) Density profiles at t =370 ms. (5) t^{start}=25.0 ms.

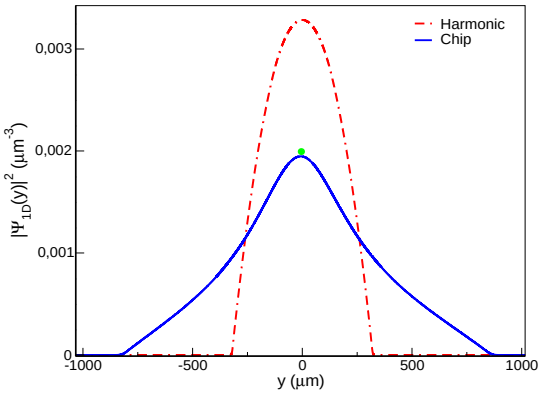

(e) Density profiles at t =120 ms. (1) t^{start}=80.0 ms.

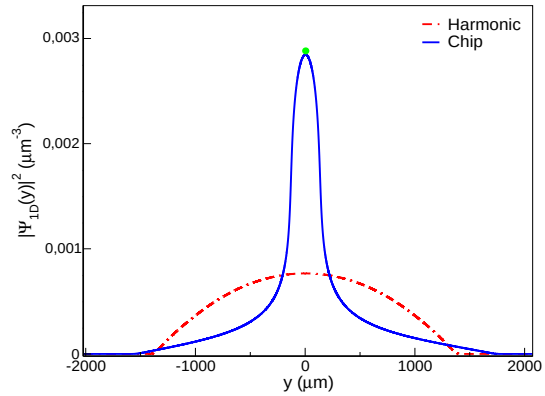

(f) Density profiles at t =300 ms. (2) t^{start}=80.0 ms.

Figure 2.34: Time-evolution of the density profile of a condensed cloud of $N = 10^5$ atoms of ^{87}Rb trapped in a chip-based potential (solid blue line) contrasted with the system trapped in a harmonic potential (dashed red lines) showing the change in position of the peak-density due to the symmetry of the trapping potential. For the harmonic case, the position of the maximum is constant. A DKC protocol is applied starting at $t^{start} = 25.0\ ms$ with a DKC duration of t_{dur}=0.23 ms in the upper and middle rows; the lower row is for starting the DKC at $t^{start} = 80.0\ ms$ during t_{dur}=0.1 ms. The numbers in the sub-captions indicate the positions marked in fig. 2.33

2.3 Conclusion

For the study of the ground state density profiles and evolution of single-component BECs, several cases including different physical situations have been considered, these are, variations of type and strength of interactions, trapping conditions; and different DKC protocols.

Compact, slowly expanding and stable BECs of ^{87}Rb, ^{41}K, ^{85}Rb and ^{39}K, from which the last two have attractive inter-atomic interactions have been considered. It has been taken advantage of the Feshbach resonances to tune the interactions into a repulsive ones and it has been derived a simple energy equilibrium condition to guarantee long expansion times without concerns about collapse. The compactness and slow expansion of the gases have been achieved with the application of delta-kick cooling.

Additionally, ground state and time dependent wave functions of BECs prepared in trapping potentials which are closer to those experimentally implemented, such as, optical dipole, chip-based and TOP traps differ dramatically from those obtained with the commonly used harmonic traps.

In both cases, for the BEC in an optical dipole and in a magnetic chip-based traps in absence of gravity, has been found that the clouds are less sensitive to a strong DKC, sufficient to collimate them than using a harmonic potential.

A large ensemble of ^{87}Rb prepared in a TOP potential. The slow expansion in this case is reached by relaxing the potential during the first 162 milliseconds, finding an interesting motion of the atoms' center of mass position.

The ground state density profiles and the dynamics of different species of BECs have been calculated by solving the time-dependent Gross-Pitaevskii equation with the tSSO computational method. The results obtained for the dynamics have been contrasted with the ones obtained by solving a set of coupled differential equations resulting from the Scaling approach.

Long-time expansion is requested for the implementation of the samples as sources for atom interferometer in a microgravity environment as well as ground-based experiments.

CHAPTER 3

DKC of mixtures of BECs and Long-time behavior

In this chapter, ground states and dynamics of dual mixtures of Bose-Einstein condensates of different atomic species [26, 34, 37, 42, 112, 159] are studied for long expansion times. Such systems allow to create a wide variety of physical scenarios, where the interplay between the intra/inter-species interactions gives rise to different phases [34, 37, 112]. In the following, the Gross-Pitaevskii equation for mixtures is solved and a generalization to binary BECs of the scaling approach is presented.

In the following, the Gross-Pitaevskii equation for mixtures is solved and a generalization to binary BECs of the scaling approach is presented.

Relevant results of several pairs are discussed, for instance: ^{87}Rb/^{85}Rb and ^{87}Rb/^{41}K, from which, suitable regimes of expansion can be used to test the weak equivalence principle or in general, as sources for interferometry-based experiments.

3.1 Miscibility criterion in uniform traps

This section is devoted to derive the criterion for stable miscible (immiscible) binary mixtures of BECs as it is presented in Ketterle's review [113].

The binary mixture components are are considered to be trapped in square-well potentials of rigid walls with volumes $Vol_{1,2}$, and the space occupied by the mixture is bound by the potential which has a volume $Vol = Vol_1 + Vol_2$. For simplicity, the kinetic energy is neglected in the total energy. Next two distinct situations are considered:

- The two components overlap and fill the total volume Vol. In our calculations mixtures studied are balanced, this is, consisting of the number of particles $N_1 = N_2 = N$. In this case the interaction energy is given by

$$E_O = \frac{N^2}{2Vol}\left[g_{11} + g_{22} + 2g_{12}\right] \tag{3.1}$$

- The two separate components occupy volumes Vol_1 and $Vol_2 = Vol - Vol_1$, the interaction energy is now

$$E_s = \frac{N^2 g_{11}}{2Vol_1} + \frac{N^2 g_{22}}{2Vol_2} \tag{3.2}$$

The volumes Vol_1 and Vol_2 can be found from the condition of equal pressures $\partial E_s(\vec{r})/\partial Vol_1 = \partial E_s(\vec{r})/\partial Vol_2$, this is the mechanical equilibrium, which gives the relationship

$$\frac{g_{11}N}{Vol_1^2} = \frac{g_{22}N}{Vol_2^2}, \rightarrow \frac{Vol_1}{Vol_2} = \sqrt{Ng_{11}/Ng_{22}} \tag{3.3}$$

Considering the threshold of miscibility, this is when $E_s = E_0$, then equating the equations

$$\frac{N^2 g_{11}}{2Vol_1} + \frac{N^2 g_{22}}{2Vol_2} = \frac{N^2}{2Vol}\left[g_{11} + g_{22} + 2g_{12}\right] \tag{3.4}$$

by simplifying $\frac{N^2}{2}$, and using $Vol = Vol_1 + Vol_2$, eq. (3.4) is re-written

$$\begin{aligned} \frac{1}{Vol_1 + Vol_2}\left[g_{11} + g_{22} + 2g_{12}\right] &= \frac{g_{11}}{Vol_1} + \frac{g_{22}}{Vol_2} \qquad (3.5)\\ = \frac{1}{Vol_1 + Vol_2}\left[g_{11} + g_{22} + 2g_{12}\right] &= \frac{g_{11}}{Vol_1}\left(1 + \frac{Vol_2}{Vol_1}\right)\\ = \frac{Vol_1}{Vol_1 + Vol_2}\left[g_{11} + g_{22} + 2g_{12}\right] &= g_{11}\left(1 + \frac{Vol_2}{Vol_1}\right) \end{aligned}$$

To free the interaction terms in the left side of eq. (3.5)

$$g_{11} + g_{22} + 2g_{12} = \frac{Vol_1 + Vol_2}{Vol_1} g_{11}\left[1 + \frac{Vol_2}{Vol_1}\right] \tag{3.6}$$

using eq. (3.3)

$$\begin{aligned} g_{11} + g_{22} + 2g_{12} &= \frac{Vol_1 + Vol_2}{Vol_1} g_{11}\left(1 + \sqrt{\frac{g_{22}}{g_{11}}}\right) \qquad (3.7)\\ = g_{11} + g_{22} + 2g_{12} &= \left[1 + \frac{Vol_2}{Vol_1}\right] g_{11}\left(1 + \sqrt{\frac{g_{22}}{g_{11}}}\right)\\ = g_{11} + g_{22} + 2g_{12} &= \left[1 + \sqrt{\frac{g_{22}}{g_{11}}}\right] g_{11}\left(1 + \sqrt{\frac{g_{22}}{g_{11}}}\right) \qquad (3.8) \end{aligned}$$

therefore

$$\begin{aligned} g_{11} + g_{22} + 2g_{12} &= \left[1 + \sqrt{\frac{g_{22}}{g_{11}}}\right]^2 g_{11} \qquad (3.9)\\ g_{22} + 2g_{12} &= \left[\frac{g_{22}}{g_{11}} + 2\sqrt{\frac{g_{22}}{g_{11}}}\right] g_{11} \end{aligned}$$

distributing g_{11} into the bracket, we obtain

$$\begin{aligned} g_{22} + 2g_{12} &= 2\sqrt{g_{22} g_{11}} + g_{22} \qquad (3.10)\\ g_{22} + 2g_{12} &= \left[\frac{g_{22}}{g_{11}} + 2\sqrt{\frac{g_{22}}{g_{11}}}\right] g_{11} \end{aligned}$$

By simplifying g_{22} in both sides of eq. (3.10) one arrives to the well-known miscibility criterion:

$$g_{12} = \sqrt{g_{22} g_{11}}, \tag{3.11}$$

for the miscibility or phase separation in a homogeneous two-component mixture. The most common parametrization of the miscibility criterion in terms of the scattering

lengths and is expressed by the parameter Δ:

$$\Delta = \frac{a_{22}a_{11}}{a_{12}^2} - 1. \tag{3.12}$$

The condensates will spatially separate if $\Delta \leq 0$ or mix when $\Delta > 0$. Phase separation due to interactions was first observed in 1956 in superfluid mixtures of ^{3}He–^{4}He [159]. One can engineer miscible or immiscible mixtures by tuning the interactions as it was experimentally demonstrated in Cornell's group in 2008 [26].

This criterion of eq. (3.12) has been derived under particular conditions of trap homogeneity. The criterion is, however not accounting for perturbations of the system as for example gravitational sag, magnetic or gravity gradients, or different trapping geometries.

3.1.1 Mean field approach

Mean field theory provides a good description of BEC mixtures.

Let's consider an ensemble of two interacting degenerate gases labeled 1 and 2, of N_1 and N_2 particles each, trapped by an external potential $V_{1(2)}$ and characterized by the wave functions $\Psi_1(\vec{r},t)$ and $\Psi_2(\vec{r},t)$, respectively. The effective inter (g_{12})- and intra ($g_{11(22)}$)- species interactions at low temperature (contact interactions) and the interaction effect by other particles in a mean-field approximation lead to the well-known coupled time-dependent Gross Pitaevskii equation (c-TDGPE) that governs the dynamics of the wave functions $\Psi_{1(2)}(\vec{r},t)$. The c-TDGPE reads [53]

$$\begin{aligned} i\hbar\partial_t\Psi_1(\vec{r},t) &= \left[\frac{-\hbar^2}{2m_1}\nabla^2 + V_1(\vec{r},t) + N_1 g_{11}|\Psi_1(\vec{r},t)|^2 + N_2 g_{12}|\Psi_2(\vec{r},t)|^2\right]\Psi_1(\vec{r},t) \\ i\hbar\partial_t\Psi_2(\vec{r},t) &= \left[\frac{-\hbar^2}{2m_2}\nabla^2 + V_2(\vec{r},t) + N_2 g_{22}|\Psi_2(\vec{r},t)|^2 + N_1 g_{21}|\Psi_1(\vec{r},t)|^2\right]\Psi_2(\vec{r},t) \end{aligned} \tag{3.13}$$

where for $i,j = 1,2$, g_{ij} is the effective inter- and intra-species interaction strength (inter- for $i \neq j$ and intra- for $i = j$).

In analogy with the description made for single-component gases in the very dilute regime, the interaction strengths here read as

$$g_{ii} = \frac{4\pi\hbar^2 a_i}{m_i}, \qquad g_{ij} = \frac{2\pi\hbar^2 a_{ij}}{m_{red}}, \quad i = 1,2,\ j = 1,2, \tag{3.14}$$

therein m_i is the mass of the atoms of species-i and a_i is the respective scattering length. In addition, $m_{red} = m_i m_j/(m_i + m_j)$ is the reduced mass of the mixture, and a_{ij} quantifies the inter-component interaction.

For large ensembles, i.e. for N_1 and $N_2 \gg 1$, the spatial scale of density perturbations is large too, such that the kinetic energy can be neglected. Thus, the stationary solution of the eq. (3.13) reads

$$V_i(\vec{r},t) + N_i g_{ii}|\Psi_i(\vec{r},t)|^2 + N_j g_{ij}|\Psi_j(\vec{r},t)|^2 = \mu_i,\ i,j = 1,2\ , \tag{3.15}$$

where μ_i is the chemical potential for the mixture components which is calculated in appendix A, and therefore, the densities of the two condensates read

$$|\Psi_i(\vec{r},t)| = \left[\frac{g_{jj}\left(\mu_i - V_i\left(\vec{r},t\right)\right) - g_{ij}\left(\mu_j - V_j\left(\vec{r},t\right)\right)}{N_i(g_{ii}g_{jj} - g_{ij}^2)}\right]^{1/2}. \tag{3.16}$$

Note that the wave functions of the two components preserve the normalization condition, i.e. $\int |\Psi_i(\vec{r})|^2 d\vec{r} = 1$. The normalization is evaluated in the whole region of extensions R_1 and R_2 of the atomic clouds, which are defined

$$R_i = \left[\frac{2\mu_i}{m_i\omega_i^2}\right]^{1/2}, \quad i = 1,2 \tag{3.17}$$

Using a box potential to increase miscibility

Ultracold gases in box potentials offer the possibility of approaching more the many-body systems that are spatially box, allowing to study for instance, phase transitions. Our motivation to study this topic is related to BEC mixtures and miscibility.

Condensates in box potentials have been already experimentally created with ^{87}Rb atoms in the $|F = 2, m_F = -2\rangle$ magnetic sublevel. [160]

In general, the density profiles scale linearly with the trapping potential of the system, taking up the same geometry, as can be seen in most of the results discussed along this document, this has been effectively experimentally observed in the condensate reached in Hadzibabic's group [160].

Taking into account the robustness of the box potentials, it is expected to produce densities with higher bulk contributions than the ones obtained by using for example harmonic traps, which makes a condensate more robust against the appearance of a possible segregation due to interactions.

The most natural way to proceed is to study the mixture in the three interesting regimes, these are: the two extreme values ("highly miscible" at $a_{85} = 900a_0$, and phase separation at $a_{85} = 100a_0$), and the threshold of validity of miscibility criterion for a mixture ^{87}Rb/^{85}Rb, which it has been already indicated, it happens at $a_{85} = 458a_0$.

Ground states of the ^{87}Rb/^{85}Rb mixture in a box with hard walls potential The miscibility criterion eq. (3.12) predicts the separation or coexistence of two BECs prepared in a box potential, therefore it is expected to be rigorously fulfilled in mixtures prepared in such potentials.

The ground state density profiles of the three more representative cases for a mixture of $N = 10^4$ atoms each component are shown in fig. for the miscible/immiscible and intermediate regimes.

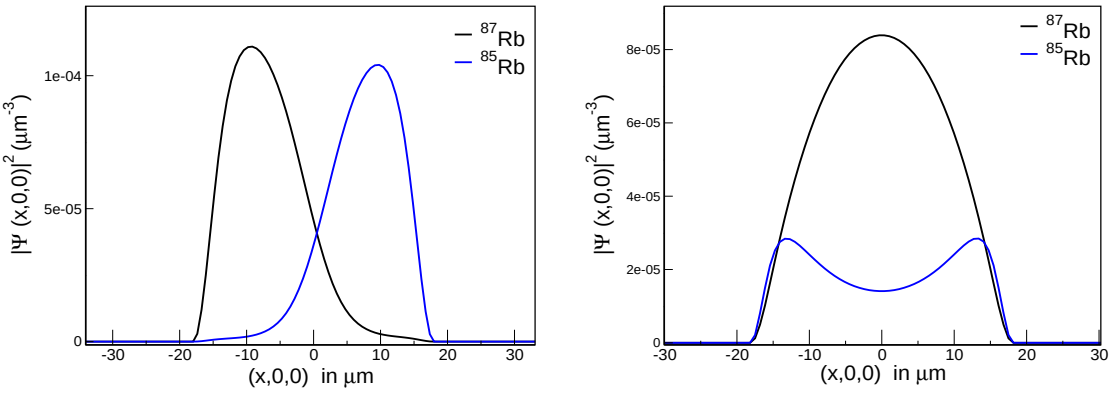

(a) Immiscible regime.

(b) Threshold of miscibility.

Figure 3.2: A ^{87}Rb/^{85}Rb mixture of $N = 10^4$ atoms each component in a box potential, characterized by a trap depth of the order of 100 nK. In (a) the mixture is tuned to the immiscible regime, this is a spontaneous symmetry breaking occurs, with $a_{85} = 100a_0$. The system is nearly in the threshold of miscibility, at $a_{85} = 460a_0$, the criterion is fulfilled in (b). Two completely interpenetrating BECs are observed in (c) when $a_{85} = 900a_0$, the trap depth in this case is of the order of 200 nK. In the horizontal axis is the x- direction, this is position (x,0,0) no radius.

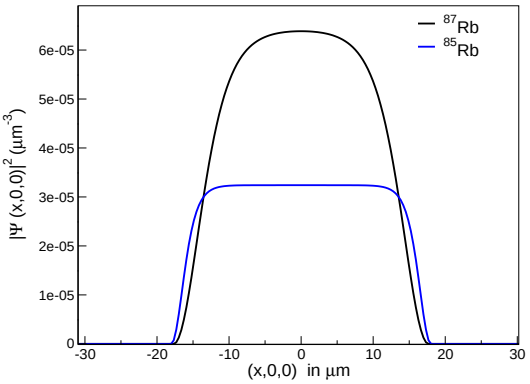

(c) Miscible regime.

In a mixture of components having nearly the same masses ^{87}Rb/^{85}Rb, the parameter Δ given by eq. (3.12) for the three situations considered in fig. 3.20, have the values: $\Delta = 0.9639$ for $a_{85} = 900a_0$ (highly miscible), $\Delta = -0.7818$ for $a_{85} = 100a_0$ (highly immiscible) and $\Delta = 0.00377$ for $a_{85} = 460a_0$ (threshold of miscibility [19]). The results in fig. 3.20, show that the criterion eq. (3.12) is rigorously fulfilled.

3.2 Ground states of tunable mixtures

In this section, several BECs mixtures covering a wide range of situations are discussed. Such systems are: ^{87}Rb/^{85}Rb, with ^{85}Rb having attractive self-interactions at zero magnetic field; ^{87}Rb/^{41}K, inter- and intra-species interactions are repulsive; ^{87}Rb/^{39}K, intra-species interactions of ^{39}K are attractive; and ^{87}Rb/^{170}Yb, the inter-species interactions are attractive. In all cases, the trapping potentials are considered to be isotropic and harmonic.

Such a symmetry allows to reduce the dimensions of the equations to solve, since three-dimensional systems freely expanding by long times reach very large sizes require large grids to be computed. Such calculations need extremely long-computational time. The reduction of the GPE to spherical coordinates is detailed in [**Adhikari2012**].

The results presented correspond to the solutions of the spherical c-TDGPE contrasted with those of c-SA.

3.2.1 The ^{87}Rb/^{85}Rb mixture

The first two-component mixture with condensates was produced for ^{87}Rb isotope in the $|2, -2\rangle$ and $|1, -1\rangle$ - hyperfine states[20]. While ^{87}Rb/^{85}Rb has a long history dating back to 1998 when it was considered by Burke *et al.*[161] to study interpenetrating bosonic superfluids. The first experimental realization of such a system was carried out by two groups [26, 28].

The parameters used in this mixture are related in Table 3.1.

Four cases are discussed, ensembles of balanced ^{87}Rb/^{85}Rb mixtures in the miscible (immiscible) regime consisting of $N = 10^3$ ($N = 10^6$) atoms each species. The condensate is prepared in a trap, with the frequencies of Table 3.1. The change in the number of atoms and the scattering length allows for observing complex phases.

The density profiles are plotted in fig. 3.3. The mixture is in the predicted very immiscible regime, this is, $a_{85} = 100a_0$ and $N = 10^3$ and $N = 10^6$. The miscibility parameter has been tuned to $\Delta = -0.7818$.

Table 3.1: Parameters of ^{87}Rb/^{85}Rb. The mixture is expected to exhibit miscibility when $a_2 > 458a_0$ and $B = 160.3$G. ^{87}Rb atoms are in $|F = 1, m_F = -1\rangle$ magnetic sublevel and ^{85}Rb in $|F = 2, m_F = -2\rangle$.

Isotope	N atoms	$\omega_{x,y,z}$ ($\times 2\pi$ Hz)	a (a_0 [a])	a_{12} (a_0)
^{87}Rb	10^6	39.537	99	213
^{85}Rb	10^6	40.0	variable	213

[a] Bohr radius

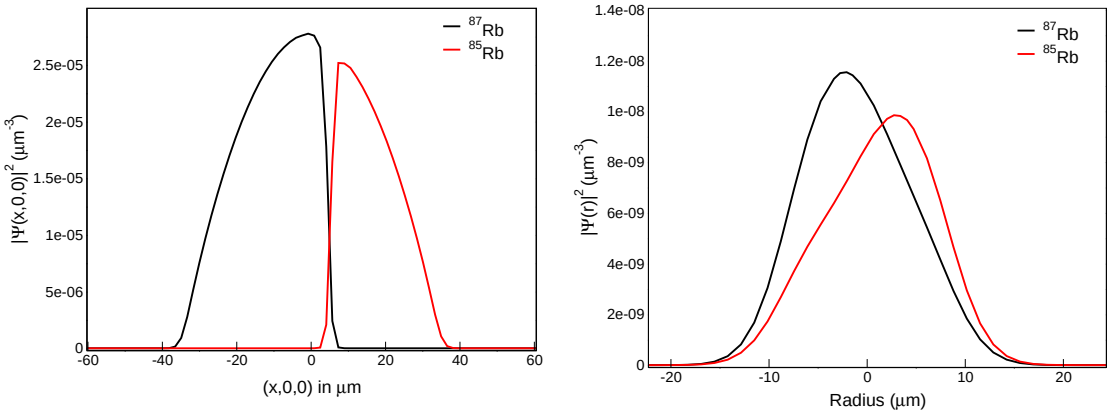

(a) a_{85}= 100 a_0. $N = 10^6$ **(b)** a_{85}= 100 a_0. $N = 10^3$

Figure 3.3: Density profiles of ^{87}Rb/^{85}Rb in an expected immiscible phase. In (a) the mixture consists of $N = 10^6$ atoms each component. The clouds are well separated, and the spherical symmetry is broken.

fig. 3.4, shows that the mixture for $\Delta = 0.9639$ corresponding to $a_{85} = 900a_0$ with the same number of atoms as above. The magnetic field required to tune the interactions in ^{85}Rb is not affecting the inter-species interactions nor the intra-species interactions of ^{87}Rb.

In this miscible regime, the clouds exhibiting a non-trivial shape, a shell structure in which one gas forms a shell around the other. The two clouds are only partially overlapped, in the strongly interacting regime ($N = 10^6$).

The overlap between the gases pair is linked to different factors, for instance, the number of atoms and the trap potentials. Figure 3.5 illustrates this dependence.

fig. 3.5 shows that the overlap between ^{87}Rb/^{85}Rb is close to 100% only for very small number of particles ($\sim 10^3$). This result is valid also for what is expected to be in the deeply miscible regime a_{85}= 900 a_0. This is explained by the effect of realistic traps which are harmonic in contrast with the uniform ones.

In the miscible regime and high particles numbers ($> 10^3$), the overlap due to the shell structure is reduced and has to be accounted for in precision experiments which require the samples to be highly overlapped.

3.2.2 The ^{87}Rb/^{41}K mixture

In the last examples, non-trivial behavior of the Rb isotopes mixture was observed due to the large inter-species interactions.

In contrast to the previous case, the inter-species interactions between ^{87}Rb and ^{41}K

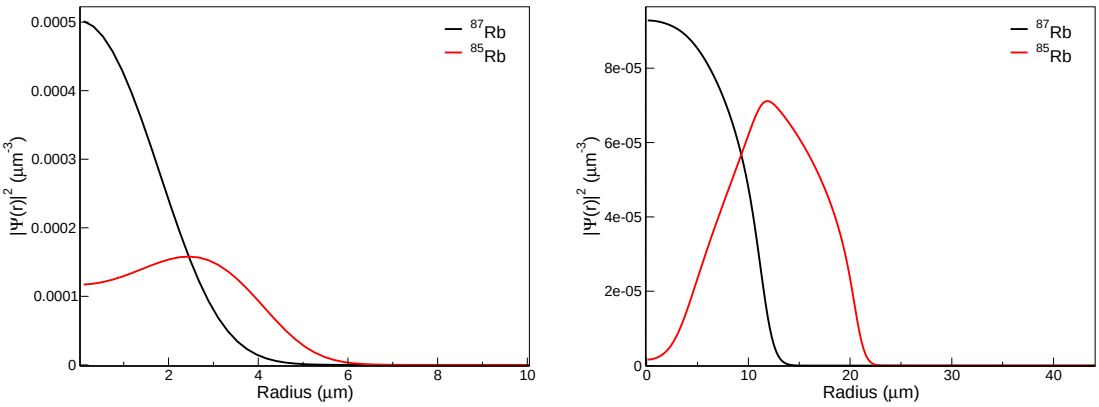

(a) a_{85}= 900 a_0. $N = 10^3$ **(b)** a_{85}= 900 a_0. $N = 10^6$

Figure 3.4: Density profiles of mixtures of ^{87}Rb/^{85}Rb the parameters are the same as in the two cases in fig. 3.3 except the scattering length has been tuned to 900 a_0. The mixture in (a) is in the weakly interacting regime, showing a high miscibility. In (b) a strongly interacting regime $N = 10^6$ atoms, the overlap is still low in spite of being predicted by theory as being in a miscible regime.

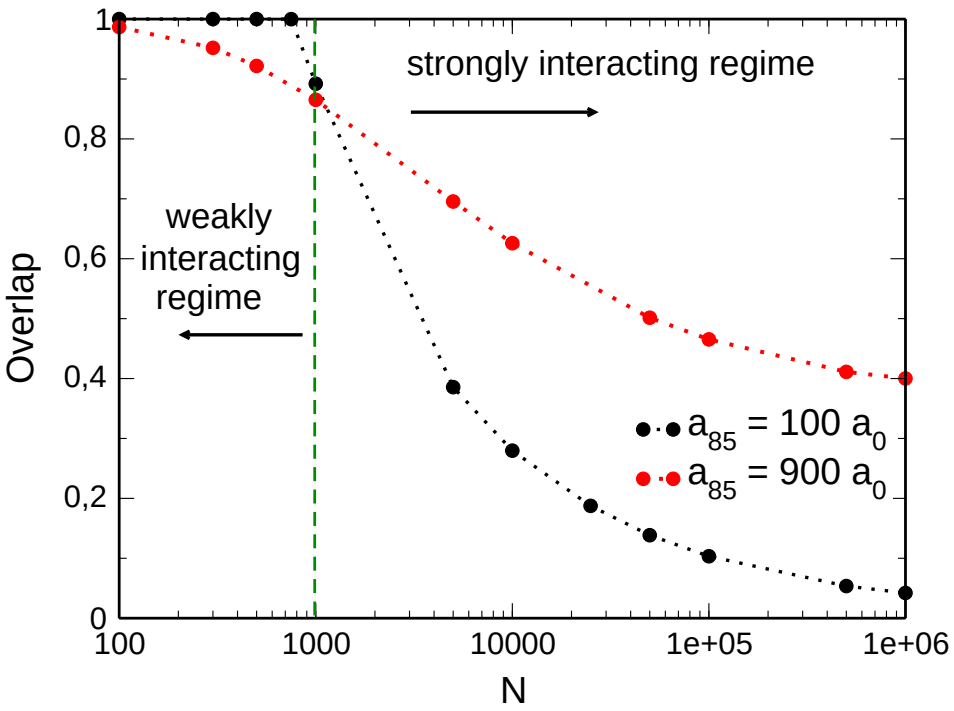

Figure 3.5: Overlap of the ground states of the ^{87}Rb/^{85}Rb mixture. Here, the parameter $\beta_{12} = m_1 N_1 g_{12}/\sqrt{1/m_1\omega_1}$ has a wide usefulness since with it, the influence of several parameters in the emergence of the different phases can be studied. A balanced mixture, was prepared in a dipole trap, keeping the frequencies unchanged. Each data point was obtained by changing the number of particles equally for both species.

can be tuned with a relatively moderate Feshbach field of about 80 G [162, 163]. The physical parameters used for this mixture are related in Table 3.2

Table 3.2: Parameters for the mixture ^{87}Rb/^{41}K. Inter-species interactions can be tuned to 0 using a bias magnetic field B=80.2 G, the original value of the inter-species scattering length for collisions is $a_{41-87} = 163a_0$ [163]. The trapping frequencies are the same in all three directions.

Isotope	N atoms	$\omega_{x,y,z}$ ($\times 2\pi$ Hz)	a (a_0)	a_{12} (a_0)
^{87}Rb	10^6	8.0	99	0
^{41}K	10^6	11.653	60.54[a]	0

a Value obtained by [164]

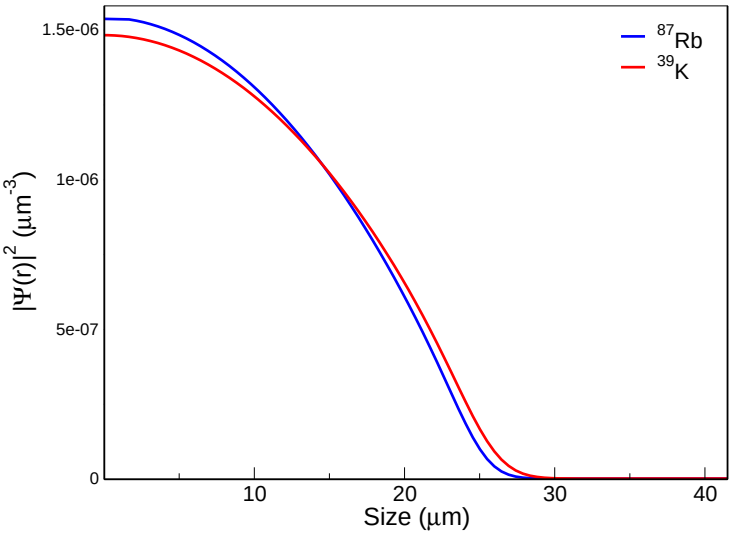

Figure 3.6: Density profiles of the GS wave functions, these are the spherical solutions of a balanced non-interacting mixture of $N = 10^6$ atoms of ^{87}Rb/^{41}K. By tuning the inter-species interactions to 0, the clouds coexist, there is a perfect overlapping. At zero magnetic field, the two condensates strongly repel each other.

In this case, the components expand with a high overlap during the entire propagation time as can it can be seen from the density profiles shown for the density after 9 s of expansion in fig. 3.6. In this case, the magnetic field has been kept during the first 200 ms of expansion.

3.2.3 The ^{87}Rb/^{39}K mixture

The case of the ^{87}Rb/^{39}K mixture is considered, in which, ^{39}K has by nature attractive interactions, being $a_{39} = -29a_0$.

The parameters used to produce this mixture are related in Table 3.3.

Table 3.3: Parameters of the ^{87}Rb/^{39}K mixture. Intra-species interactions indicated by a in the fourth columnof the table for ^{39}K have been tuned from $a_{39} = -29a_0$ [166] to $100a_0$ with a bias magnetic field B=414 G. a_{12} in the last column is the inter-species scattering length has not been modified

Isotope	N atoms	$\omega_{x,y,z}$ ($\times 2\pi$ Hz)	a (a_0)	a_{12} (a_0)
^{87}Rb	10^6	8.0	99	34
^{39}K	10^6	11.95	100.0	34[a]

a Value taken from [164]

Unlike the ^{87}Rb/^{41}K mixture, a high magnetic field is required to bring the ^{87}Rb/^{39}K

mixture into a convenient stable and miscible regime. For these physical parameters the ground state of the mixture components are calculated in fig. 3.7.

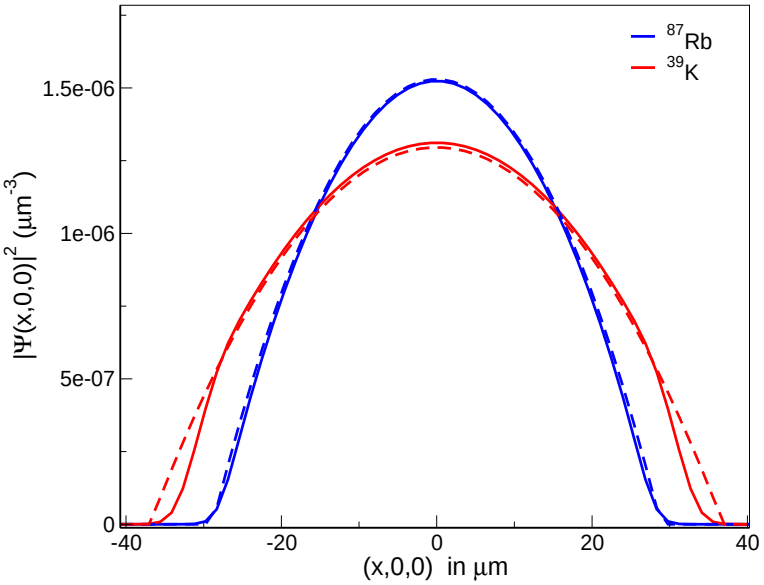

Figure 3.7: Density profiles of a mixture containing 10^6 atoms of ^{87}Rb/^{39}K. With the intra-species interactions of ^{39}K set to $a_{39} = 100a_0$. The ground state solutions show two perfectly coexisting gases The magnetic field B=414 G needed is quite strong compared to the one used in previous cases. TFA for both components are plotted with dashed lines. A full 3D GPE has been solved to obtain the ground state solutions.

Although the ground state solutions of the mixture seem to be quite stable for the set of parameters chosen, the magnetic field to produce such a stabilization is high and has been taken off at t =200 ms.

3.2.4 The ^{87}Rb/^{170}Yb mixture

Stable Yb isotopes have properties which make them very convenient for precision measurements, unlike alkali, the Yb isotopes have no magnetic moment in their ground state, resolving the need for magnetic shielding.

^{170}Yb is not the most abundant isotope ($\sim 3.056\%$), but is chosen since no need for an external stabilization against collapse is required.

Table 3.4: Parameters used for the preparation in a harmonic trap of ^{87}Rb/^{170}Yb mixture. Collision properties of ^{170}Yb can be found in [167] and inter-species scattering length value is taken from [168].

Isotope	N atoms	$\omega_{x,y,z}$ ($\times 2\pi$ Hz)	a (a_0)	a_{12} (a_0)
^{87}Rb	10^6	87.72	99	-11.45
^{170}Yb	10^6	62.839	63.89	-11.45

The attractive inter-species interactions is counter-acted by the strong intra-species repulsions, giving rise to the stable and overlapped GS of the mixture.

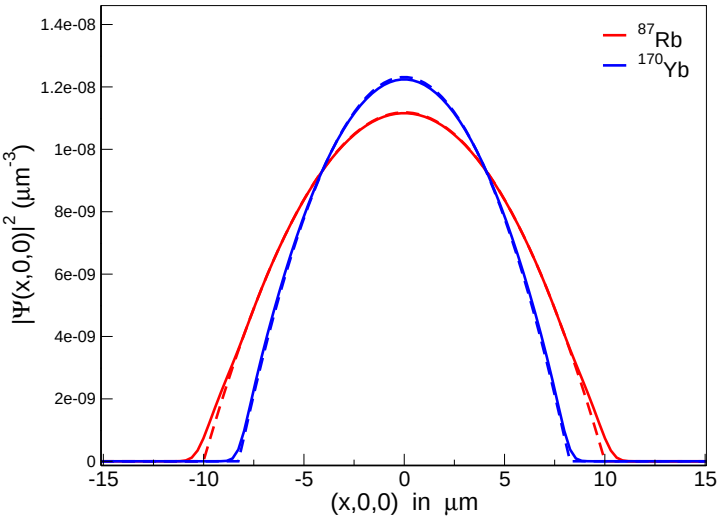

Figure 3.8: Density profiles of a mixture of $N = 10^6$ atoms each component of ^{87}Rb/^{170}Yb confined in a harmonic trap with the frequencies indicated in Table 3.4. The spatial density of this ensemble is characterized by the large overlap. The results shown are from the numerical solution of the 3D TD-GPE (solid lines) contrasted with the Thomas Fermi solutions (dashed lines). $a_{87/170} = -11.45a_0$.

In this case, the ground state of the mixture is found to be symmetric, stable and completely miscible, illustrating the miscibility of the pair without further tuning of external magnetic Feshbach field.

3.3 Dynamics of tunable mixtures

3.3.1 Theoretical model

The dynamics of multi-component BECs mixtures is studied by calculating the time evolution of sizes and the density profiles of the BECs by solving the c-TDGPE eq. (3.13) and extending the scaling approach of sect. 2.0.2 to mixtures in the miscible regime which is where we are interested. Phase separation may be considered in a future study.

Scaling approach for miscible mixtures

In addition to the treatment of mixtures by the c-TDGPE which can be lengthy in calculating many trials of the dynamics for fulfilling the specific requirements of experiments, a scaling approach computation is performed for having quick preliminary results that are afterwards compared to the more accurate c-TDGPE calculations.

In order to account for the mutual interactions between constituent gases, a generalization of the scaling theory proposed in [128, 129] and discussed for single-component gases in sect. 2.1.5 is done for mixtures.

It has been seen in sect. 2.1.6 and sect. 2.1.7 that the expansion of large ensembles of alkali atoms can be well approximated by classical dynamical equations describing the motion of particles subjected to a conservative force or just by free propagation after being released from the trap. The procedure for determining the motional equations is as follows.

We start with the coupled time-independent Gross Pitaevskii equations (c-TIGPE) for mixtures in a very dilute regime:

$$\begin{aligned}\left[-\frac{\hbar^2}{2m_1}\nabla^2 + U_1 + N_1 g_{11}|\Psi_1|^2 + N_2 g_{12}|\Psi_2|^2\right]\Psi_1 &= \mu_1\Psi_1\\ \left[-\frac{\hbar^2}{2m_2}\nabla^2 + U_2 + N_2 g_{22}|\Psi_2|^2 + N_1 g_{12}|\Psi_1|^2\right]\Psi_2 &= \mu_2\Psi_2\end{aligned} \tag{3.18}$$

where m_1 is the species-1 mass, m_2 is the species-2 mass, V_1 the harmonic trapping

potential of species-1, V_2 the trapping potential of species-2. $g_{ii\prime}$ are the effective s-wave interactions between particles of a same gas, $g_{ij\prime}$ $\{i,j = 1,2\}$, are the inter-species interactions, defined in eq. (3.1.1).

In a gas at $T = 0$ and with a very large number of particles N the kinetic energy can be considered as negligible, therefore it is applied the Thomas Fermi approximation:

$$\begin{aligned} \mu_1 &= U_1 + g_{11}n_1 + g_{12}n_2 \\ \mu_2 &= U_2 + g_{22}n_2 + g_{12}n_1 \end{aligned} \tag{3.19}$$

Inverting these two equations, we obtain the spatial densities for both gases

$$n_1 = \frac{g_{22}\left(\mu_1 - U_1\right) - g_{12}\left(\mu_2 - U_2\right)}{\left(g_{11}g_{22} - g_{12}^2\right)}$$

$$n_2 = \frac{g_{11}\left(\mu_2 - U_2\right) - g_{12}\left(\mu_1 - U_1\right)}{\left(g_{11}g_{22} - g_{12}^2\right)} \tag{3.20}$$

For reasons of stability of the system, it is required that $g_{11}g_{22} > g_{12}^2$, see eq. (3.12). And knowing that $n_1, n_2 > 0$.

Introducing the model of a classical gas in which each particle experiences a force, which for condensates 1 and 2 are respectively:

$$\begin{aligned} \vec{F}_1(\vec{r},t) &= -\nabla\left(U_1(\vec{r},t) + N_1 g_{11}\rho_{cl,1}(\vec{r},t) + N_2 g_{12}\rho_{cl,2}(\vec{r},t)\right) \\ \vec{F}_2(\vec{r},t) &= -\nabla\left(U_2(\vec{r},t) + N_2 g_{22}\rho_{cl,2}(\vec{r},t) + N_1 g_{12}\rho_{cl,1}(\vec{r},t)\right) \end{aligned} \tag{3.21}$$

where $\rho_{cl,i}, i = 1,2$ are the spatial densities in the gas normalized to N. At $t = 0$ the equilibrium condition ($\vec{F}_i = 0$) gives $\rho_{cl,i}(\vec{r},0) = N_i|\Psi_{TF,i}(\vec{r},0)|^2$ which are given by eq. (3.20). Upon release from the trap, the gases begin to expand, and its size can be described by $\vec{R} = (Rx,Ry,Rz)$

$$R_{j,i}(t) = \lambda_{j,i}(t)R_j(0), \begin{cases} j = x,y,z \text{ (direction index)} \\ i,i' = 1,2 \text{ (sample index)} \end{cases} \tag{3.22}$$

and, the spatial evolution of the classical density is

$$\begin{aligned} \rho_{cl,i}(\vec{r},t) &= \frac{\rho_{cl,i}}{\lambda_{x,i}(t)\lambda_{y,i}(t)\lambda_{z,i}(t)}\left[\left\{r_{j,i}/\lambda_{j,i}\left(t\right)\right\}_{j=x,y,z},0\right] \\ &= \frac{1}{\lambda_{x,i}(t)\lambda_{y,i}(t)\lambda_{z,i}(t)}\left[\frac{g_{i'i'}}{\bar{g}}\left(\mu_i - U_i(r_j/\lambda_j,0)\right)\right. \\ &- \left.\frac{g_{ii'}}{N_{i'}\bar{g}}\left(\mu_{i'} - U_{i'}(r_j/\lambda_j,0)\right)\right] \end{aligned} \tag{3.23}$$

where for shortening, $\bar{g} = g_{11}g_{22} - g_{12}^2$.

Applying Newton's law to the trajectories eq. (3.22)

$$m_i\ddot{\lambda}_{j,i}(t)R_{j,i}(0) \;=\; -\partial_{r_{j,i}}U_i\left[\vec{R}_i(t),t\right]+\frac{\partial_{r_{j,i}}U_i\left[\vec{R}_i(0),0\right]}{\lambda_{j,i}\lambda_{x,i}\lambda_{y,i}\lambda_{z,i}} \tag{3.24}$$

For condensate - 1 it is found

$$\begin{aligned}
&\sum_{j=x,y,z} m_1\ddot{\lambda}_{j,1}r_{j,1}\\
=\;& -m_1\left(\omega_{x,1}^2 r_{x,1}\lambda_{x,1}+\omega_{y,1}^2 r_{y,1}\lambda_{y,1}+\omega_{z,1}^2 r_{z,1}\lambda_{z,1}\right)\\
+\;& \frac{1}{\lambda_{x,1}\lambda_{y,1}\lambda_{z,1}}\left[g_{22}m_1(\omega_{x,1}^2\frac{r_{x,1}}{\lambda_{x,1}}+\omega_{y,1}^2\frac{r_{y,1}}{\lambda_{y,1}}+\omega_{z,1}^2\frac{r_{z,1}}{\lambda_{z,1}})\right.\\
-\;& \left. g_{12}m_2(\omega_{x,2}^2\frac{r_{x,2}}{\lambda_{x,2}}+\omega_{y,2}^2\frac{r_{y,2}}{\lambda_{y,2}}+\omega_{z,2}^2\frac{r_{z,2}}{\lambda_{z,2}})\right]\frac{N_1 g_{11}}{\bar{g}}\\
+\;& \frac{1}{\lambda_{x,2}\lambda_{y,2}\lambda_{z,2}}\left[g_{11}m_2(\omega_{x,2}^2\frac{r_{x,2}}{\lambda_{x,2}}+\omega_{y,2}^2\frac{r_{y,2}}{\lambda_{y,2}}+\omega_{z,2}^2\frac{r_{z,2}}{\lambda_{z,2}})\right.\\
-\;& \left. g_{12}m_1(\omega_{x,1}^2\frac{r_{x,1}}{\lambda_{x,1}}+\omega_{y,1}^2\frac{r_{y,1}}{\lambda_{y,1}}+\omega_{z,1}^2\frac{r_{z,1}}{\lambda_{z,1}})\right]\frac{N_2 g_{12}}{\bar{g}}.
\end{aligned} \tag{3.25}$$

and similarly for condensate - 2.

$$\begin{aligned}
&\sum_{j=x,y,z} m_2\ddot{\lambda}_{j,2}r_{j,2}\\
=\;& -m_2\left(\omega_{x,2}^2 r_{x,2}\lambda_{x,2}+\omega_{y,2}^2 r_{y,2}\lambda_{y,2}+\omega_{z,2}^2 r_{z,2}\lambda_{z,2}\right)\\
+\;& \frac{1}{\lambda_{x,2}\lambda_{y,2}\lambda_{z,2}}\left[g_{11}m_2(\omega_{x,2}^2\frac{r_{x,2}}{\lambda_{x,2}}+\omega_{y,2}^2\frac{r_{y,2}}{\lambda_{y,2}}+\omega_{z,2}^2\frac{r_{z,2}}{\lambda_{z,2}})\right.\\
-\;& \left. g_{12}m_2(\omega_{x,2}^2\frac{r_{x,1}}{\lambda_{x,1}}+\omega_{y,1}^2\frac{r_{y,1}}{\lambda_{y,1}}+\omega_{z,1}^2\frac{r_{z,1}}{\lambda_{z,1}})\right]\frac{N_2 g_{22}}{\bar{g}}\\
+\;& \frac{1}{\lambda_{x,1}\lambda_{y,1}\lambda_{z,1}}\left[g_{22}m_1(\omega_{x,1}^2\frac{r_{x,1}}{\lambda_{x,1}}+\omega_{y,1}^2\frac{r_{y,1}}{\lambda_{y,1}}+\omega_{z,1}^2\frac{r_{z,1}}{\lambda_{z,1}})\right.\\
-\;& \left. g_{12}m_2(\omega_{x,2}^2\frac{r_{x,2}}{\lambda_{x,2}}+\omega_{y,2}^2\frac{r_{y,2}}{\lambda_{y,2}}+\omega_{z,2}^2\frac{r_{z,2}}{\lambda_{z,2}})\right]\frac{N_1 g_{12}}{\bar{g}}.
\end{aligned} \tag{3.26}$$

Which for the scaling parameters $\lambda_{j,1}$ can be written

$$\begin{aligned}
&\sum_{j=x,y,z} m_1 \ddot{\lambda}_{j,1} \\
= \; & -m_1 \left(\omega_{x,1}^2 \lambda_{x,1} + \omega_{y,1}^2 \lambda_{y,1} + \omega_{z,1}^2 \lambda_{z,1}\right) \\
+ \; & \frac{1}{\lambda_{x,1}\lambda_{y,1}\lambda_{z,1}} \left[g_{22} m_1 \left(\frac{\omega_{x,1}^2}{\lambda_{x,1}} + \frac{\omega_{y,1}^2}{\lambda_{y,1}} + \frac{\omega_{z,1}^2}{\lambda_{z,1}}\right) \right. \\
- \; & \left. g_{12} m_2 \left(\frac{x_1}{x_2}\frac{\omega_{x,2}^2}{\lambda_{x,2}} + \frac{y_1}{y_2}\frac{\omega_{y,2}^2}{\lambda_{y,2}} + \frac{z_1}{z_2}\frac{\omega_{z,2}^2}{\lambda_{z,2}}\right) \right] \frac{N_1 g_{11}}{\bar{g}} \\
+ \; & \frac{1}{\lambda_{x,2}\lambda_{y,2}\lambda_{z,2}} \left[g_{11} m_2 \left(\frac{\omega_{x,2}^2}{\lambda_{x,2}}\frac{x_1}{x_2} + \frac{y_1}{y_2}\frac{\omega_{y,2}^2}{\lambda_{y,2}} + \frac{z_1}{z_2}\frac{\omega_{z,2}^2}{\lambda_{z,2}}\right) \right. \\
- \; & \left. g_{12} m_1 \left(\frac{\omega_{x,1}^2}{\lambda_{x,1}} + \frac{\omega_{y,1}^2}{\lambda_{y,1}} + \frac{\omega_{z,1}^2}{\lambda_{z,1}}\right) \right] \frac{N_2 g_{12}}{\bar{g}}.
\end{aligned} \tag{3.27}$$

and a similar expression was found for condensate - 2.

This approach is not valid when the system starts with a vanishing or negative scattering length since it has been neglected the kinetic energy of the bosons, which for the case of attractive interaction it is not possible to balance an attraction between bosons. To describe a system initially attractive interactions further calculations are needed.

The c-SA is numerically solved with the Runge–Kutta method which is presented in Appendix C.

Here we will focus on ^{87}Rb/^{85}Rb, ^{87}Rb/^{41}K, ^{87}Rb/^{39}K and, ^{87}Rb/^{170}Yb bosonic mixtures.

3.3.2 Long-time behavior. Results

Binary mixtures of BECs are released the trapping potential to allow for long free expansion times which are required in many experimental realizations. The long-time behavior is strongly influenced by the inter-particle interactions. The different bosonic mixtures considered in this study cover a wide range of possibilities, these are attractive intra- and inter-species interactions in some cases tuned to a strongly or weakly repulsive regime as will be detailed in each case.

Free expansion at long times

A two-component mixture of BECs which expands freely for a long-time reaches large sizes and their density profile shapes change due to the free or induced variation of the interactions. In all cases considered, the mixtures consist of $N = 10^6$ atoms in each component and are allowed to freely evolve during 1 s. The evolution of the system is studied by the two computation methods, the c-SA and the solution of c-TDGPE.

The ^{87}Rb/^{85}Rb mixture After a free evolution, the mixture reaches a radius of $\sim$4 mm The expansion rates of ^{87}Rb and ^{85}Rb are close to $\sim$2.2 mm/s and 4 mm/s respectively. Results between the two computing methods are compared, which for free expansion are in a good agreement. The small overlap of the wave functions is preserved during the free evolution as shown in fig. 3.9(b).

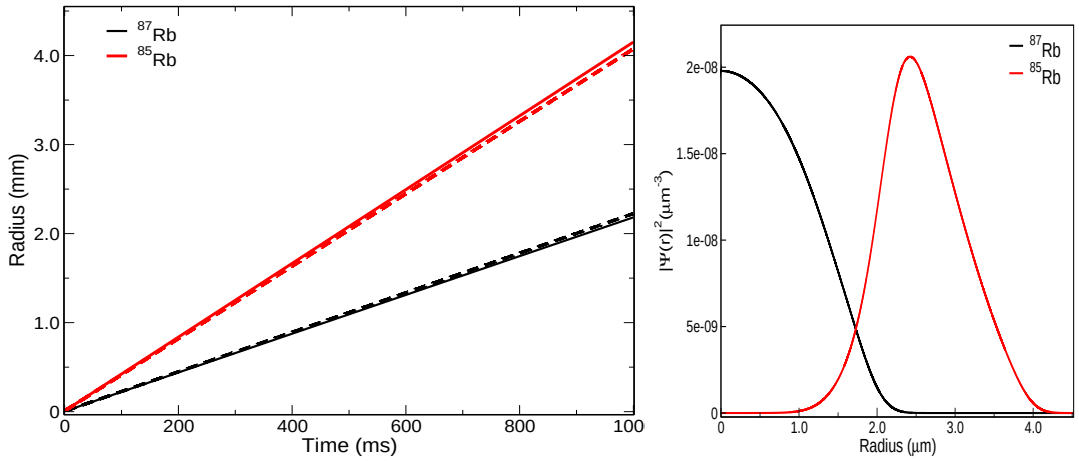

(a) Evolution of the radii. c-SA (dashed lines) and c-TDGPE (solid lines) results.

(b) Density profiles after 1s of expansion.

Figure 3.9: A balanced mixture of $N = 10^6$ of ^{87}Rb and ^{85}Rb expands freely upon release the trap with frequencies of Table 3.1. (a) shows the evolution of the radii during 1 s. In (b) the time-evolved density profiles of components at t =1 s. The Feshbach field is removed at time t =10 ms.

The $^{87}Rb/^{41}K$ mixture fig. 3.10(a) shows a good agreement between the results obtained with the two methods. The two gases coexist after a long expansion even if the magnetic field has been removed at early time of the expansion as can be seen in fig. 3.10(b). From fig. 3.10(a) one sees that the final sizes are not extremely large, this is because the trap potential used is not very deep. The expansion rates of ^{41}K and ^{87}Rb are $\sim 3\ mm \cdot s^{-1}$ and $\sim 2\ mm \cdot s^{-1}$ respectively.

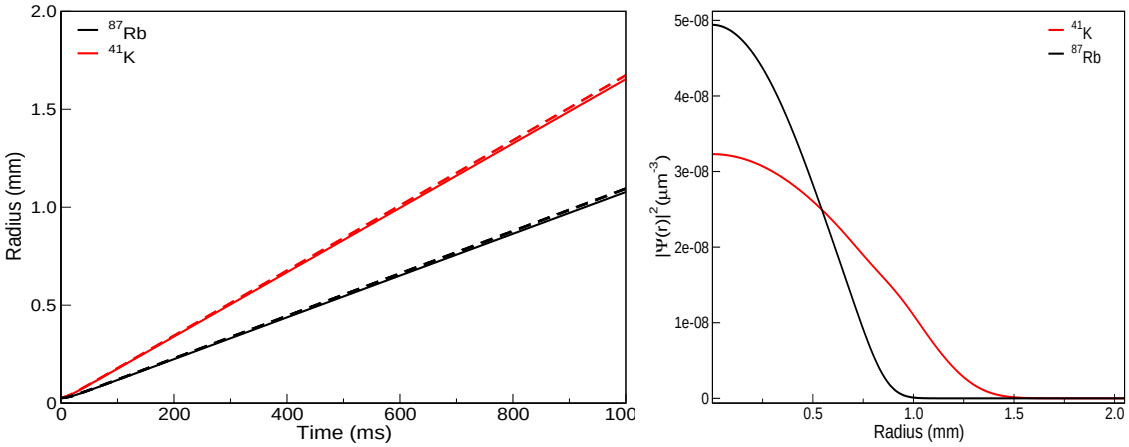

(a) Evolution of the radii. c-SA (dashed lines) and c-TDGPE (solid lines) results.

(b) Density profiles after 1s of expansion.

Figure 3.10: Free expansion of a mixture of ^{87}Rb and ^{41}K. In (a) the size evolution from a trap of frequencies indicated in Table 3.2. The Feshbach field is removed at t=200 ms. The two components stay overlapped after the long-time evolution.

The $^{87}Rb/^{39}K$ mixture fig. 3.11 shows the free evolution of the wave packets of fig. 3.7. There is a slight difference between the results by the two methods in fig. 3.11(a) which

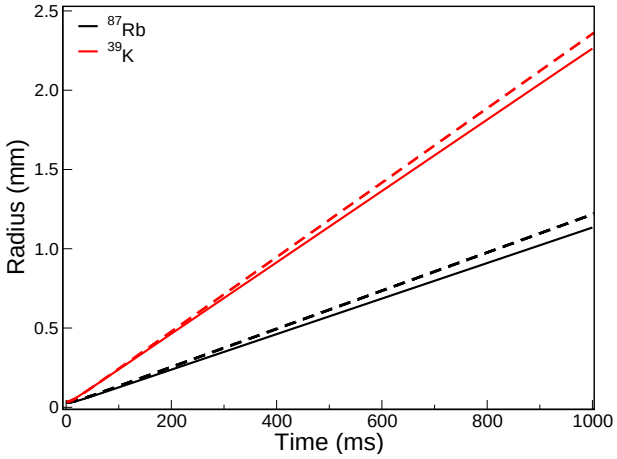

(a) Evolution of the radii. c-SA (dashed lines) and c-TDGPE (solid lines) results.

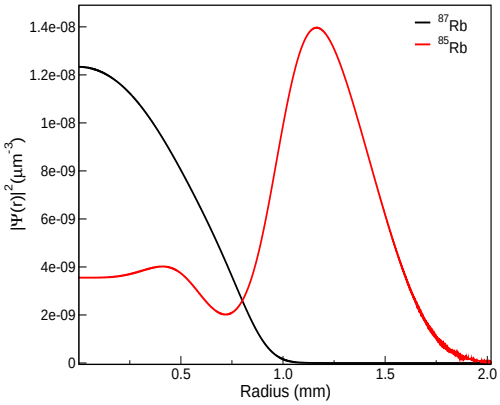

(b) Density profiles after 1s of expansion.

Figure 3.11: Evolution of a ^{87}Rb/^{39}K mixture. In (a), the time evolution of the radii of both components shows the faster expansion of the ^{39}K cloud. In (b), the density profiles after 1 s of expansion, the components separate due to the strong intra-species interaction of ^{39}K compared to other interaction terms. The parameters are shown in Table 3.3. The Feshbach field is removed at t =300 ms. The expansion rates obtained of ^{39}K and ^{87}Rb from (a) are of the order of ~ 3.5 $mm \cdot s^{-1}$ and ~ 1.8 $mm \cdot s^{-1}$ respectively.

is due to the non-trivial shape of the ^{39}K cloud which become more complex during expansion as can be seen in fig. 3.11(b). The shape of ^{39}K and the very different expansion rates of components extracted from fig. 3.11(a) indicate that for producing miscible and simultaneously collimated mixture a single-pulse DKC will not be sufficient.

The deformation observed in the ^{39}K density can be understood by comparing the change in time of the intra-species interaction energy of both components. In fig. 3.12, it is seen that even though the inter-component interaction is decreasing depicted in blue, the inter-atomic interactions in ^{39}K are decreasing faster than those of ^{87}Rb atoms yielding the central region to the latter ones. This is not the case of the other mixtures considered previously where the shapes of the densities are preserved during expansion.

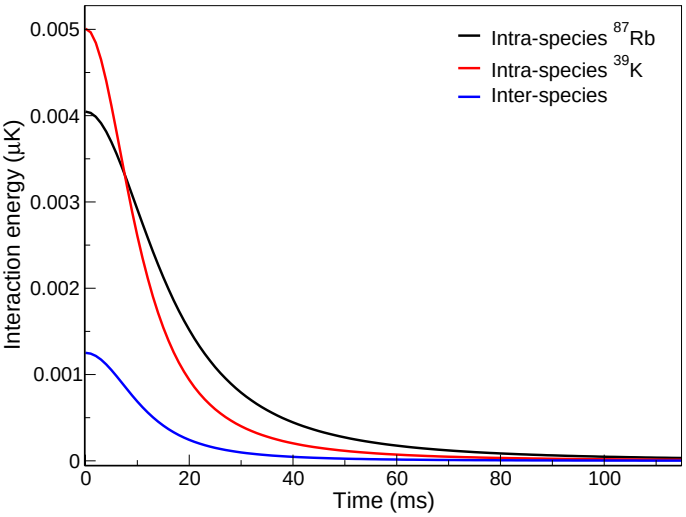

Figure 3.12: Interaction energies of the ^{87}Rb/^{39}K mixture The scattering lengths are $a_{87} = 99a_0$, $a_{39} = 100a_0$ (tuned with B=414 G) and $a_{39/87} = 34a_0$ The intra-species interaction energy of ^{39}K drops to a lower value than that of ^{87}Rb atoms starting at few milliseconds after release, which makes the ^{39}K cloud lose stability against ^{87}Rb causing a deformation and a separation of the components densities.

The $^{87}Rb/^{170}Yb$ mixture From fig. 3.13, in spite of the very large size that the mixture reaches after t =1 s of free expansion, the stability and miscibility of these two gases without need for an external magnetic field is noticed. The expansion rates are ~ 4.4 $mm \cdot s^{-1}$ and ~ 2.6 $mm \cdot s^{-1}$ for ^{87}Rb and ^{170}Yb respectively.

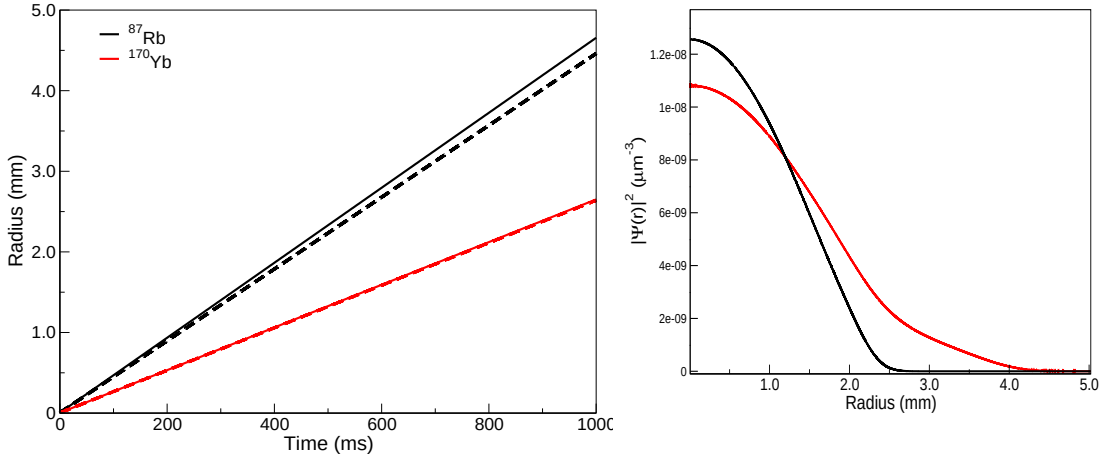

(a) Evolution of the radii. c-SA (dashed lines) and c-TDGPE (solid lines) results.

(b) Density profiles after 1s of expansion.

Figure 3.13: Long-time free evolution of the mixture ^{87}Rb/^{170}Yb. The parameters used are from Table 3.4. The two gases reach very large sizes after 1s of expansion due to the large trap frequencies used and the large mass of ^{170}Yb. From (b) the two components stay mixed and stable after t =1 s due to the small attractive inter-species interaction.

DKC and collimation of mixtures

The $^{87}Rb/^{85}Rb$ mixture It is necessary to control the final size of both condensates after a long time of expansion ($t_f = 11$ s), for this aim, DKC is applied with the same duration and timing to both samples. This reproduces the case of a DKC using a dipole trap. For ^{87}Rb/^{85}Rb mixture two cases have been considered, $N = 10^3$ atoms, and $N = 10^6$ atoms in each component.

For $N = 10^3$ atoms, the component clouds shown in fig. 3.14 are well collimated to a radius of about 1 mm at t =10 s, with a DKC applied at t^{start} =48.0 ms.

The small discrepancy observed between the two computation methods is because the TFA in which is based the c-SA is an approach for strongly interacting systems.

fig. 3.15 shows the same manipulation for large particles numbers (10^6 atoms). The slope of the expansion curve is dramatically reduced. Moreover, it can be seen that the two approaches (c-SA depicted with dashed lines and c-TDGPE with solid lines) are in a good quantitative agreement for this case. This is explained by the reduced effect of neglecting the kinetic energy in the SA for large potential interaction energies. The two gases are very nicely collimated by the DKC to a radius of about 3 mm at t =10 s.

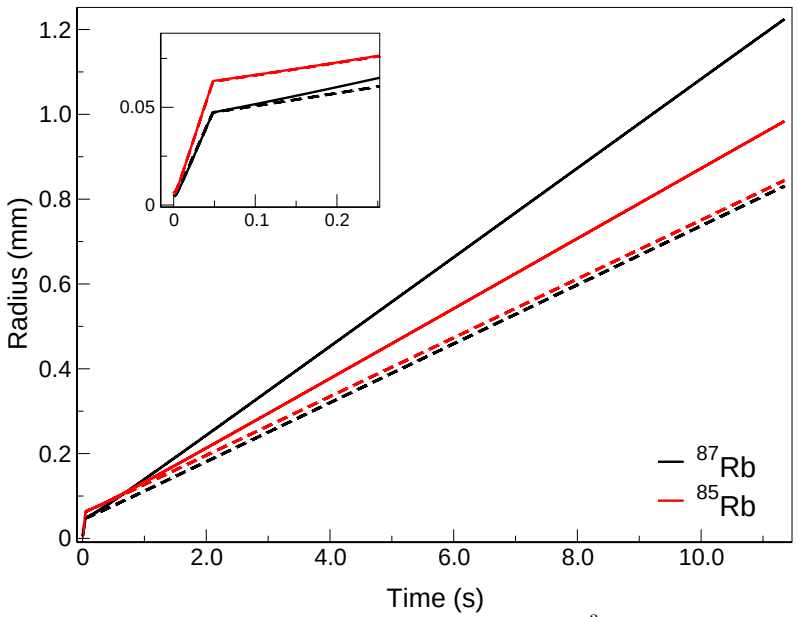

Figure 3.14: Size of the expanding two interacting gases of 10^3 atoms each, with DKC applied, a_{85}=900a_0 initially, and after waiting for 10 ms the magnetic field is removed leaving the ^{85}Rb in the regime of attractive interactions with a strength of $a_{85} = -443a_0$. DKC is applied at t^{start} =48 ms and stays during t_{dur} =0.302 ms, with the trap frequencies of Table 3.1. The inset is a zoom-in on the first 200 ms showing good agreement between the SA and the c-TDGPE. At long time, a discrepancy of about 35% with the numerical GPE solution is noticed.

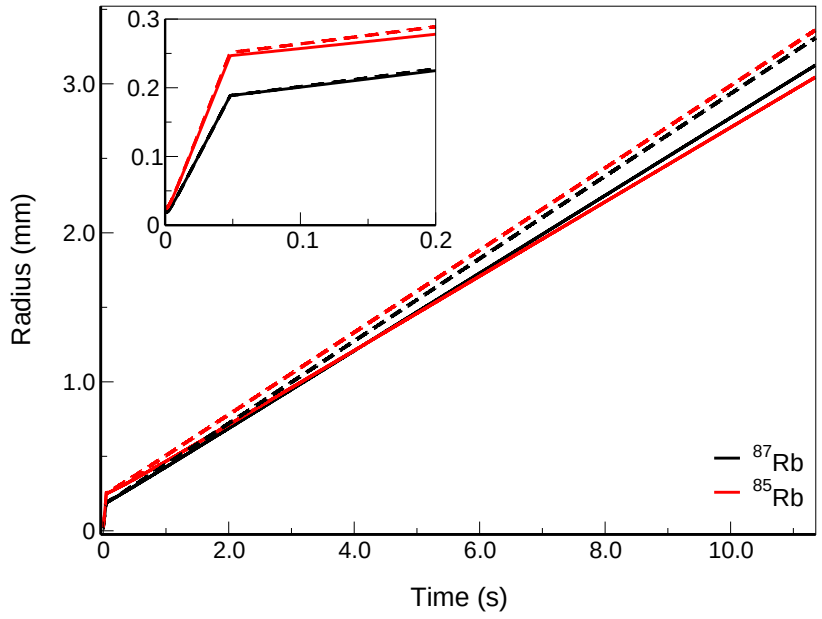

Figure 3.15: Time evolution of the radius of BECs of ^{87}Rb and ^{85}Rb with $N = 10^6$ atoms in each, with DKC applied. Initially a_{85}=900a_0, and after 10 ms, the ^{85}Rb atoms are allowed to attractively interact with a_{85}=-443a_0. DKC is applied at t^{start} =48.0 ms and stays during t_{dur} = 0.302 ms with the trap frequencies of Table 3.1. The inset is a zoom on the first 200 ms showing quantitative agreement, a discrepancy of about 25% with the numerical GPE solution is reported at long times.

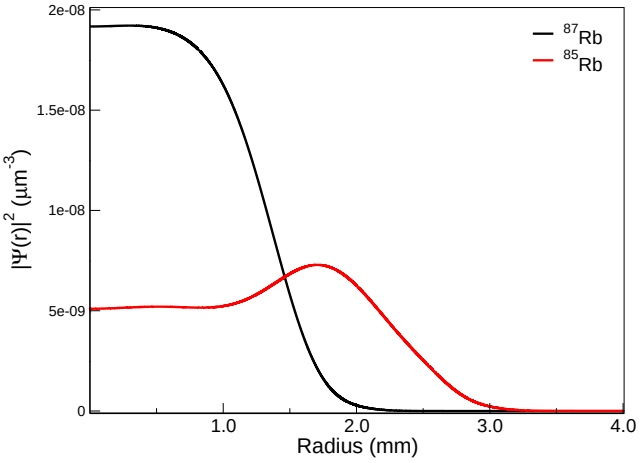

Figure 3.16: Density profiles of $N = 10^6$ atoms of ^{87}Rb and ^{85}Rb at t =11 s A DKC applied at t^{start} =48.0 ms with a duration t_{dur} =0.302 ms enhances the overlap between wave packets in more than 20%, the gases seem to be more mixed.

The $^{87}Rb/^{39}K$ mixture The miscibility of the ^{87}Rb/^{39}K mixture turns very weak during the dynamics as was obtained in fig. 3.11(a). The non-trivial shape of the density profiles observed during expansion in fig. 3.11(b) is still present with the application of a DKC at $t^{start} = 48.0\ ms$. After a time t =3 s of expansion the cloud reach a radius of more than 2 mm.

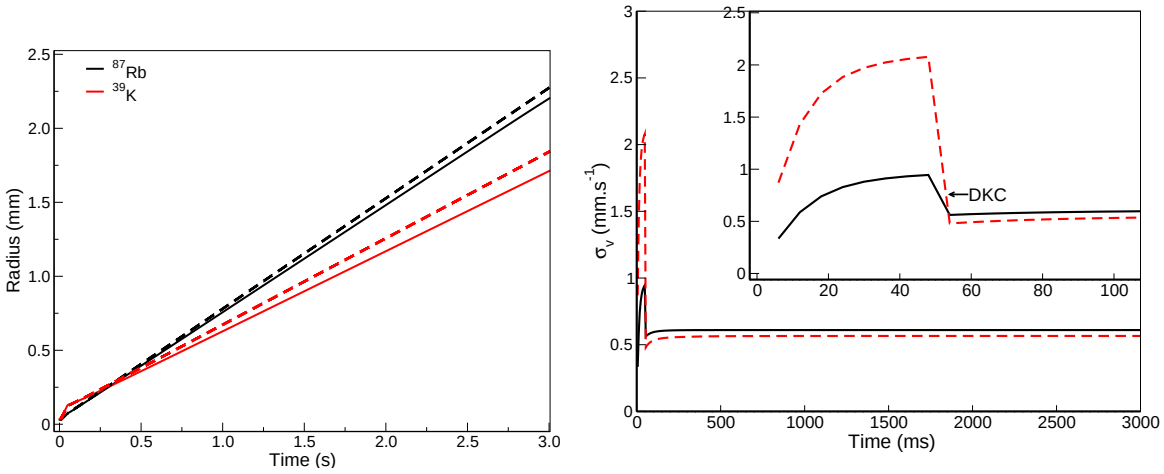

(a) Size of a mixture ^{87}Rb/^{39}K with a single DKC pulse applied.

(b) Velocity dispersion of mixture ^{87}Rb/^{39}K with a single DKC pulse applied.

Figure 3.17: An expanding bosonic mixture ^{87}Rb/^{39}K containing $N = 10^6$ atoms each, a_{39}=100a_0. DKC is applied at $t^{start} = 48.0\ ms$ with a duration of $t_{dur} = 2.6\ ms$. Solid lines in the size curves correspond to c-TDGPE solution, and dashed lines are for c-SA. The velocity dispersion curves (GPE) clearly show the reduction of the velocities as an effect of the DKC. The lens reproduces the initial traps of linear frequencies equal to 11.948 and 8 Hz for ^{87}Rb and ^{39}K respectively. At short time there is a very good agreement, whereas at long time it shows a discrepancy of about 25-35% with the numerical GPE solution.

The $^{87}Rb/^{170}Yb$ mixture As fig. 3.18 shows, for evolution times of about 1.5s, it is not necessary to use a multi-stage DKC. ^{87}Rb and ^{170}Yb can be simultaneously collimated to a final size of less than 2.5 mm

The stability and the high miscibility of this ensemble is confirmed from fig. 3.19 where the density profiles are shown to be gaussian-like and largely overlapped making this

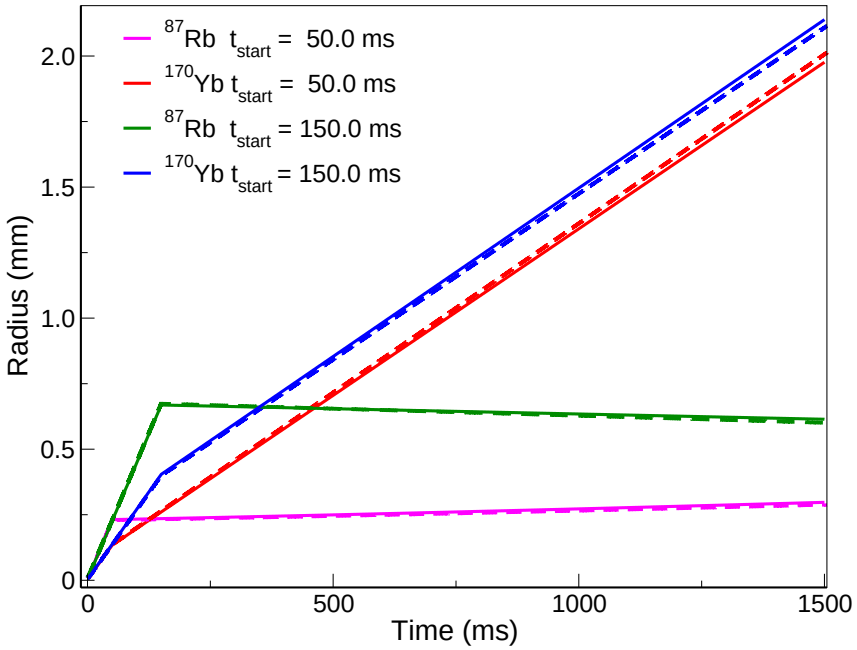

Figure 3.18: Time expansion of a ^{87}Rb/^{170}Yb mixture of $N = 10^6$ atoms each component. The two independent DKC procedures shown produced the same effect. A DKC applied at $t^{start} = 50.0ms$ has a duration of t_{dur}=0.064 ms, and that at t^{start}=150.0 ms lasts t_{dur}=0.022 ms. After a total expansion time of 1.5 s the mixture reaches a radius of about 2 mm. The scaling approach results are shown with dashed lines with the respective color of each case. Since the mixture is highly miscible the scaling approach works very well in this case.

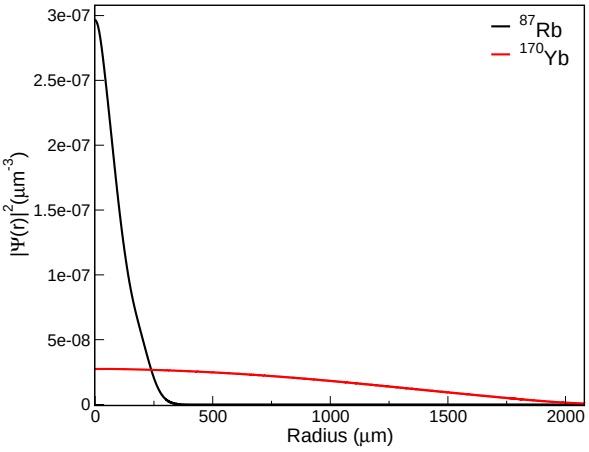

(a) A DKC has been applied at t^{start}=50.0 ms with t_{dur}=0.064 ms.

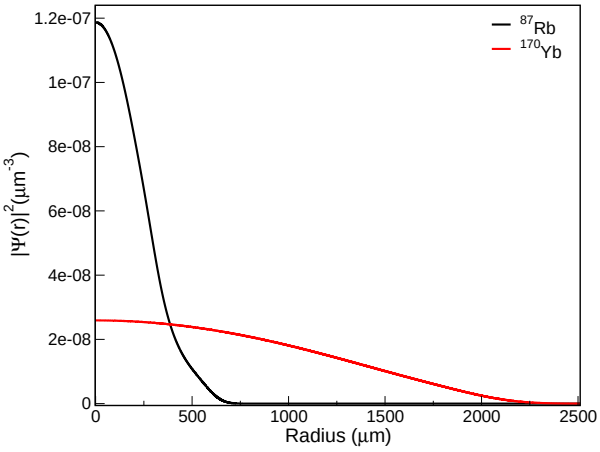

(b) A DKC has been applied at t^{start}=150.0 ms with t_{dur}=0.022 ms.

Figure 3.19: Effect of a single-pulse DKC on the density profiles of the mixture ^{87}Rb/^{170}Yb at $t = 1.5$ s. The two components are totally miscible and the shapes of the densities are gaussian-like after long expansion times and the re-trapping due to the large stability of this ensemble.

mixture an interesting source for applications requiring long propagation times.

Multiple DKC and collimation of mixtures of different atomic elements

Depending on the size and expansion rates requirement for a possible experimental implementation in each mixture, the application of a multi-stage DKC procedure can be needed. This is the case for instance of ^{87}Rb/^{41}K which is not very well simultaneously collimated, this is due to the very different masses which makes ^{87}Rb less sensitive to the application of a short pulse,

The $^{87}Rb/^{41}K$ mixture By looking at the expansion of the mixture fig. 3.21, it is clear that the presence of each sample dramatically affects the freedom of choosing the procedure to follow. One gas can be highly collimated by re-trapping it for a long time and allowing it to continue expanding at a very low speed. The other will not be collimated to a nice level with 1 pulse DKC due to the mass difference.

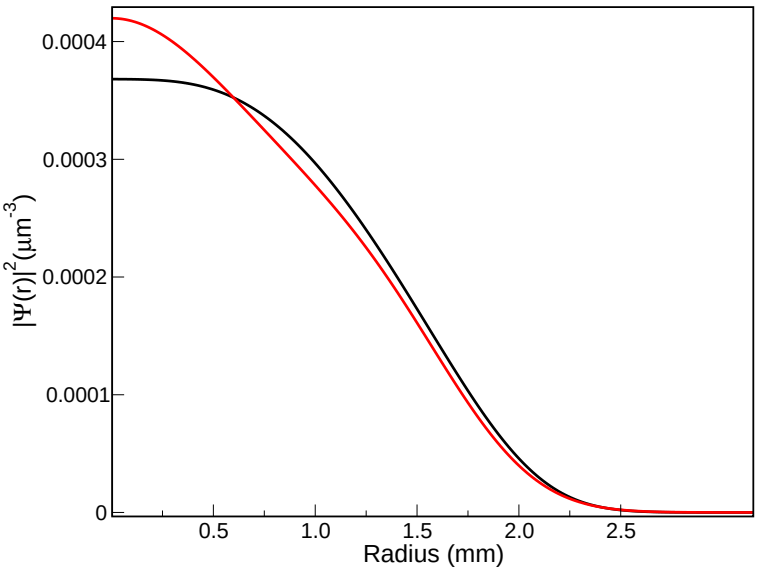

Figure 3.20: Density profiles of a non interacting mixture of $N = 10^6$ atoms of ^{87}Rb/^{41}K. The mixture is released from the trap and after a time t^{start} =20 ms is retrapped during t_{dur} =9.0 ms, and t^{start2} = 140.0 ms during t_{dur1} = 1.56 ms. The densities on the right figure correspond to a expansion time 9 s. The magnetic field is kept on during the first 200 ms of expansion, the condensates remain in the miscible state.

The effect of the application of the DKC two times is observed in the velocity dispersion profiles for the mixture components. in fig.3.22

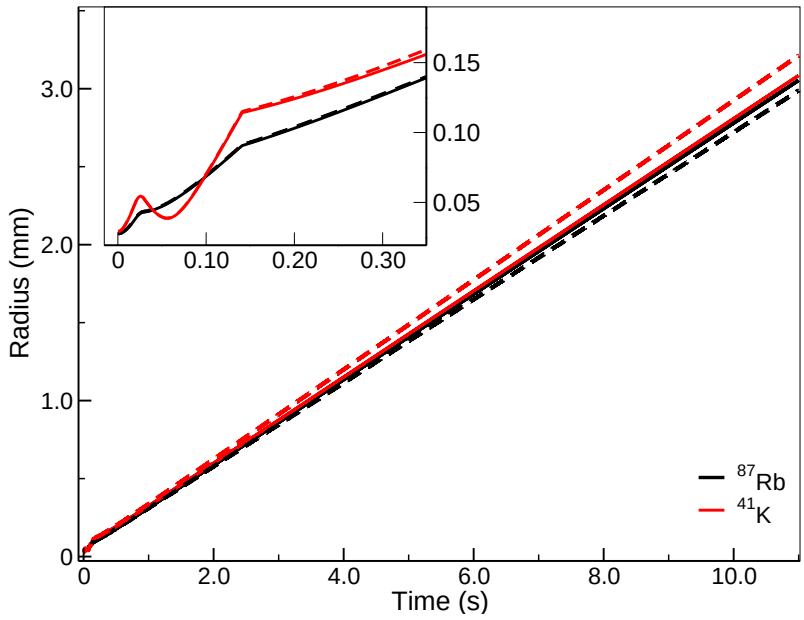

Figure 3.21: Evolution of the radius of 10^6 atoms of the ^{87}Rb/^{41}K mixture including application of DKC two times and turning on/off of a bias magnetic field. The bias magnetic field is taken off after 200 ms of expansion. The DKC is needed to be applied for two times: at $t^{start1} = 20.0\ ms$ with a duration of $t_{dur1} = 9\ ms$, and $t^{start2} = 140.0\ ms$ during $t_{dur1} = 1.56$ ms. The black line corresponds to the expansion of ^{87}Rb and the red one corresponds to ^{41}K. The inset is a zoom of the first 350 ms of expansion, where it can be seen clearly the times when DKC is applied. The results here are obtained by solving the c-TDGPE.

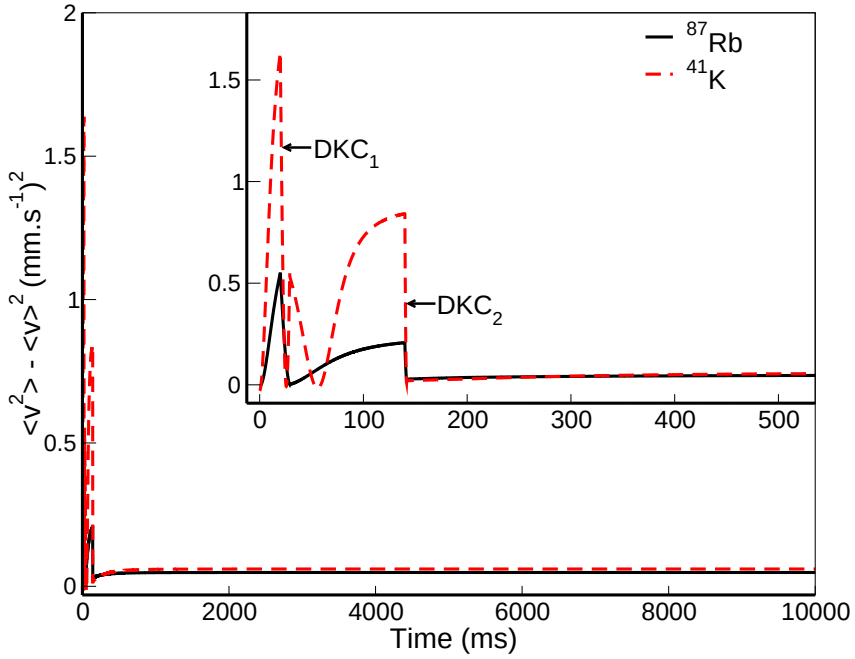

Figure 3.22: Velocity dispersion $\langle v^2\rangle - \langle v\rangle^2$ of 10^6 atoms of the ^{87}Rb/^{41}K mixture including application of DKC two times and turning on/off of a bias magnetic field. The DKC has been applied for two times: at $t^{start1} = 20.0\ ms$ with a duration of $t_{dur1} = 9\ ms$, and $t^{start2} = 140.0$ ms during $t_{dur1} = 1.56$ ms. The black line corresponds to the expansion of ^{87}Rb and the red one corresponds to ^{41}K. The inset is a zoom of the first 500 ms of expansion, where it can be seen clearly the times when DKC is applied.

3.4 Conclusion

In this chapter, an extension of the scaling approach to binary mixture condensates is made in the miscible regime. The static ground states for the miscible cases have been calculated by using the Thomas Fermi approach and the GPE finding a perfect agreement. The results obtained with this approach have been contrasted with the solutions of the coupled time-dependent Gross-Pitaevskii equations, finding qualitative and quantitative agreement. There have been observed some small discrepancies for long-expansion times possibly due to the fact the kinetic energy has been neglected which is a fundamental consideration for the scaling approach.

With the idea of overcoming the issues found in the ^{87}Rb/^{85}Rb mixture, a stable and overlapped ensemble of ^{87}Rb/^{41}K has been considered showing clear advantages, specially in miscibility and the expansion of the two components. It could be also collimated to a very high degrees for long observation times required in atom interferometry.

The convenience of operating an atom interferometer without high bias magnetic fields in the miscible case of ^{87}Rb/^{170}Yb makes it an excellent option to be implemented as a source in atom interferometry experiments in a field-free environment. It has been observed that this reach low interesting expansion rates.

CHAPTER 4

Degenerate mixtures sources for precision interferometry

In this chapter, we present some of the features required to prepare a suitable source for high-precision measurements in atom interferometry. We focus on the test of the weak equivalence principle proposed in [105, 169, 170] using high accuracy atomic sensors with condensates made of the two rubidium isotopes (^{87}Rb and ^{85}Rb) or different elements (^{87}Rb and ^{41}K) simultaneously cooled and trapped by lasers and magnetic fields. In this chapter, we study how to minimize systematic errors that arise in the realization of such an experiment.

4.1 Test of the Equivalence principle

The theories of Quantum Mechanics and General Relativity (GR) have allowed to understand and predict physical behavior in matter from subatomic particles to galaxies. GR is often discarded at short scales where quantum fluctuations, dominated by other fundamental forces, become relevant. The successful application of these two theories, each at characteristically different domains, often undermines their incompatibility. For more than a century GR and Quantum mechanics have not merged into a single theory, that can be treated as a quantum theory in the low limit of gravity, and as a GR theory in the large mass limit [171], and at the same time successfully describing the interaction forces when gravity is strong and distance is short. In this attempt to reconcile both theories is natural to think in reviewing some fundamental principles, in this sense the Equivalence principle is an excellent candidate since it is the empirical basis of the geometric description of gravity as suggested in GR while not being incompatible with Quantum mechanics. The equivalence principle has played an important role in the development of new theories as can be inferred from its many different versions, being the universality of free fall UFF the central part of all of them, [172, 173, 174], and the several tests done along the history[97, 175].

The weak equivalence principle (WEP) states that "all particles experience the same acceleration in a given gravitational field, or more precisely, that if an uncharged point like test particle is placed at an initial event in space-time and given an initial velocity there, then its subsequent trajectory will be independent of its mass and composition."

A test of WEP is quantified by the Eötvös ratio η [176], which compares the acceleration of two test bodies moving only under the influence of the gravitational field.

$$\eta = \frac{|a_1 - a_2|}{(a_1 + a_2)/2} \tag{4.1}$$

where $a_{1(2)}$ is the acceleration of body 1(2). If the principle is violated (violations are

expected to occur in the 10^{-13} to 10^{-18} range [177, 178]) , then these accelerations would differ from each other. The finding of a possible violation of WEP would have serious implications in the microscopic theories of gravity.

Nowadays there have been quantum and classical tests, which fundamentally differ from each other. In quantum experiments the most common atoms used are the alkali metals of bosonic/bosonic and bosonic/fermionic nature.

The high precision methods developed so far include ground and space-based experiments. The most robust to date is based on a Eötvös torsion balance [97] reaching an accuracy of 10^{-13} in the violation parameter η, and lunar laser-ranging reaching an accuracy of 10^{-13} [98].

Modern proposals are intended to use matter wave interferometry to test the WEP at the quantum domain by following the free fall evolution of two species of atoms isolated from other forces and measuring the phase shift that is related to the atom acceleration as it is described in sect. 4.2.

Within the ambitious projects currently being developed are fountain tests [5, 6, 170] with the goal of measuring $\eta \approx 10^{-15}$ by launching atoms in a vertical fountain geometry to maximize the free fall time and achieving a total interrogation time of up to few seconds. A mission from the French space agency, Microscope, is expected to reach an accuracy of $\eta = 10^{-15}$ [179]. The proposed Space-Time Explorer and Quantum Equivalence Principle Space Test (STE-QUEST), motivates this work. This space mission was planned for an extended free evolution time of 10 seconds. The mission was designed to operate in a satellite with ^{87}Rb and ^{85}Rb (or ^{87}Rb and ^{41}K) in the Earth gravitational field and the goal was to obtain a sensitivity η of 10^{-15} [105, 115, 116, 180].

For testing the WEP at the atomic level it is necessary to take into account many aspects that will influence the trajectories of the test masses. Before clarifying some limits emerging due to environmental conditions and proposing solutions to minimize their impact in a future experimental realization, a short introduction to fundamental aspects on matter wave interferometry which is used to measure the gravity acceleration g is presented.

4.2 Basic concepts on matter wave interferometry

Atom interferometers (AI) were primarily demonstrated in 1991 based on different techniques [11, 77, 181, 182]. We discuss an AI in a Mach Zehnder geometry as it is mainly used in this work, and we review the requirements for precision measurements on which we work for the different quantities analyzed in this work. A complete description of different configurations of atom interferometers is well described in [90] and papers [80, 183]. The physical principle of the AI is similar to that of an optical interferometer in which a light beam is split and reflected by means of optical beam splitters and mirrors, for which the optical path difference results in a particular phase difference.

The atom interferometer considered in this work uses three laser pulses tuned on the two-photon Raman transitions of ^{87}Rb and ^{85}Rb, which symmetrically split, reflect, and recombine the trajectories of the atoms.

4.2.1 Mach-Zehnder Interferometer $\frac{\pi}{2} - \pi - \frac{\pi}{2}$

A Raman transition between two hyperfine states of an atom $|1\rangle$ and $|2\rangle$ is driven by two counter-propagating laser beams of frequencies ω_1 (and a phase ϕ_1) and ω_2 (and a phase ϕ_2) when

$$\hbar\,(\omega_2 - \omega_1) = E_2 - E_1, \tag{4.2}$$

where for this case, the laser frequencies are chosen exactly at resonance. The intermediate state $|i\rangle$ is not populated in this transition because the beams do not excite a single-photon transition. The two states $|1\rangle$ and $|2\rangle$ are coupled by a Raman transition and Rabi oscillations are driven between the states, e.g. when the atom starts in state $|1\rangle$ a $\frac{\pi}{2}$-pulse builds a superposition of states $|1\rangle$ and $|2\rangle$ with equal amplitudes, see fig. 4.1.

The momentum of the beams is transferred to the atoms during the transition. The atom receives a two recoil kick, in the same direction by the absorption of one photon of wave vector $\vec{k}_1$ and the stimulated emission of another one of wave vector $\vec{k}_2 \simeq -\vec{k}_1$, whose magnitude can be called k. This process results in the coupling of the states $|1,p\rangle$ and $|2,p+2\hbar k\rangle$.

A complete Raman interferometer sequence is shown in fig. 4.2. The atoms initially in the state $|1,p\rangle$ travel through an array of three interaction regions. The first one is a $\frac{\pi}{2}$-pulse which brings the atoms into the superposition state

$$|\Psi\rangle = C_1|1,p\rangle + C_2|2,p+2\hbar k\rangle = |1,p\rangle + e^{i\phi'}|2,p+2\hbar k\rangle \quad , \tag{4.3}$$

where C_1 and C_2 are complex coefficients defining the phase ϕ', which depends on the relative phase of the two laser beams. From eq. (4.2.1) one sees that these states separate, meaning a spatial separation of the atom's wave packet, as it is shown in fig. 4.2, therefore this first pulse is equivalent to a beam splitter.

After some time T corresponding to the duration of the free evolution pulse, and traveling a distance L the atoms reach a second region of interaction undergoing a π-pulse which acts on the two paths A and B to reverse the states $|1,p\rangle \rightarrow |2,p+2\hbar k\rangle$. After a time T and having traveled a distance L, the atoms are mixed together with a $\pi/2$-pulse acting to produce an interference pattern. This sequence is called a Mach Zehnder Interferometer, and $|1,p\rangle$ and $|2,p+2\hbar k\rangle$ define the two output channels from where, the phase shift is measured.

The phase read-out

The total phase difference between the two paths A and B in the interferometer is derived from three contributions, discussed in [184] for example:

- A propagation phase, coming from the evolution of the atom between light pulses,

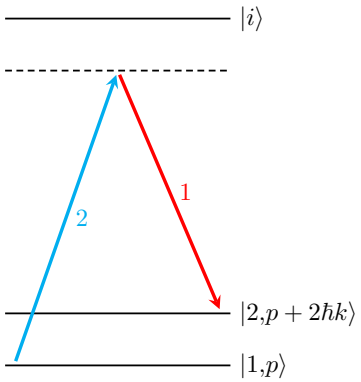

Figure 4.1: Level diagram of a stimulated Raman transition. Two laser beams with frequencies ω_1 and ω_2 which propagate in opposite directions, drive a Raman transition between the states $|1\rangle$ and $|2\rangle$ with a difference between the energies $\Delta = E_2 - E_1$. The Raman process couples the states $|1,p\rangle$ and $|2,p+2\hbar k\rangle$. The intermediate state is not populated in this transition.

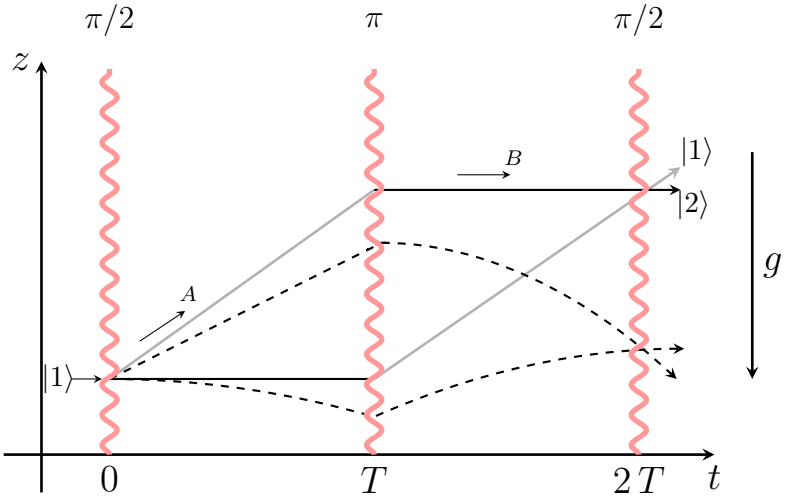

Figure 4.2: Mach-Zehnder atom interferometer. The sequence starts at time $t = 0$ when a $\pi/2$ pulse, equivalent to a beam splitter, is applied to coherently divide the atom wave function. After a time T, a π pulse is applied, playing the role of a mirror reversing the relative velocity between parts of the wave packet. At the end, after a time T, another $\pi/2$ pulse is applied, resulting in the interference of the wave packets along the two paths. As an output the interferometer measures the probability of detecting in one of the states $|1\rangle$ or $|2\rangle$ to determine the phase shift. In the presence of a linear acceleration g, the wave packets trajectories are not straight lines but curves, this is shown by dashed lines.

and it is found from the classical action integral along each path (A/B).

$$\Delta\phi_{1\to 2} = \frac{1}{\hbar}\left[S_{cl}^{B} - S_{cl}^{A}\right] \quad , \tag{4.4}$$

where S_{cl} is the classical action defined in terms of the Lagrangian of the system $\mathcal{L}$

$$S_{cl} = \int_0^{2T} \left[L\left[z(t),\dot{z}(t)\right] - E_i\right] dt \qquad , \quad L = T - V = m\vec{v}^2/2 - mgz. \tag{4.5}$$

where E_i is the energy of the internal atomic level. T and V are the kinetic and the potential part in the Lagrangian function.

- A laser phase, coming from the phase difference due to interaction between atoms and lasers in the beam splitters. Due to the atom-light interaction, the atoms acquire the phase of the laser ϕ_L causing the state gains (+) or loses (-) momentum.

$$\Delta\phi_{laser} = \sum_{j,B} \pm\phi_L(t_j, z_B(t_j)) - \sum_{j,A} \pm\phi_L(t_j, z_A(t_j)) \tag{4.6}$$

where the sum takes into account the contributions of all interaction points at times t_j, and $z_{B(A)}$ are the classical trajectories of the two arm A/B of the interferometer, respectively.

- A separation phase, arises from the splitting of the wave packets at the outputs, since the classical trajectories of the two paths do not cross each other at the exit of the interferometer necessarily.

The separation between the arms is $\Delta z = z_B - z_A$ resulting in a phase shift

$$\Delta\phi_{separation} = \bar{p}\Delta z/\hbar \tag{4.7}$$

where $\bar{p}$ is the final classical canonical momentum of the atom.

It has been demonstrated that the propagation and separation phase contributions cancel each other [185], remaining the laser phase contribution.

Without the influence of the gravitational field the trajectories are just straight lines (black solid lines in fig. 4.2) and the symmetry in that case leads to $\Delta\phi = 0$. A breaking of this symmetry is produced by introducing a gravitational field, this is shown by dashed lines in fig. 4.2. Applying a force to change the atom's motion is equivalent to apply a phase gradient to the wave function, in this case it has been found [185] that the phase from the classical atomic trajectory is proportional to the gravitational acceleration g, namely

$$\Delta\phi = k_{eff} g T^2. \tag{4.8}$$

This expression is slightly modified due to the gravity gradient tensor:

$$T = \vec{\nabla}\cdot\vec{g}\,, \qquad \vec{g}(\vec{r}) = -\vec{\nabla}\vec{\Phi}(\vec{r}) \tag{4.9}$$

where $\vec{\Phi}$ is the gravitational potential. For the conservative field,

$T_{ij} = T_{ji}$ and $\vec{\nabla}^2\vec{\Phi} = 0$ giving $T_{xx} + T_{yy} + T_{zz} = 0$.

The gravity gradient due to the mass of the Earth is:

$T_{xx} = T_{yy} = g/R, T_{zz} = -2g/R$ with R the radius of the Earth and the crossed components are zero [186].

Hence the gravitational field modifies the phase shift by the additional terms

$$\begin{aligned} &T_{zz}\Delta z k T^2 \\ &T_{zz}\Delta v_z k T^3 \end{aligned} \tag{4.10}$$

The gravitational gradients are found to be extremely small for typical experimental parameters, and even more so when it has been chosen isotopes with very close mass values. However in high precision measurements, the effect can be critical giving rise to biased terms that may accelerate the atoms.

The phase shift measured in the interferometer is also modified by centrifugal and Coriolis forces due to Earth rotation and by magnetic fields used during the preparation of the components. They have a perturbative effect in the phase shift and hence in the expected sensitivity of the test. We have calculated such effect using the experimental parameters of the project.

4.3 Requirements on a suitable source for STE-QUEST [105]

The aim of the STE-QUEST proposal is to test the universality of free fall to an uncertainty of 2×10^{-15} by using the two isotopes ^{87}Rb and ^{85}Rb in an atom interferometer. Such a high accuracy has certain requirements in technical aspects and some of them directly related to the source, these are:

- Large number of atoms N is needed to increase the phase sensitivity of the interferometer $\Delta\phi$. The use of large condensates helps in preventing large projection

noise fluctuations that scale as $\sqrt{N}/N$, which for the number of atoms considered for the proposal, this is $N = 10^6$, such shot noise is of the order of $\sim 10^{-3}$.

- The fact that BECs have long coherence lengths and expand slowly during long interrogation times ensures high contrast, and allows a signal detection after several seconds. BECs also help reducing the wavefront errors
- A common-mode noise rejection required for the differential acceleration can be achieved by a simultaneous preparation and interrogation of the atomic samples.
- There are other fundamental limits on the sensitivity of the interferometer, eg. gravity gradients on the differential acceleration. It is possible to reduce their impact by preparing an ensemble with a high level of miscibility of the component gases, which is given by enhancing the overlap of density profiles of the atomic ensembles.

The interferometry sequence starts after the prepared source of the two Rb isotopes reaches an expansion in the linear regime of interactions to prevent a possible dephasing associated with the mean field effects producing loss of interferometric contrast. The first stage starts with a mixture in the Feshbach field which is kept for 10 ms. The next step is to apply the DKC procedure to collimate the clouds and slow down the expansion rates in order to reach a temperature of $T_0 70pK$, equivalent to a expansion rate of $82\mu m/s$, knowing that $\frac{1}{2}k_B T_0 = \frac{1}{2}mv^2$, where the temperature is named by T_9 in order to aovid confuse it with the interrogation time T.

4.4 Controlling the size and the expansion rates of expanded clouds by DKC

Along this chapter, we are making use of techniques that allow to reduce several systematic errors present in high precision measurements in an atom interferometer.

Therefore the expansion rates should be simultaneously reduced and matched at the order of at least 10^{-3} to minimize the differential speed, and a speed of about $82\mu m \cdot s^{-1}$ in each species, equivalently to a temperature of $\sim 70pK$. This is also facilitated by the fact that the gases are condensed rather than thermal, since they have low expansion rates leading to small ensembles even after a long time of expansion.

It has been already discussed how the DKC technique acts reducing the size of the clouds for momentum width reduction in sect. 2.1.5. In the present section, specific results of the mixture ^{87}Rb/^{85}Rb are shown for the specific requirements of the project.

The DKC as analogous to optical lenses, can be used to collimate the atomic beam. DKC works efficiently for single species, being easily achieved a very low slope of the linear expansion, this can be seen for instance in fig. 4.3, where the atoms have been re-trapped at different timings and with different durations. Now, in order to justify the DKC sequences applied in our mixtures, we consider the following cases: individual samples of ^{87}Rb, ^{85}Rb and ^{41}K and then the corresponding mixtures.

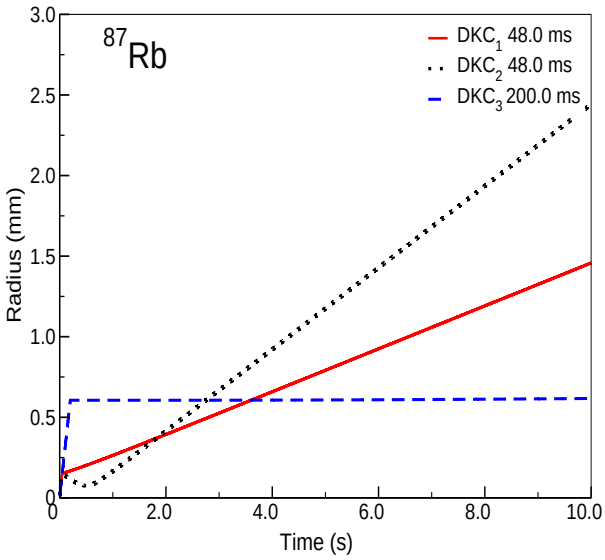

Figure 4.3: DKC effect on a ^{87}Rb condensate of $N = 10^6$ atoms. Time evolution of the radius over 10 s, for different starting and duration times of the DKC. The dotted black line is for $t^{start} = 48.0$ ms and has a duration of $t_{dur} = 0.302$ms, for the solid red line DKC starts at same time with a longer duration of 0.34 ms, and the dash-dot blue line the DKC starts at $t^{start} = 100.0$ ms during $t_{dur} = 0.156$ ms. When DKC is applied at later time $t^{start} = 200.0$ ms during $t_{dur} = 0.078$ms (dashed turquoise line), the expansion rate has flattened at extremely low expansion rates. The trap is spherically symmetric with frequencies $\omega = 2\pi \times 40$ Hz.

In fig. 4.3 different cases produced by the DKC are shown for an ensemble of $N = 10^6$ atoms of ^{87}Rb in a spherically symmetric harmonic trap with frequencies $\omega = 2\pi \times 40$ Hz. One can see that when the atoms stay in the trap for a long time the atoms go into a 'focal point' and the size diverges to very high values, in general depending on the starting and duration of the DKC, the frequencies; this is depicted in the black dotted line, where the trap has been switched on at $t^{start} = 48.0$ ms and kept for $t_{dur} = 0.34$ms. One can reach a regime where the size stays almost constant during the whole expansion time and optimizing the expansion rate ($\sim 2.4\mu m/s$) to maximum. This is the case for the dashed turquoise line where the DKC has been applied at $t^{start} = 200.0$ ms during $t_{dur} = 0.078$ms, when the condensate is already in the linear regime, expanding with a constant velocity. This seems to be a good case for producing an optimum collimation of the ensemble which is true in a single-species condensate even when it has reached a size of almost 1.2 mm which widely surpasses the size of the trap. Another similar case is shown by the dash-dot blue line where the velocity of expansion is highly reduced, $\approx 27\mu m/s$. At the moment of starting the DKC, the condensate was expanding at 3mm/s velocity and having a size $\approx 600\mu m$. Such a sequence is sufficiently good with single-species condensates and without limitations of the size at the moment of starting the dynamics.

The BEC is highly collimated when the DKC is applied at the right time and with the proper duration, this is the case of the solid red line; if the DKC acts for a long time the BEC comes into a " focal point" diverging to a larger radius as shown by the solid red line. This case was already exposed in fig. 3.15 in page 57, giving an optimum input for AI. This shows the role of the waiting time to start re-trapping the condensate as well as its duration on deciding the dynamical properties of the condensates. The trap during DKC is the same used for producing the condensate.

In fig. 4.3 efficient DKC procedures are shown for ^{87}Rb. The same atomic lens has to be applied to the other component of the mixture ^{85}Rb (or ^{41}K).

In a condensate of $N = 10^6$ atoms of ^{85}Rb with repulsive interactions, the scattering length has been tuned to $a_{85} = 900a_0$ and kept during the first 10 ms of expansion. It is trapped in a spherically symmetric harmonic trap with frequencies $\omega = 2\pi \times 40$ Hz.

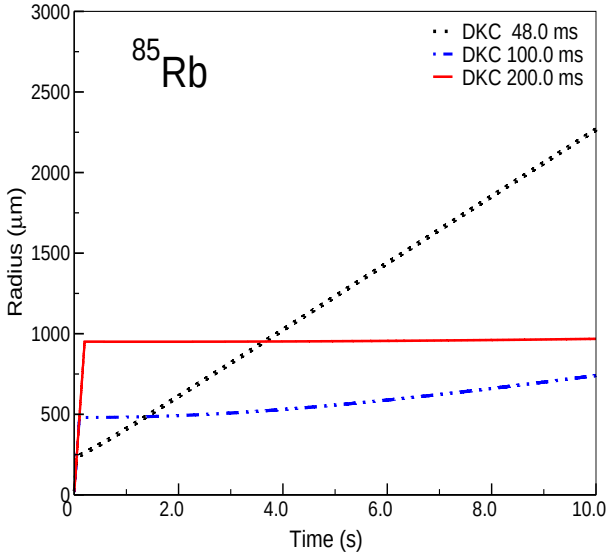

Figure 4.4: DKC effect on a ^{85}Rb condensate consisting of $N = 10^6$ atoms and $a_{85} = 900a_0$. Change in radius in 10 s of expansion for different starting and duration times of the DKC. A short lens is applied at $t^{start} = 48.0$ ms lasting $t_{dur} = 0.302$ms (dotted black line). The dashed blue line shows the evolution of the size by starting DKC at $t^{start} = 100.0$ ms by $t_{dur} = 0.156$ ms. For a DKC applied at $t^{start} = 200.0$ ms during $t_{dur} = 0.078$ ms, the expansion rate shows very low expansion rates as happened in same case for ^{87}Rb. The trap frequency is $\omega = 2\pi \times 40$ Hz in all directions as in previous case of ^{87}Rb.

Here the same DKC treatment is applied as in a previous case with ^{87}Rb. DKC is first applied to produce a nearly constant expansion rate (dashed blue line) similar to the case of ^{87}Rb. The cloud has reached a very large size –nearly 2 mm– which left it discarded to operate in an interferometer, regardless of the expansion rate as it does not meet our requirements [105]. In the second case, unlike the ^{87}Rb, the size of the condensate surpasses the capabilities of the dipole trap. At $t^{start} = 100.0$ ms and $t_{dur} = 0.156$ ms the cloud of ^{85}Rb already reaches a very large size ($\sim 1mm$), the expansion rate is now $v_{85} \sim 40\mu m/s$, far from matching the v_{87}. Another issue seems to be the size; the black line is the time evolution of the radius for a DKC applied at $t^{start} = 48.0$ ms lasting $t_{dur} = 0.302$ms, the corresponding expansion rate is $v_{85} \sim 207\mu m/s$.

The other sample widely studied here is ^{41}K prepared with the same protocols and trap features as the cases above. The solid red line, dashed blue line and dotted black line show the size evolution of the following DKC: The red line, with $t^{start} = 48.0$ ms and $t_{dur} = 0.302$ms, exhibits a similar behavior to the observed in ^{85}Rb, however the high difference in mass value with respect to ^{87}Rb forces us to think that the trap used in a possible mixture will be much tighter than the one for ^{87}Rb atoms allowing these to reach larger sizes quickly.

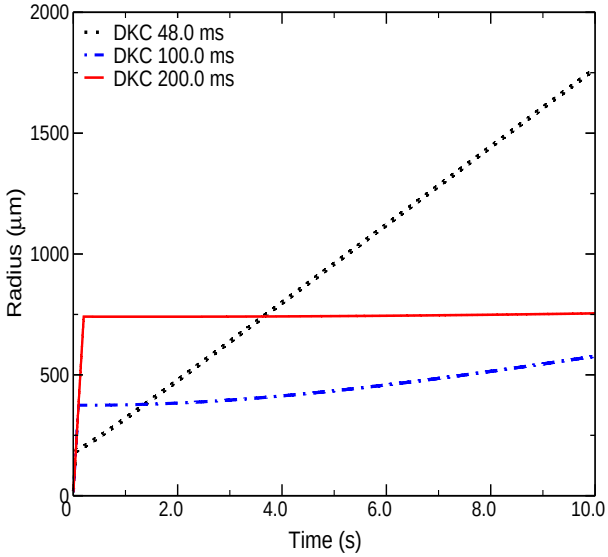

Figure 4.5: DKC effect on a condensate of $N = 10^6$ atoms of ^{41}K evolving for 10 s. The same DKC protocols used for the two samples above are used in this ensemble. The dotted black line shows the effect of DKC starting at $t^{start} = 48.0$ ms and with a duration of $t_{dur} = 0.302$ms. The dashed blue line shows the DKC starting at $t^{start} = 100.0$ ms during $t_{dur} = 0.156$ ms. Lastly the flattening of the expansion curve is obtained applying again DKC at $t^{start} = 200.0$ ms during $t_{dur} = 0.078$ ms (solid red line). A spherically symmetric trap was used, with a frequencies $\omega = 2\pi \times 40$ Hz.

Table 4.1: Summary of radii and expansion rates of ^{87}Rb, ^{85}Rb and ^{41}K. Each ensemble has the same number of atoms $N = 10^6$ and frequencies $\omega = 2\pi \times 40$ Hz. Three sets of the DKC shown in fig. 4.3, fig. 4.4 and fig. 4.5 are related here. Second column, a lens starting at $t^{start} = 48.0$ ms with a duration $t_{dur} = 0.302$ms. Third column $t^{start} = 100.0$ ms with a duration $t_{dur} = 0.156$ms. Fourth column $t^{start} = 200.0$ ms with a duration $t_{dur} = 0.078$ms. Notice that here are shown the values of the radii (R) at the moment of starting the DKC. The expansion rates are calculated when the clouds are linearly expanding.

Isotope	R(μm) / $v(\mu m/s)$ $t^{start} = 48.0$ ms	R(μm) / $v(\mu m/s)$ $t^{start} = 100.0$ ms	R(μm) / $v(\mu m/s)$ $t^{start} = 200.0$ ms
^{87}Rb	148.8/144.4	306.0/25.6	601.5/2.4
^{85}Rb	236.0/207.2	480.0/40.2	950.6/3.6
^{41}K	184.1/161.2	374.3/31.3	740.8/2.8

The radii and expansion rates obtained for the different DKC protocols applied to the ensembles ^{87}Rb, ^{85}Rb and ^{41}K are summarized in Table 4.1. As a common result for all samples, very low expansion rates were obtained when DKC is applied later, at $t^{start} = 100.0$ ms and $t^{start} = 200.0$ ms.

A mixture of ^{85}Rb/^{87}Rb with $N = 10^6$ atoms each are simultaneously trapped in harmonic traps of frequencies $\omega_{85} = 2\pi \times 40$ Hz, $\omega_{87} = 2\pi \times 39.5376$ Hz (correction due to the different masses of the two isotopes) for ^{85}Rb and ^{87}Rb respectively.

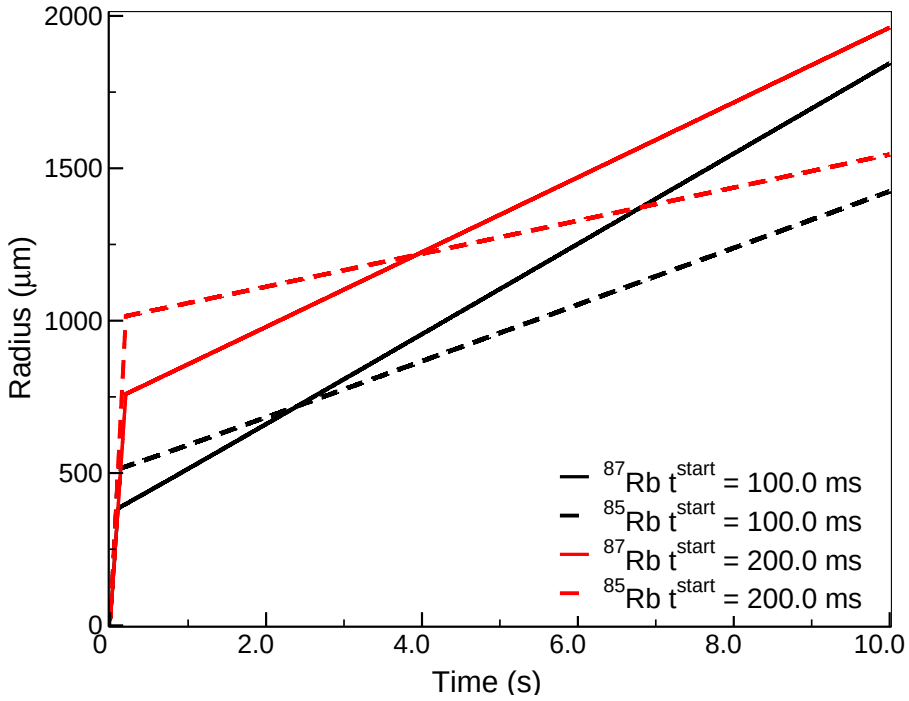

Figure 4.6: Effect of DKC in a mixture of ^{85}Rb/^{87}Rb with $N = 10^6$ atoms each component. The same DKC sequences have been applied for the mixture. The frequencies have been modified due to the different masses ($\omega_{85} = 2\pi \times 40$ Hz, $\omega_{87} = 2\pi \times 39.5376$ Hz), but the trap geometries are still spherical. The solid lines show time evolution of the radii where DKC has been applied at $t^{start} = 100.0$ ms during $t_{dur} = 0.156$ ms, and the dashed lines show the effect of applying DKC at $t^{start} = 200.0$ ms during $t_{dur} = 0.078$ ms. ^{87}Rb is in black and ^{85}Rb in red. The scattering lengths are $a_{87} = 100a_0$, $a_{85} = 900a_0$ and $a_{85-87} = 213a_0$

The highly collimated cases obtained in individual samples are used again for the mixture. From the fig. 4.6 it is evident that the lens configurations are not sufficiently

appropriate for reducing the size and the expansion rates for both gases simultaneously. Because the ^{87}Rb trap is slightly shallower than the one of ^{85}Rb, the former one expands faster than the latter. The interspecies interaction is repulsive, this contributes to enhancing the initial size of the condensates. In these cases, the following ratios between expansion rates were found: $\eta = v_{87}/v_{85} \approx 1.256$ and 1.371 for a DKC applied at 100 ms and 200 ms, respectively. This is the reason why being independently highly collimated with these DKC protocols has not been chosen for being the interferometer input instead of the one in fig. 3.15 which has a ratio between expansion rates matched to ~ 0.9994.

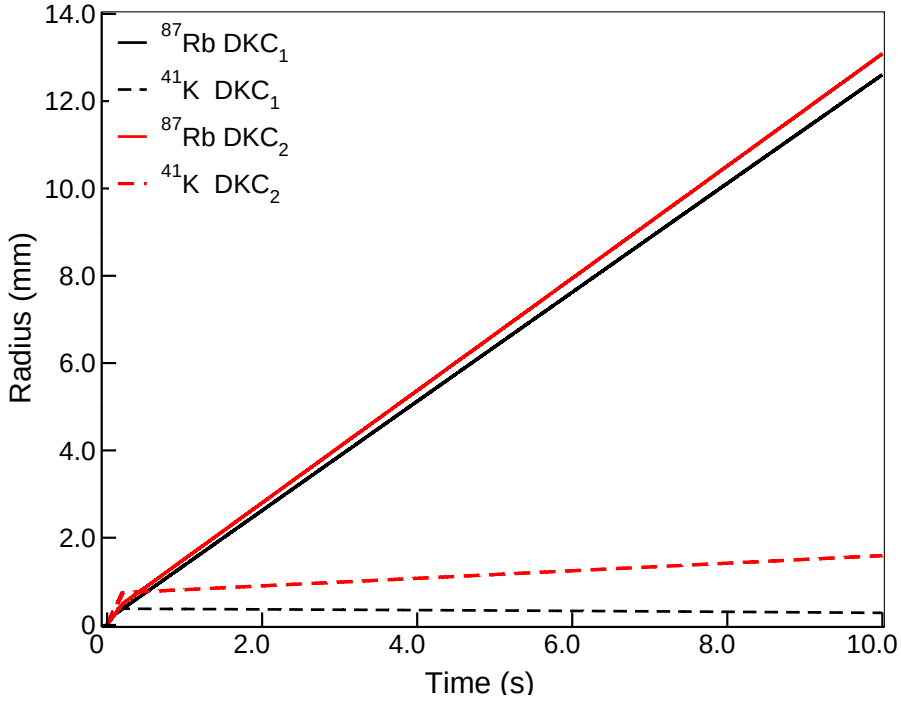

Figure 4.7: Effect of DKC in a mixture of ^{41}K/^{87}Rb with $N = 10^6$ atoms in each component. The same DKC sequences have been applied for the mixture, The frequencies have been modified by the gravitational sag ($\omega_{41} = 2\pi \times 40$ Hz, $\omega_{87} = 2\pi \times 25.4954$ Hz), but the trap geometries are still spherical. The solid lines show the time evolution of the radii where DKC has been applied at $t^{start} = 100$ ms during $t_{dur} = 0.156$ ms, and the dashed lines show the effect of applying DKC at $t^{start} = 200.0$ ms during $t_{dur} = 0.078$ ms. ^{87}Rb is in black and ^{41}K in red. From the notorious difference in the radii, it is evident the need for applying DKC for a second time. The inter-species scattering length has been tuned to $a_{41-87} = 0a_0$ for the first 300 ms of expansion.

By waiting longer to apply the DKC as done in fig. 4.8 where the $t^{start} = 1$ s, it is possible to collimate the expansion curves, but this is limited by the maximum size that the condensate can reach in the experiment.

In fig. 4.7, the same sequences previously used in the mixture of Rb isotopes are considered, now in a ^{41}K/^{87}Rb mixture. The components are free since the scattering length has been tuned to zero during the first 300 ms of expansion; the trapping frequencies are much more different from each other making the two components develop different expansions as they are released. The component ^{87}Rb as it is subject to a shallower trap, needs considerably longer times for producing a sensible change in its dynamics. From these curves we can conclude that it is necessary to re-trap the atoms at least for a second time to obtain a satisfactory input for precision interferometric measurements. This is as well shown in fig. 4.12, page 79, where it has been found an optimized DKC configuration of a collimated mixture where both components have very

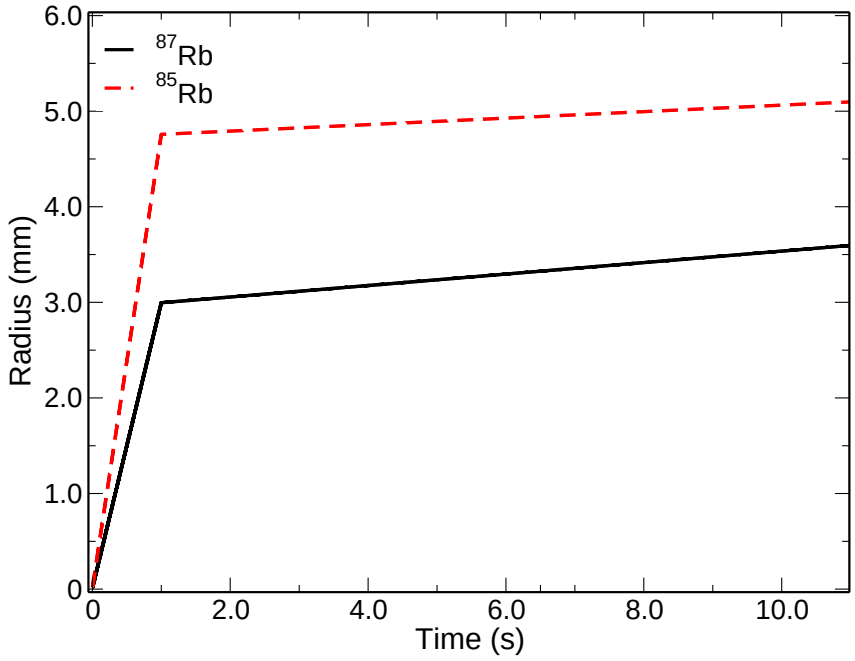

Figure 4.8: Effect of DKC in a mixture of ^{85}Rb/^{87}Rb with $N = 10^6$ atoms each component. The same DKC sequences have been applied for the mixture. The frequencies have been modified to account for the mass difference ($\omega_{85} = 2\pi \times 40$ Hz, $\omega_{87} = 2\pi \times 39.5376$ Hz), but the trap geometries are still spherical. DKC has been applied at $t^{start} = 1.0$ s during $t_{dur} = 0.016$ ms. ^{87}Rb is in black and ^{85}Rb in red.

low expansion rates, being different from each other by less than 2%, a value that can be extracted from fig. 3.21. The beneficial features come from the permanent miscibility observed during the dynamics of the mixture.

To test the weak equivalence principle, the expansion rates enter in the phase shift by means of the differential acceleration δa as

$$\delta a = \frac{k_B}{R}\left[\frac{T_{at,1}}{m_{at,1}} - \frac{T_{at,2}}{m_{at,2}}\right] \qquad , T_{at,1} = T_{at,2} \approx 70\text{pK} \; . \tag{4.11}$$

where k_B is the Boltzmann constant, $T_{at,1(2)}$ the effective atomic temperature of the 1(2) mixture component with atomic mass $m_{at,1(2)}$. R is the effective wavefront curvature which for this specific case is $R = 250$km [116].

The same estimations can be done for the ^{41}K/^{87}Rb mixture for future work. It is already expected to considerably reduce the systematic errors of the results obtained already for this ensemble.

The conclusion after considering a broad range of situations designed to take advantage of DKC is that with a proper choice of the DKC sequence, it is possible to optimize both, the size and the expansion velocity at the same time.

4.4.1 Optimization of expansion rates of the mixture components simultaneously

This chapter has been devoted to finding the optimization of the ratio between expansion rates of the mixture components. The interactions have been tuned to the repulsive regime and by modifying the DKC characteristics, finding the way to optimize the mixture preparation.

Two control knobs are chosen for the ratio of the expansion rates of the considered mixtures: the interaction strengths for the ^{87}Rb/^{85}Rb mixture and the lens duration in the ^{41}K/^{87}Rb mixture. The magnetic fields used for tuning the interactions in fig. 4.9 have been turned on during the first 10 ms of expansion.

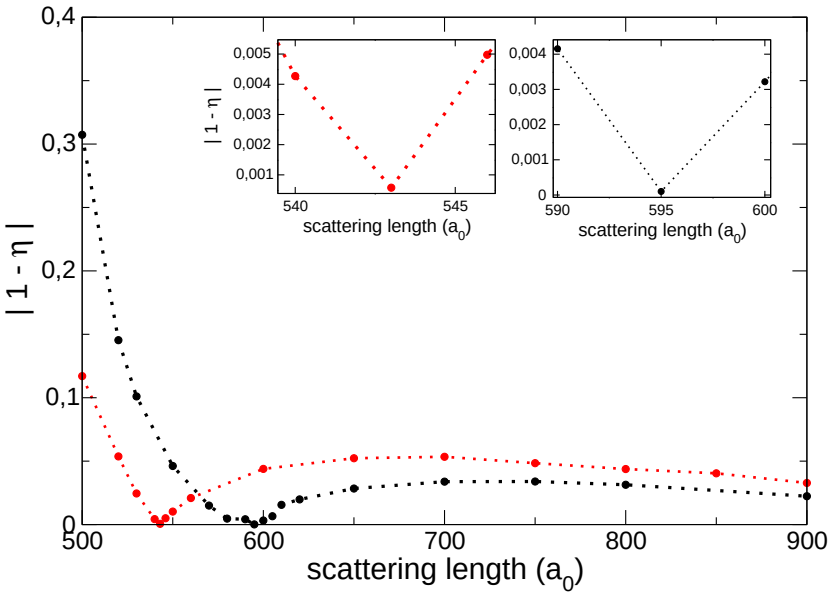

Figure 4.9: Matching of the expansion rates of two sets of ^{87}Rb/^{85}Rb mixtures with $N = 10^6$ (black dots) and $N = 5 \times 10^2$ (red dots) atoms each component. $\eta = v_{85}/v_{87}$ is the ratio between expansion rates. The self-interactions of ^{85}Rb have been made variable. The ensembles are subject first to a DKC by $t_{dur} = 0.302$ ms and starting at $t^{start} = 48.0$ ms, and second to changes of the scattering length between 500 and 900 a_0, for miscibility expected from $458a_0$. The optimal scattering length is around 595 a_0, found $\eta \sim 0.9992$. For the ensemble of $N = 10^6$ bosons and 545 a_0 for the weakly interacting samples with $N = 5 \times 10^2$ bosons, it is found $\eta \sim 1.001$. The insets are for a better visualization of the values. The colors correspond to the normal size curves.

The black curve in fig. 4.9, corresponds to an ensemble of $N = 10^6$ bosons, showing how the ratio between the expansion rates of the two samples can be brought very close to $\eta \approx 1.001$ for a scattering length $a_{85} \sim 595a_0$. This can be understood from the fact that at this value of scattering length the mixture is already miscible and stable and the scattering lengths of both components do not differ so much from each other, making the interaction energies faster compensated by the kinetic energies during the dynamics. Such compensation should be produced simultaneously in a similar way for both gases, in order to match the expansion velocities.

The matching of the expansion rates is important for the correction of the expected wavefront errors that influence the interferometer signal. The interferometer phase which is related to the differential accelerations (induced by the differential expansion rates based on the momentum distribution components of the BECs) is typically calculated ignoring the wavefront distortions and density profiles having non-trivial-geometry. Such distortions can lead to defects in the interference signal. In the cases studied, the weakly interacting systems ensure that such imperfections are not present and the theory to calculate the differential acceleration can be used. Aoms in such weakly interacting condensates have also smaller differential displacement and higher miscibility than

strongly interacting mixtures.

The other parameter allowing to control the expansion rates in each condensate and at the same time match the expansion rates of the components of the mixture is the duration of the kick, calculated for fixed values of scattering length. This effect is shown in a mixture of ^{41}K/^{87}Rb but works in the same way in the ^{87}Rb/^{85}Rb mixture.

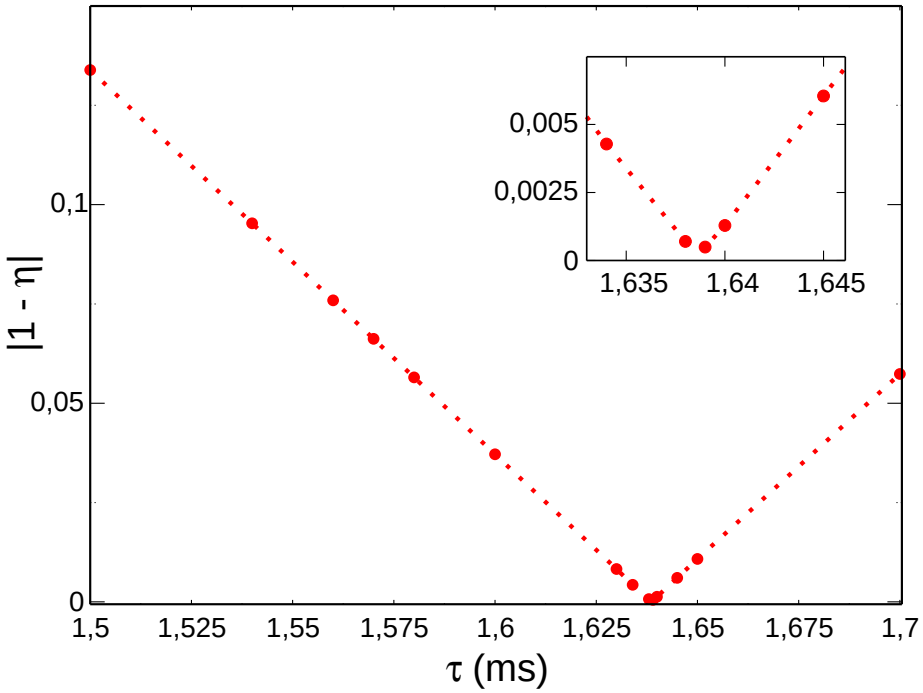

Figure 4.10: Ratio of the expansion rates of ^{87}Rb/^{41}K mixture by changing the duration of the DKC pulse. The mixture is prepared with 10^6 atoms in each component and the inter-species scattering length $a_{87-41} = 0a_0$ during first $t_{Feshbach} = 300$ ms of expansion. The DKC has been applied for a first time at $t^{start1} = 20.0$ ms with a fixed duration of $t_{dur1} = 9.0$ ms, the second time of DKC is $t^{start2} = 140.0$ ms with the duration used as the optimizing parameter, which has been found to be around $\tau = 1.64$ ms.

The long duration of the DKC in this mixture is justified by the shallow trap in ^{87}Rb. The atoms need to be trapped longer to feel the trapping effect. A discussion of this is developed in sect. 3.2.2.

The value τ used in the calculations ($\tau = 1.56$ ms) in sect. 3.2.2 is smaller than the optimal (1.64 ms). Due to the expansion features observed in this mixture, this mixture can be considered convenient to handle and capable to fulfill the specifications of an experimental implementation.

Each point in the curves of the last two fig. 4.9 and fig. 4.10 is obtained from the calculation of the ratio between the expansion velocities of the two components after a total evolution of 11 s. To understand more clearly the choice of the DKC steps for minimizing the expansion rates and simultaneously collimating the clouds, the numbers obtained in this regard are collected in Table 4.2.

The values related in Table 4.2 are extracted from fig. 3.15 and fig. 4.6. The radii of the component clouds at the moment of starting the DKC are too large, also the expansion rates from both components are not well matched. By comparing both the radii and the expansion rates in all combinations, it is evident that the case $t^{start} = 48.0$ ms is optimal.

Table 4.2: Summary of radii and expansion rates of components of a ^{87}Rb/^{85}Rb mixture containing $N = 10^6$ atoms. The data shown here are extracted from fig. 3.15 and fig. 4.6. Second column, a lens starting at $t^{start} = 48.0$ ms with a duration $t_{dur} = 0.302$ms. Third column $t^{start} = 100.0$ ms with a duration $t_{dur} = 0.156$ms. Fourth column $t^{start} = 200.0$ ms with a duration $t_{dur} = 0.078$ms. The radii (R) shown here, are measured at the moment of starting the DKC. The expansion rates are calculated when the clouds are linearly expanding.

Component	R(μm) / $v(\mu m/s)$ $t^{start} = 48.0$ ms	R(μm) / $v(\mu m/s)$ $t^{start} = 100.0$ ms	R(μm) / $v(\mu m/s)$ $t^{start} = 200.0$ ms
^{87}Rb	148.8/140.27	383.5/147.2	759.1/122.9
^{85}Rb	247.8/140.77	512.1/93.02	1014.6/54.4

Now that we found reliable configurations of DKC and strength interactions, we can take a good DKC configuration for each mixture where the expansion rates are low enough to be considered as good inputs for a high precision interferometry measurement and follows the dynamics of the atoms expanding during long time.

The expansion rates from the mixture ^{87}Rb/^{85}Rb are depicted in fig. 4.11. After DKC the expansion rates are approximately reduced by a half, reaching both velocities of 140 $\mu m/s$ that can be further reduced which requires more computational time, following the same protocols used so far.

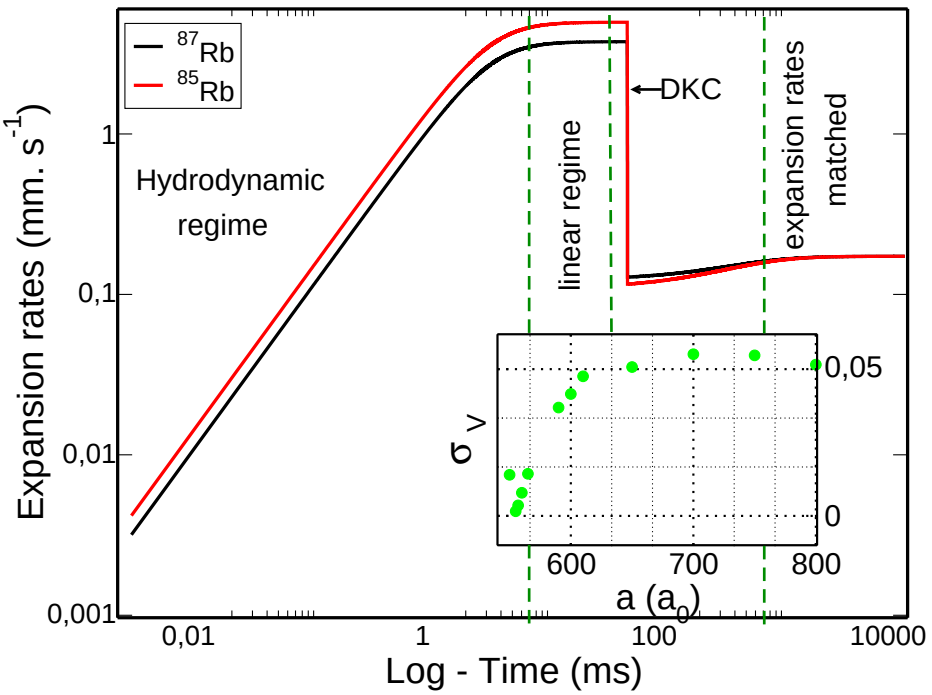

Figure 4.11: Log-log plot of expansion rates as a function of time for a ^{87}Rb/^{85}Rb mixture. The expansion rates are reduced to a level of 140 $\mu m \cdot s^{-1}$ leading them to match at the order of 10^{-3}. Same physical parameters used in previous calculations are used here, as related in Table 3.1. The inset shows the optimization of the expansion rates ratio by tuning the interactions.

Similarly, for the ^{87}Rb/^{41}K mixture the expansion velocities reach 100 $\mu m/s$ after DKC. They differ by a small fraction of 10^{-3} reducing the effect of the wavefront distortions. Consequently the use of a retro-reflection mirror with only $\lambda/30$ surface quality is required.

The special attention dedicated to control the expansion rates of the clouds comes

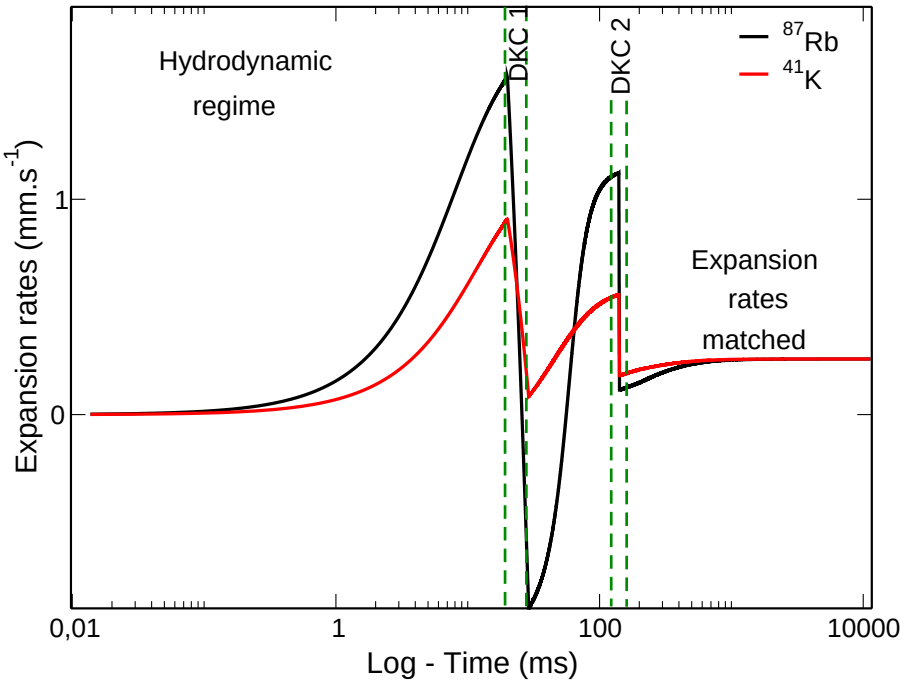

Figure 4.12: Expansion rates as a function of time for a ^{87}Rb/^{41}K mixture. These expansion rates are reduced to a level of 100 $\mu m \cdot s^{-1}$ matching them of the very low level of 10^{-3}. Two-pulse DKC is applied at $t^{start1} = 20.0\ ms$ with a duration of $t_{dur1} = 9\ ms$, and $t^{start2} = 140.0\ ms$ during $t_{dur1} = 1.56$ ms. The physical parameters used are indicated in Table 3.2.

from the fact that a retro reflection mirror defines the effective wave front curvature of the beam splitting light field. The initial collimation also plays a role, but standard techniques are considered as sufficient.

Having minimized the effect of the wavefront aberrations naturally present in the expansion of the atomic clouds, we focus on other experimental conditions limiting the accuracy of the Eötvös ratio.

4.5 Co-location of the samples

Since having the two components of the condensate of different masses, the gravity influences them in a different way, affecting the center of mass position. This, combined with other factors that will be discussed below, make the desired co-location of the samples a delicate issue to deal with.

When the condensates are not miscible or when their density profiles are far from the Gaussian shape, a relative phase is induced. This leads to a nonuniform growth during the interferometry affecting the visibility of the interference fringe. In this respect the choice of the atomic samples and the control of their interactions are crucial at a first stage. When the clouds are used in the interferometer an expansion with a careful choice of experimental parameters as can be seen in fig. 4.13 for a ^{87}Rb/^{85}Rb mixture where the overlap of the densities is enhanced is beneficial.

The estimation done in [116] for the initial positions of the centre of the clouds dictates that in order to maximize the resolution of the position of the atoms, the two components of the mixture should not be separated more than about $1nm$ in their center of mass. Using Feshbach resonance we are able to take an overlap of the densities in ^{87}Rb/^{85}Rb from as low as 40% as is the case for $a_{85} = 900a_0$, depicted in fig. 4.13, to a value of about

70% after applying the DKC twice, which may improve the overlap of the samples. This was already demonstrated as being a reliable technique for slowing down the expansion of the two samples simultaneously at extraordinarily low regimes of which we have already benefited.

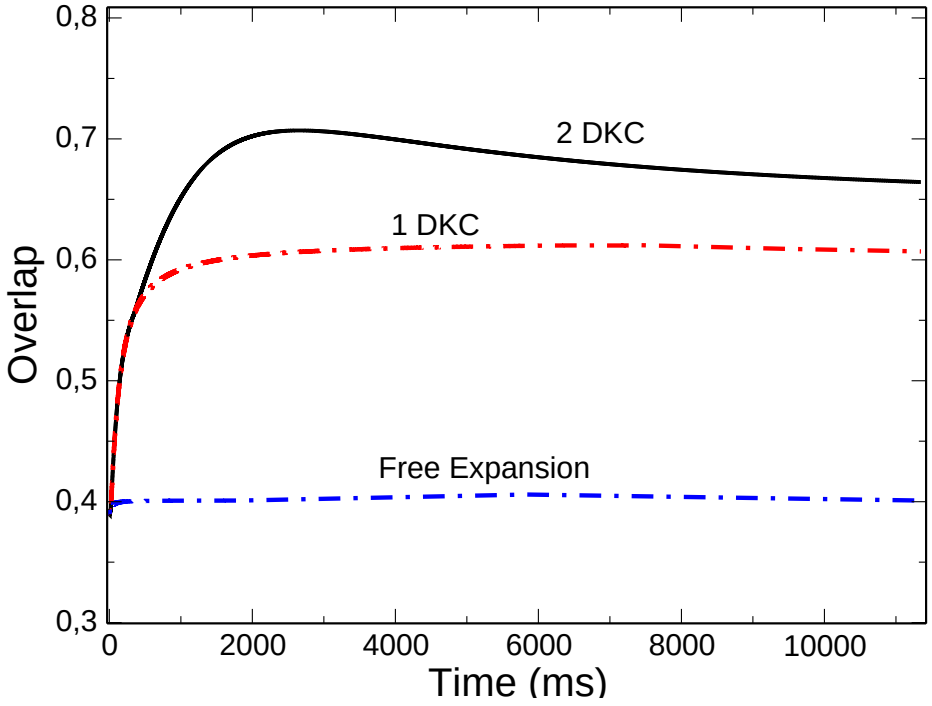

Figure 4.13: Enhancement of overlap between the two components by multi-lensing. A ^{87}Rb/^{85}Rb mixture of 10^6 atoms in each component is allowed to expand under three different conditions. First, it freely expands keeping the overlap constant as shown in the blue long-dashed line. Secondly, the DKC is applied once at $t_{start-1} = 20ms$ with a duration of $t_{dur-1} = 0.65ms$ shown in red dashed line, and last, the black curve shows the effect of DKC applied for a second time at $t_{start-2} = 350ms$ with a duration of $t_{dur-1} = 0.033ms$. $a_{85} = 900a_0$.

It has been noticed that the ground state solutions depend on several factors, one of them related to the relative separation of the two components, which is proportional to the gravitational acceleration and to the trap frequencies. For mixtures consisting of components with different masses, it is possible for the two condensates not to overlap at all.

4.6 Influence of magnetic and gravity gradients on phase separation

Systematic errors are induced in absolute g measurements due to diverse external factors that may compromise the miscibility of the component gases making the desired accuracy not achievable. These limitations are more critical in ground- than in space-based experiments, however, they can still induce important terms affecting the estimation of the phase shift in micro-gravity or space-based experiments as it is demonstrated with the results below for the mixtures of ^{87}Rb/^{85}Rb and ^{87}Rb/^{41}K.

4.6.1 Gravity gradients

The rise of gravity gradients in the measurements was already presented in sect. 4.2.1 and are of the order of $2.5 \times 10^{-6} s^{-2}$ in the satellite, inducing a differential acceleration $T_{zz}\Delta z$ due to the initial relative positions of the clouds Δz. This is numerically calculated by introducing the T_{zz} tensor component in the Hamiltonian of the system.

The effect has been studied for both ^{87}Rb/^{85}Rb and ^{87}Rb/^{41}K mixtures. We will first discuss the results for ^{87}Rb/^{85}Rb mixture. Due to the topology of the wave functions of the ground states already known from this work, there are two interesting regimes to consider, the theoretically predicted deeply miscible, which is $a_{85} = 900a_0$ and the threshold of miscibility, which is $a_{85} = 460a_0$.

^{87}Rb/^{85}Rb with $a_{85} = 900a_0$.

We have covered a wide range of values of gravitational acceleration to detect any shift in position of the center of mass of the atomic clouds, starting from a very small value $g = 10^{-6}m/s^2$, meaningful in micro-gravity to $g = 10^{-1}m/s^2$, which is already a gravity environment. In fig. 4.14 the most easily perceptible shift compared to the absence of gravity is shown.

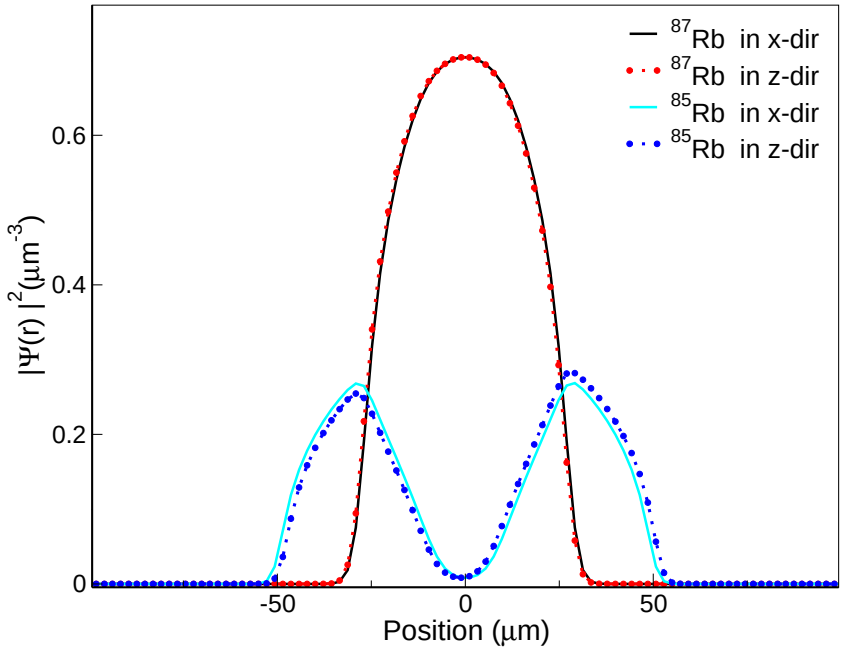

Figure 4.14: Gravity gradient effects on a ^{87}Rb/^{85}Rb mixture. The mixture consists of $N = 10^6$ atoms in each component and $a_{85} = 900a_0$, the trap frequencies are taken from Table 3.1. The solid lines display the density profiles in absence of gravity, being the black curve for ^{87}Rb, and cyan is for ^{85}Rb. When a gravity gradient is applied by taking $g = 10^{-1}m/s^2$, the density profiles of ^{87}Rb (black dots) and ^{85}Rb (red dots) show a very small relative position $\Delta z \sim 1.5\mu m$.

When sweeping the values of g it was found that extremely small values $g < 10^{-2}$ do not entail any noticeable change until $g = 1 \times 10^{-2}m/s^2$ value and the two centers are separated by $\Delta z \approx 180nm$ which is very close to the theoretically expected value of $158 - 162nm$ for the two species, not shown here because is not easily perceptible, instead the density profiles influenced by a gravity gradient given by $g = 10^{-1}m/s^2$, with $g = 0$ are compared.

The mixture for $a_{85} = 900a_0$ is showing a shell structure instead of two perfectly overlapped clouds. We have found that it is quite stable against small perturbations such as the values of gravity gradients applied here. To observe a symmetry breaking large values of g would be required.

^{87}Rb/^{85}Rb with $a_{85} = 460a_0$.

The idea of applying a gravity gradient to this mixture in the threshold of miscibility is to see if we can induce in this way a symmetry breaking. In this case, like the foregoing sect. 4.6.1, we have made a broad sweep of values of g, from $g = 10^{-6}m/s^2$ to $g = 1m/s^2$. The ensemble consists of $N = 10^4$ atoms each species. In this system, again we observe that no noticeable changes in the spatial densities for a wide range of g values occur. By the resutsobtained in fig. 3.5, his effect is expected to be more dramatic for an ensemble with a larger number of atoms .

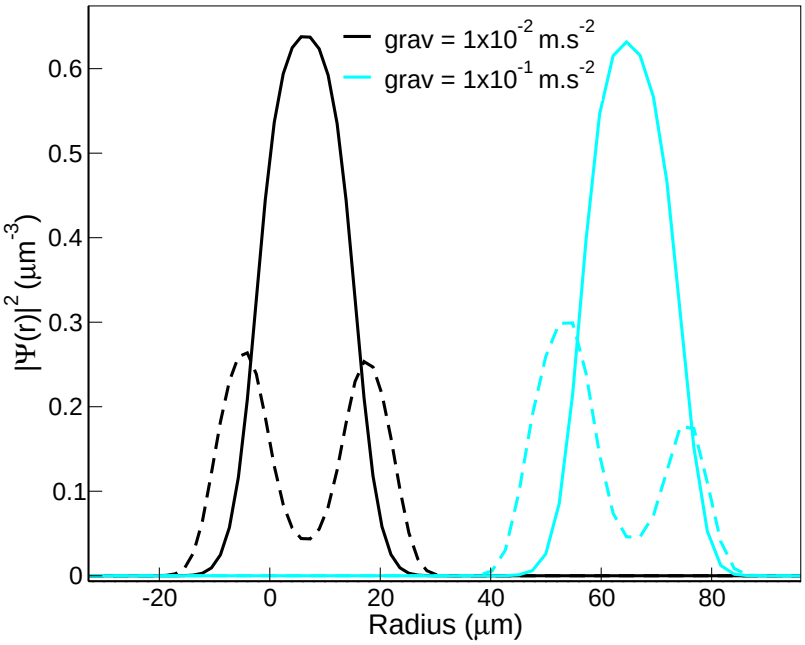

Figure 4.15: Gravity gradient effects on a ^{87}Rb/^{85}Rb mixture. The mixture consists of $N = 10^4$ atoms in each component and $a_{85} = 460a_0$, the trap frequencies are related in Table 3.1. The solid lines display the density profiles of ^{87}Rb,and dashed lines show ^{85}Rb. Black curves show the effect on the densities by applying $g = 10^{-2}m/s^2$ ($\Delta z \sim 150nm$), when increasing g to $g = 10^{-1}m/s^2$, the density profiles show the non-symmetric structure depicted by cyan curves with $\Delta z \sim 3.2\mu m$. The shift of positions is evident in both cases.

The finite relative position of the samples observed in both cases in fig. 4.17 was expected due to the fact that the mixture is in an unstable regime which can be easily affected by external perturbations. The density profile of ^{85}Rb is showing a strong symmetry breaking.

We continue increasing the values of g to complete the tendency of broken symmetry evidenced in fig. 4.17. Now the values are taken in a 1 g gravity environment.

fig. 4.16 shows a clear phase separation induced by large gravity gradients, which is another signature of the unsuitability of such condensate ensemble in ground-based measurements.

^{87}Rb/^{41}K.

This ensemble has been previously shown in sect. 3.2.2 as being highly miscible and stable in the presence of the Feshbach field of 80 G, where the two clouds with spherical symmetry merge perfectly, therefore it is expected that if there is a symmetry breaking, this should be manifested by the separation of the condensates, not exhibiting any

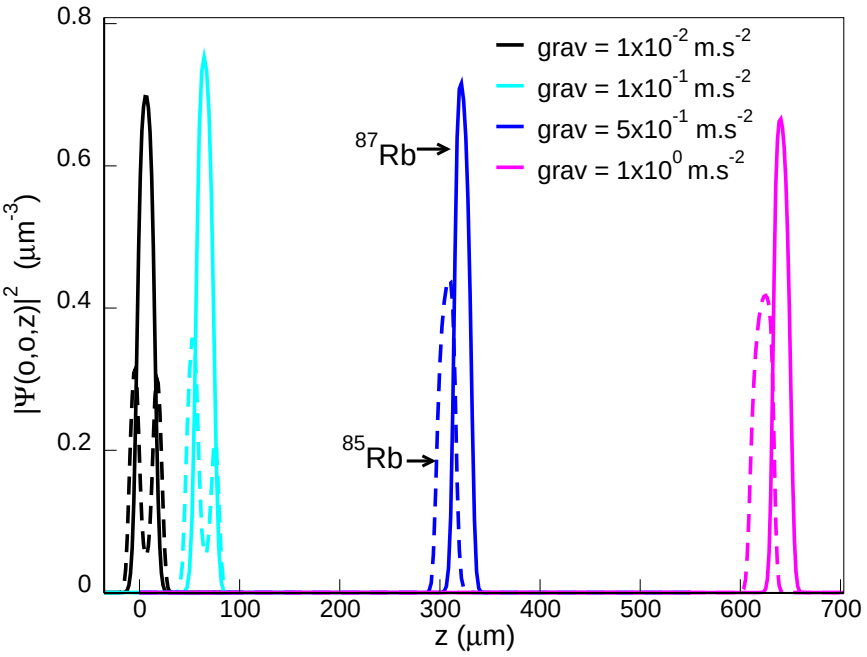

Figure 4.16: Phase separation induced by large gravity gradients in a ^{87}Rb/^{85}Rb mixture. A mixture of $N = 10^4$ atoms each component and $a_{85} = 460a_0$, in a trap of frequencies given in Table 3.1. The solid lines show ^{87}Rb, and dashed lines ^{85}Rb density profiles. Black and cyan curves are the last case fig. 4.17, shown here just for comparison. Tunning gravity to $g = 10^{-2}m/s^2$ ($\Delta z \sim 150nm$), the case of $g = 5 \times 10^{-1}m/s^2$ is depicted in blue curves, found a $\Delta z \sim 4\mu m$, and lastly, $g = 1m/s^2$ (magenta), found a $\Delta z \sim 17\mu m$.

non-trivial shape.

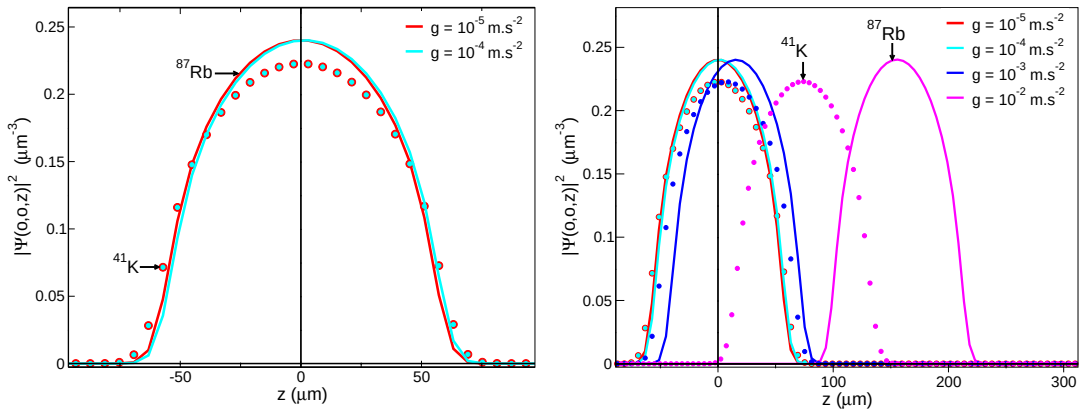

Figure 4.17: Gravity gradient effects on a ^{87}Rb/^{41}K mixture. Density profiles of ^{87}Rb are on solid lines, and of ^{41}K are the dots. On left figure the cases of having $g = 10^{-5}m/s^2$ (red) and $g = 10^{-4}m/s^2$ (cyan) are depicted , there is already an observable shift of the relative positions Δz of few nm. On right side, are shown the cases of left figure as a reference point, additionally, the densities for using $g = 10^{-3}m/s^2$ (blue) and $g = 10^{-2}m/s^2$ (magenta) are plotted, sufficient for symmetry breaking observations.

For ^{87}Rb/^{41}K ensemble a slight displacement has been observed, this causes the condensates separate, this is despite the stability, due to the fact that their masses are very different from each other. The effect of gravity becomes important for small values

of g, since for $g = 10^{-4} m/s^2$ a shift in the center of mass of components by $\Delta z \sim 5nm$ was obtained.

4.6.2 Magnetic gradients

Inhomogeneities in the bias fields, as the one used to tune the interactions to force the ensembles to merge give rise to a residual phase shift contributing to the measured differential accelerations. Phase separation may arise with the addition of weak magnetic gradients that are correlated to the fact of having different coefficients for the quadratic Zeeman shift in the two isotopes.

The Hamiltonian of the system is modified by adding such inhomogeneities as shown in eq. (4.12)

$$H'_M(x) = \alpha x \quad , \alpha = m\omega_x^2 \delta \ . \tag{4.12}$$

The magnetic gradient has been considered in one direction, but it is straightforward to extend for more dimensions. Here α is the bias magnetic gradient written in terms of an offset δ on which we make a broad sweep to observe when the bias magnetic gradient has a dramatic effect on the mixtures inducing a separation of the clouds. In all cases studied below, the magnetic gradient has been shifting the ^{87}Rb atoms.

^{87}Rb/^{85}Rb.

In order to study stability and phase separation induced by magnetic gradients, the two ultimate cases, $a_{85} = 900a_0$ and $a_{85} = 460a_0$ are analyzed.

The trapping frequencies here are once again: $\omega_{85} = 2\pi \times 40$ Hz, $\omega_{87} = 2\pi \times 39.5376$ Hz, the scattering length $a_{85} = 900a_0$. A symmetry breaking has been observed as an effect of the large values of magnetic gradients, transforming from a shell structure to a side-to-side cloud, as it is shown below in fig. 4.18.

In fig. 4.18 three cases of magnetic offset are depicted where the separation of the center of mass positions of the two clouds a $\delta = 100n$m, $\delta = 1\mu$m and $\delta = 7\mu$m.

To facilitate the observation of a possible separation of the components, the calculation have been done in the threshold of miscibility, $a_{85} = 460a_0$ and the results are shown in fig. 4.19

In all cases sketched in fig. 4.18 and fig. 4.19 the direct correlation between the offset applied and the shift in the center of mass is observed.

A similar behavior as in the previous case fig. 4.18 is observed here in fig. 4.19.The rise of non-trivial structures of the spatial densities is clear.

^{87}Rb/^{41}K.

To evaluate the effect of magnetic gradient in ^{87}Rb/^{41}K mixtures, a wide range of values of the offset has been sweep, as shown below in fig. 4.20.

When an offset of $\delta = 5.0\ nm$ was applied, it did not produced a significant change in the relative position of the condensates, since it was measured to be of the order of Å. For $\delta = 0.5\ \mu m$ a shift can be seen since the black and turquoise curves are not exactly superimposed, giving a shift of $\sim 0.3\ \mu m$, and last, in the cases for $\delta = 5\ \mu m$ and $\delta = 50\ \mu m$ the direct correlation between the offset and the shift caused is evident. The ^{87}Rb/^{41}K ensemble is manifestly susceptible to separation induced by the environment.

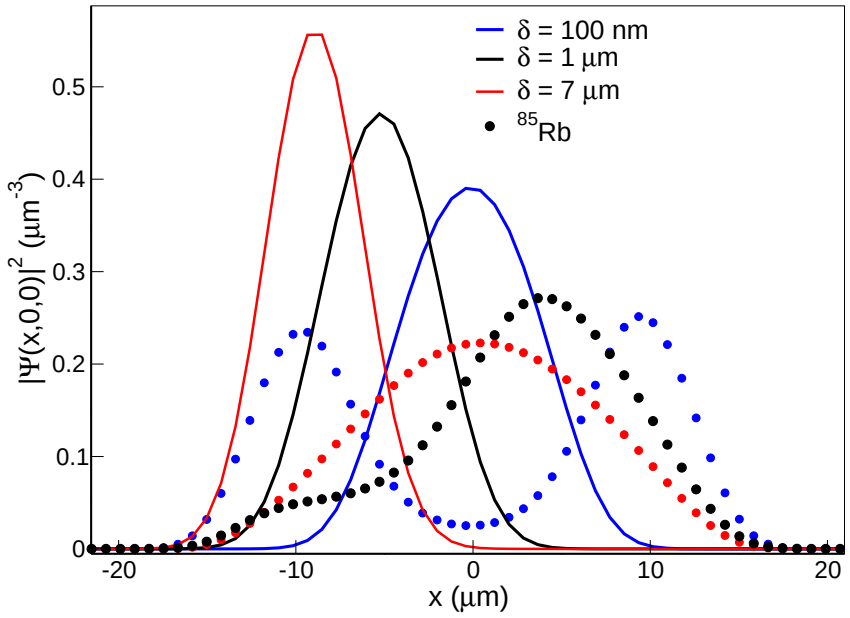

Figure 4.18: Effect of a bias magnetic gradient on a ^{87}Rb/^{85}Rb mixture in the more miscible regime possible corresponding to $a_{85} = 900a_0$. A mixture of 10^6 atoms in each component in harmonic traps of frequencies $\omega_{85} = 2\pi \times 40$ Hz, $\omega_{87} = 2\pi \times 39.5376$ Hz is subject to a magnetic gradient given by eq. (4.12). The presence of the offset δ induces a symmetry breaking largely separating the center of mass position of the components. Solid lines are for ^{87}Rb and dots are for ^{85}Rb. Black color lines show the effect of an offset $\delta = 1\mu$m., blue lines show the effect of an offset $\delta = 100n$m and red lines are for an offset $\delta = 7\mu$m.

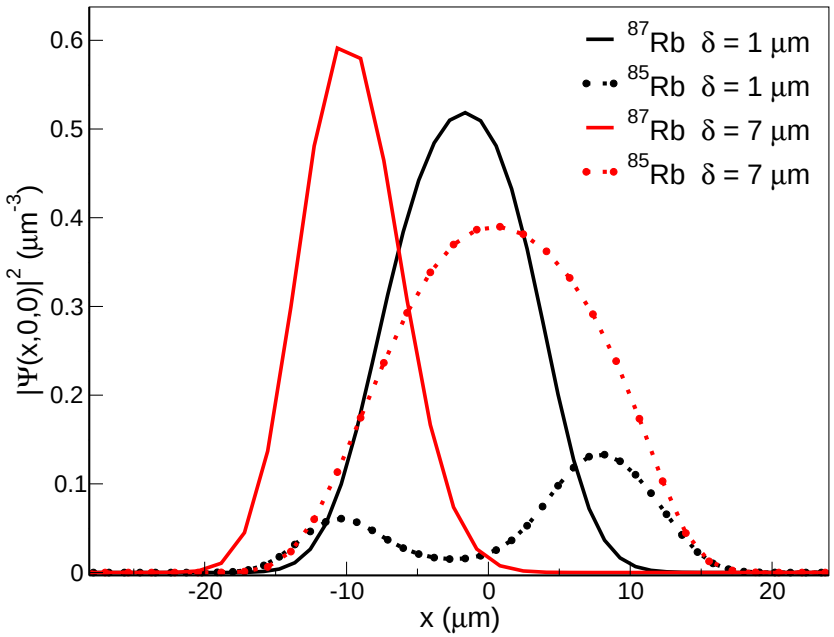

Figure 4.19: Effect of a bias magnetic gradient on a ^{87}Rb/^{85}Rb mixture put close to the threshold of phase separation, but still with the physical parameters defining the miscible regime, already expected for $a_{85} = 460a_0$. A mixture of 5×10^3 atoms in each component in a harmonic traps of frequencies $\omega_{85} = 2\pi \times 40$ Hz, $\omega_{87} = 2\pi \times 39.5376$ Hz is subject to a magnetic gradient given by eq. (4.12). The symmetry breaking induced by the magnetic gradient is stronger than for the previous case of $a_{85} = 900a_0$. The center of mass position of the components are clearly distinct. Solid lines are for ^{87}Rb and dots are for ^{85}Rb. Black color lines show the effect of an offset $\delta = 1\mu$m, blue lines show the effect of an offset $\delta = 100n$m and red lines are for an offset $\delta = 7\mu$m.

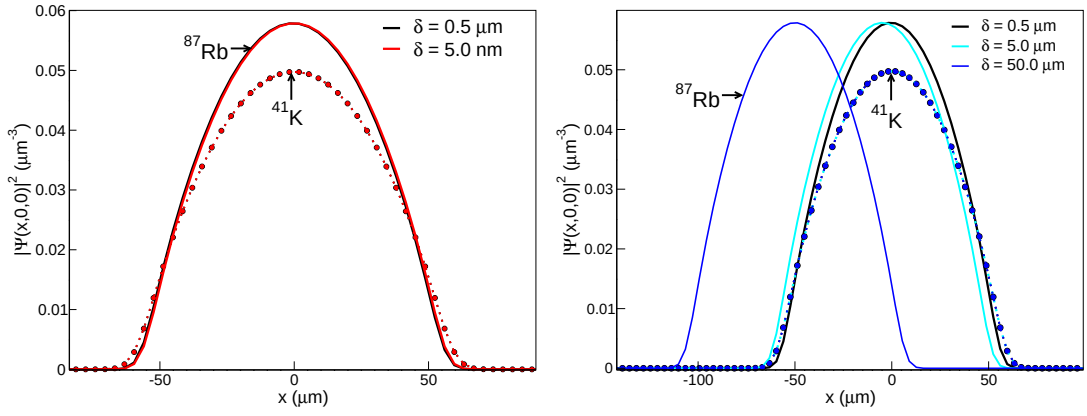

Figure 4.20: A bias magnetic gradient is introduced in the ^{87}Rb/^{41}K mixture. Figure on the left side contains the density profiles of ^{87}Rb in solid lines and ^{41}K in dashed lines, for two different values of the offset, $\delta = 5.0nm$ (black) and in red is $\delta = 0.5\ \mu m$. On the right figure are depicted the shifts in the densities for three offsets, $\delta = 0.5\ \mu m$ (black), $\delta = 5.0\ \mu m$ (cyan) and $\delta = 5.0\ nm$ (blue curves).

4.7 Conclusion

In this chapter, some physical factors that may influence the performance of the measurements in atom interferometry to test the weak equivalence principle have been considered. Such factors are: differential position and the expansion rates of the mixture components, magnetic and gravity gradients.

The main motivation of this study is the preparation of a suitable source for precision measurements based on atom interferometry which was proposed in STE-QUEST project which was addressed for an exclusive mixture of ^{87}Rb/^{85}Rb which allows for a common noise rejection.

The requested co-location of the samples for a differential position not greater than $1nm$ can be achieved with a highly miscible mixture, this is not perfectly reached for the ^{87}Rb/^{85}Rb mixture. To circumvent this, other ensembles have been investigated and demonstrated their suitability, these are: ^{87}Rb/^{41}K, ^{87}Rb/^{168}Yb and ^{87}Rb/^{170}Yb.

The overlap of the density wave packets of the two components has been studied as a function of important physical variables, like the scattering length and duration of delta-kick cooling.

The range of magnetic and gravity gradients present in a microgravity environment is not inducing a separation of the components.

It has been presented an efficient sequence of delta kick cooling and tuning of the interactions to fulfill the conditions above discussed.

CHAPTER 5

Conclusion and outlook

This thesis has provided a specific investigation for preparing atomic mixtures for high precision atom interferometry extended for over unprecendeted durations. These sources consisting of mixtures of Bose-Einstein condensates are guaranteed to be stable against interaction-induced collapse, compact and able to reduce the different systematic effects as the one for example present in laser cooled samples and hinder to achieve high precision measurements.

Engineering a suitable source for precision-atom-interferometry for a test of the Weak Equivalence principle at a high accuracy of 10^{-15} on a satellite goes well beyond the state of the art in atom optics. We have designed some strategies for largely preventing some of the most important effects related to wavefront errors.

The differential mean positions and velocities between the component gases launched in the interferometer may lead to wavefront errors, mean field effects, magnetic and the Earth gravity gradients. In order to limit the differential acceleration to a precision of $10^{-15} m/s^2$, the differential displacement between the atomic ensembles must be kept below 1 nm if one cannot apply gravity gradients compensation methods, as proposed in [187] for example.

Indeed, the minimum relative position of the two atomic gases forming the mixture, which strongly depends on the species chosen. To this end, we have mostly dealt with two systems: ^{87}Rb/^{85}Rb and ^{87}Rb/^{41}K. For these cases we studied the interactions which can be modified with the help of Feshbach resonances such that the two species to become miscible. We paid attention that further complications due to the presence of high magnetic fields were avoided. Other aspects had to be considered, including the geometry and frequencies of the traps, and the density profiles of the ground state of the ensembles. Furthermore, the miscibility of components predicted by theory is limited to uniform potentials and has been contrasted with realistic traps.

For minimizing most of the systematic errors limiting the performance of the system, a sequence of delta-kick collimation and tuning of the interactions was found ensuring very low expansion rates. We anticipate that the use of tunable interactions and delta-kick collimation could emerge as a standard technique for precision measurements in atom interferometry.

The effects of magnetic and gravity gradients have been analyzed as leading error terms that may contribute in error terms limiting the performance of the measurements.

The physical systems considered here are also suitable for performing ground-based

measurements. Other ensembles fitting in the application of the techniques are: ^{87}Rb/^{39}K and ^{87}Rb/^{170}Yb.

Besides the mixtures studied, we have considered single-species components prepared in realistic traps configurations, such as, optical dipole, chip-based and TOP traps and concluded that models assuming harmonic potentials are too simplistic. Important effects on the expansion and on the motion of the center of mass of BECs subject to DKC by these potentials were noticed. Gross-Pitaevskii equations were solved to account for the realistic dynamics.

In case of realistic crossed dipole trap, the actual shape is imprinted onto the wave functions by the delta kick, particularly due to an imperfect harmonicity, wings are observed in the spatial profile of the BEC after its time-evolution.

When using a magnetic field created by an atom chip for trapping of the BEC and for the delta-kick, it has been noticed, that DKC is also imperfect as tails arising at both sides of the cloud in contrast to the case where an ideal harmonic potential is used.

Among the several trapping configurations, there has been studied an anisotropic harmonic trap of different strengths in the three directions. The latter makes an efficient simultaneous collimation in all directions a difficult task. For this case, studies recommend a multi-pulse DKC sequence as solution since the less confined direction needs a pulse of longer duration to be collimated producing a focal-point-like effect in the other directions which will require a further collimation achieved with a second pulse.

In addition to the different trapping conditions of a BEC of ^{87}Rb, within the study of single-component BECs of ^{41}K, ^{85}Rb and ^{39}K, the manipulation of the type and strength of interactions via Feshbach resonances by deriving a simple energy equilibrium condition to guarantee the stability against collapse during long expansion times has been crucial in this work.

In this thesis, an extension of the scaling approach used to describe the time-evolution of the size of a condensate in the miscible regime has been performed for binary mixture condensates giving an excellent agreement when contrasted with the solutions of the coupled time-dependent Gross-Pitaevskii equations.

In the production of compact and slowly expanding condensates mixtures, it has been observed, that in the case of the ^{87}Rb/^{41}K mixture the application of a multiple-pulse DKC sequence is required due to the mass difference between components.

It has been found that the ^{87}Rb/^{170}Yb mixture stays miscible during long expansion times without the need for large bias magnetic fields. This mixture is an ideal source for atom interferometry as it allows to perform experiments in a field-free environment and to reach low expansion rates.

The work presented in this thesis depicts the possibilities to make experiments using mixtures of Bose Einstein condensates as sources which allows to predict their behavior under different conditions.

Improving the efficiency of the DKC protocols in realistic trapping potentials

The delta-kick collimation procedures applied to a BEC subject to the different realistic traps considered in this work did not show the same response as for the well-known harmonic traps. To these discrepancies, several factors may contribute. In order to

improve the understanding and therefore to enhance the efficiency of the DKC some additional computations were performed and strategies developed.

Our studies showed that the efficiency of the delta-kick collimation protocols in realistic trap configurations can be improved by lowering the atomic density before releasing the gas, this can be done by modulating the strength of the potential to re-trap the atoms to be a fraction of that used to produce the BEC. An efficient collimation will be produced with shorter pulses preventing the BEC goes into a focal-point in some direction(s) while producing almost a null effect on the other(s) direction(s).

The expansion can also comprise two different stages, instead of releasing suddenly, it is possible to first open the trap adiabatically during the first few milliseconds to also produce a more compact cloud, followed by a more controlled free expansion to apply then a short-duration DKC pulse as it is being experimentally implemented by the Quantus experiment. The numerical study helps to make a choice of timings and durations of each stage to efficiently collimate the BEC.

The long-duration of the kick used to collimate a cloud in the presence of a spatially-dependent force causes harmonic-like oscillations of the center of mass of the BEC as it was the studied case of the ^{87}Rb BEC in a TOP trap. In addition to the description made in this work which consisted in solving the time-dependent Gross Pittaevskii equation for the wave function, a function $\phi_0(x)$ which is solution of the time-independent problem corresponding to the chemical potential μ, is used to be time-evolved similar to a Path integral formulation

$$\phi(x,t) = \phi_0(x)e^{-i\mu t}e^{i[\dot{q}x - S(q)]} \tag{5.1}$$

with

$$S(q) = \int_0^t dt' \left[\dot{q}^2(t') - q^2(t')\right] \tag{5.2}$$

Both solutions can be compared.

When the condensates are created and delta-kicked in non-harmonic traps, the wave function will be asymmetric and its center does not coincide with the trap minimum. Interactions may enhance this effect with respect to the origin, such an asymmetry could be enhanced. This effect can impede the collimation and was therefore studied in this PhD. In this context, protocols were identified suppressing this effect. With the help of simulations one can predict this displacement and shift the trap minimum employed for the delta-kick.

Selecting the condensates mixtures

With respect to the choice of condensates mixtures, it tuned out to be useful to make preliminary tests of the evolution of competing interaction energy terms at the first milliseconds of expansion for both components by solving the Gross-Pitaevskii equations to anticipate the feasibility of a particular mixture to be used as a source in experiments requesting miscibility during long times of expansion.

This is important because the case of the mixture ^{39}K/^{87}Rb prepared to be stable and miscible when confined, but showed vastly different expansion behavior partly explained by the different interaction energy variation as illustrated in fig. 5.1.

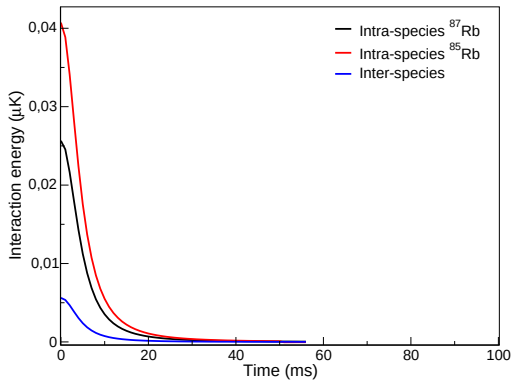

(a) Mixture ^{85}Rb/^{87}Rb, $a_{85/87} = 213a_0$, the scattering length of ^{85}Rb is tuned to $a_{85} = 900a_0$.

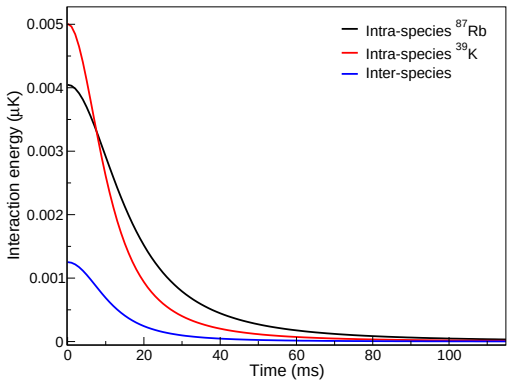

(b) Mixture ^{39}K/^{87}Rb, $a_{39/87} = 34a_0$, the scattering length of ^{39}K is tuned to $a_{39} = 100a_0$.

Figure 5.1: Variation of the interaction energies of the condensates mixtures. In (a) ^{87}Rb occupies the central region, both intra-species interaction energies decay at the same rate, the energy between the atoms of ^{85}Rb is larger than the other energies during the expansion allowing the relation between the energies system to remain unchanged. The initial relation between energies in (b) change during expansion, the system is miscible at $t = 0$ with higher peak density of the ^{87}Rb cloud.

Effect of large scattering length a

The work can be extended to encompass systems more strongly interacting, by including additional terms for accounting the very large interactions. The description then goes beyond mean field theory. The mean field Gross Pitaevskii equation is valid whenever the inter-particle spacing is larger than the scattering length, this is $n|a|^3 \ll 1$

This generalization consists in including the well-known non-perturbative Lee Huang Yuan (LHY) correction [188, 189] which modifies the ground state energy of a BEC of a volume V and mass m

$$E_{GS} = \frac{2\pi\hbar^2 V n^2}{M} a \left[1 + \frac{128}{15}\sqrt{\frac{na^3}{\pi}} + \dots\right] \tag{5.3}$$

where n is the density. This may lead to improved results.

Three-body interactions

Although three-body interactions have negligible contributions to the loss of atoms in the condensate mixture, they can have small contributions in the wave functions of the ensembles that can be non-negligible for high precision measurements.

In this thesis, it has been observed that the evolution of the wave functions is trap-shape-dependent, this is even more dramatic for strong confinements, The dynamics of BECs with high densities or strong confinement needs a better description of the inter-atomic interactions.

The inclusion of three-body recombination losses terms would be important to analyze the impact of losses in the condensate mixtures.

The way to introduce this effect would be by including the imaginary three-body loss

term in the Gross-Pitaevskii [190]

$$i\hbar\frac{\partial}{\partial t}\Psi = \left[-\frac{\hbar^2}{2m}\nabla^2 + V_{trap} + g|\Psi|^2 - i\frac{\hbar}{2}K_3|\Psi|^4\right]\Psi, \tag{5.4}$$

with Ψ a real function, and where V_{trap} is the trapping potential, g the effective interaction between atoms, and K_3 is the three-body loss coefficient which has been theoretically deduced or experimentally measured for different atomic species. For the non-condensed atoms in the cloud, this coefficient is different by a statistical factor of $\sqrt{3}$ [190]. To inlcude the effect of thermal atoms, one should also takes into account that the density of the thermal atoms is smaller than that of condensed atoms by about one order of magnitude, will therefore show different decay characteristics [128].

Bibliography

[1] Anderson, M. H., J. R. Ensher, M. R. Matthews, C. E. Wieman, and E. A. Cornell: 'Observation of Bose-Einstein Condensation in a Dilute Atomic Vapor'. *Science* (1995), vol. 269(5221): pp. 198–201 (cit. on pp. 1, 12, 30).

[2] Davis, K. B., M. -O. Mewes, M. R. Andrews, N. J. van Druten, D. S. Durfee, D. M. Kurn, and W. Ketterle: 'Bose-Einstein Condensation in a Gas of Sodium Atoms'. *Phys. Rev. Lett.* (22 Nov. 1995), vol. 75: pp. 3969–3973 (cit. on p. 1).

[3] Bloch, Immanuel, Jean Dalibard, and Wilhelm Zwerger: 'Many-body physics with ultracold gases'. *Rev. Mod. Phys. 80, 885* (2008), vol. (cit. on p. 1).

[4] Byrnes, Tim, Kai Wen, and Yoshihisa Yamamoto: 'Macroscopic quantum computation using Bose-Einstein condensates'. *Phys. Rev. A 85, 040306(R)* (2012), vol. (cit. on p. 1).

[5] Dickerson, S. M., J. M. Hogan, A. Sugarbaker, D. M. S. Johnson, and M. A. Kasevich: 'Multiaxis Inertial Sensing with Long-Time Point Source Atom Interferometry'. *Phys. Rev. Lett. 111, 083001* (2013), vol. (cit. on pp. 1, 3, 66).

[6] Kovachy, Tim, Jason M. Hogan, Alex Sugarbaker, Susannah M. Dickerson, Christine A. Donnelly, Chris Overstreet, and Mark A. Kasevich: 'Matter Wave Lensing to Picokelvin Temperatures'. *Phys. Rev. Lett.* (14 Apr. 2015), vol. 114: p. 143004 (cit. on pp. 1, 3, 18, 31, 66).

[7] Müntinga, H. et al.: 'Interferometry with Bose-Einstein Condensates in Microgravity'. *Phys. Rev. Lett.* (9 Feb. 2013), vol. 110: p. 093602 (cit. on pp. 1, 3, 18).

[8] Broglie, Louis de: 'The reinterpretation of wave mechanics'. English. *Foundations of Physics* (1970), vol. 1(1): pp. 5–15 (cit. on p. 1).

[9] Henkel, Carsten, Jean-Yves Courtois, and Alain Aspect: *Atomic diffraction by a thin phase grating*. 2010 (cit. on p. 1).

[10] Andrews, M. R., C. G. Townsend, H.-J. Miesner, D. S. Durfee, D. M. Kurn, and W. Ketterle: 'Observation of Interference Between Two Bose Condensates'. *Science* (1997), vol. 275(5300): pp. 637–641 (cit. on p. 1).

[11] O., Carnal and Mlynek J.: 'Young's double-slit experiment with atoms: A simple atom interferometer'. *Phys. Rev. Lett. 66, 2689* (1991), vol. (cit. on pp. 1, 66).

[12] Einstein, A.: 'Quantentheorie des einatomigen idealen gases'. *Sitzungsberichte der Preussischen Akademie der Wissenschaften XXII, 261*. 1924 (cit. on p. 1).

[13] C., Bradley C., Sackett C. A., Tollet J. J., and Hulet R.: 'Bose-Einstein Condensation of Lithium: Observation of Limited Condensate Number'. *Phys. Rev. Lett. 78, 985* (1997), vol.

[14] Fermi, E., E. Amaldi, O. D'Agostino, F. Rasetti, and E. Segre: 'Artificial Radioactivity Produced by Neutron Bombardment'. *Proceedings of the Royal Society of London A: Mathematical, Physical and Engineering Sciences* (1934), vol. 146(857): pp. 483–500 (cit. on p. 2).

[15] Amaldi, E., O. D'Agostino, E. Fermi, B. Pontecorvo, F. Rasetti, and E. Segre: 'Artificial Radioactivity Produced by Neutron Bombardment. II'. *Proceedings of the Royal Society of London A: Mathematical, Physical and Engineering Sciences* (1935), vol. 149(868): pp. 522–558 (cit. on p. 2).

[16] Amaldi, E. and E. Fermi: 'On the Absorption and the Diffusion of Slow Neutrons'. *Phys. Rev.* (10 Nov. 1936), vol. 50: pp. 899–928 (cit. on p. 2).

[17] Cornell, E.A. and C.E. Wieman: 'Nobel Lecture: Bose-Einstein condensation in a dilute gas, the first 70 years and some recent experiments'. *Rev. Mod. Phys. 74, 875* (2002), vol. (cit. on pp. 1, 3).

[18] Ketterle, W.: 'Nobel lecture: When atoms behave as waves: Bose-Einstein condensation and the atom laser'. *Rev. Mod. Phys. 74, 1131* (2002), vol. (cit. on pp. 1, 3).

[19] Esry, B. D., Chris H. Greene, James P. Burke Jr., and John L. Bohn: 'Hartree-Fock Theory for Double Condensates'. *Phys. Rev. Lett.* (19 May 1997), vol. 78: pp. 3594–3597 (cit. on p. 45).

[20] Myatt, C. J., E. A. Burt, R. W. Ghrist, E. A. Cornell, and C. E. Wieman: 'Production of Two Overlapping Bose-Einstein Condensates by Sympathetic Cooling'. *Phys. Rev. Lett.* (4 Jan. 1997), vol. 78: pp. 586–589 (cit. on pp. 2, 3, 45).

[21] Hall, D. S., M. R. Matthews, J. R. Ensher, C. E. Wieman, and E. A. Cornell: 'Dynamics of Component Separation in a Binary Mixture of Bose-Einstein Condensates'. *Phys. Rev. Lett.* (8 Aug. 1998), vol. 81: pp. 1539–1542 (cit. on pp. 2, 3).

[22] Matthews, M. R., B. P. Anderson, P. C. Haljan, D. S. Hall, C. E. Wieman, and E. A. Cornell: 'Vortices in a Bose-Einstein Condensate'. *Phys. Rev. Lett.* (Sept. 1999), vol. 83(13): pp. 2498–2501 (cit. on p. 2).

[23] Miesner, H.-J., D. M. Stamper-Kurn, J. Stenger, S. Inouye, A. P. Chikkatur, and W. Ketterle: 'Observation of Metastable States in Spinor Bose-Einstein Condensates'. *Phys. Rev. Lett.* (11 Mar. 1999), vol. 82: pp. 2228–2231 (cit. on p. 2).

[24] Stamper-Kurn, D. M., H.-J. Miesner, A. P. Chikkatur, S. Inouye, J. Stenger, and W. Ketterle: 'Quantum Tunneling across Spin Domains in a Bose-Einstein Condensate'. *Phys. Rev. Lett.* (4 July 1999), vol. 83: pp. 661–665 (cit. on p. 2).

[25] Tojo, Satoshi, Yoshihisa Taguchi, Yuta Masuyama, Taro Hayashi, Hiroki Saito, and Takuya Hirano: 'Controlling phase separation of binary Bose-Einstein condensates via mixed-spin-channel Feshbach resonance'. *Phys. Rev. A* (3 Sept. 2010), vol. 82: p. 033609 (cit. on p. 2).

[26] Papp, S. B., J. M. Pino, and C. E. Wieman: 'Tunable Miscibility in a Dual-Species Bose-Einstein Condensate'. *Phys. Rev. Lett.* (4 July 2008), vol. 101: p. 040402 (cit. on pp. 2, 41, 43, 45).

[27] Altin, P. A., N. P. Robins, D. Döring, J. E. Debs, R. Poldy, C. Figl, and J. D. Close: 'R85b tunable-interaction Bose–Einstein condensate machine'. *Review of Scientific Instruments* (2010), vol. 81(6), 063103: pages (cit. on p. 2).

[28] Thalhammer, G., G. Barontini, L. De Sarlo, J. Catani, F. Minardi, and M. Inguscio: 'Double Species Bose-Einstein Condensate with Tunable Interspecies Interactions'. *Phys. Rev. Lett.* (21 May 2008), vol. 100: p. 210402 (cit. on pp. 2, 45).

[29] Pilch, K., A. D. Lange, A. Prantner, G. Kerner, F. Ferlaino, H.-C. Nägerl, and R. Grimm: 'Observation of interspecies Feshbach resonances in an ultracold Rb-Cs mixture'. *Phys. Rev. A* (4 Apr. 2009), vol. 79: p. 042718 (cit. on p. 2).

[30] McCarron, D. J., H. W. Cho, D. L. Jenkin, M. P. Köppinger, and S. L. Cornish: 'Dual-species Bose-Einstein condensate of ^{87}Rb and ^{133}Cs'. *Phys. Rev. A* (1 July 2011), vol. 84: p. 011603 (cit. on p. 2).

[31] Baumer, F., F. Münchow, A. Görlitz, S. E. Maxwell, P. S. Julienne, and E. Tiesinga: 'Spatial separation in a thermal mixture of ultracold ^{174}Yb and ^{87}Rb atoms'. *Phys. Rev. A* (4 Apr. 2011), vol. 83: p. 040702 (cit. on p. 2).

[32] Ho, Tin-Lun and V. B. Shenoy: 'Binary Mixtures of Bose Condensates of Alkali Atoms'. *Phys. Rev. Lett.* (16 Oct. 1996), vol. 77: pp. 3276–3279 (cit. on pp. 2, 3).

[33] Alexandrov, A S and V V Kabanov: 'Excitations and phase segregation in a two-component Bose-Einstein condensate with an arbitrary interaction'. *Journal of Physics: Condensed Matter* (2002), vol. 14(18): p. L327 (cit. on p. 2).

[34] Ao, P. and S. T. Chui: 'Binary Bose-Einstein condensate mixtures in weakly and strongly segregated phases'. *Phys. Rev. A* (6 Dec. 1998), vol. 58: pp. 4836–4840 (cit. on pp. 2, 3, 41).

[35] Barankov, R. A.: 'Boundary of two mixed Bose-Einstein condensates'. *Phys. Rev. A* (1 July 2002), vol. 66: p. 013612 (cit. on p. 2).

[36] Ejnisman, Renato, Han Pu, York Young, Nicholas Bigelow, and C. Law: 'Studies of two-species Bose-Einstein condesation'. *Opt. Express* (Apr. 1998), vol. 2(8): pp. 330–337 (cit. on p. 2).

[37] Kuo, Yuen-Cheng and Shih-Feng Shieh: 'Phase separation of multi-component Bose–Einstein condensates in optical lattices'. *Journal of Mathematical Analysis and Applications* (2008), vol. 347(2): pp. 521–533 (cit. on pp. 2, 3, 41).

[38] Pattinson, R. W., T. P. Billam, S. A. Gardiner, D. J. McCarron, H. W. Cho, S. L. Cornish, N. G. Parker, and N. P. Proukakis: 'Equilibrium solutions for immiscible two-species Bose-Einstein condensates in perturbed harmonic traps'. *Phys. Rev. A* (1 Jan. 2013), vol. 87: p. 013625 (cit. on p. 2).

[39] Pu, H. and N. P. Bigelow: 'Properties of Two-Species Bose Condensates'. *Phys. Rev. Lett.* (6 Feb. 1998), vol. 80: pp. 1130–1133 (cit. on pp. 2, 3).

[40] Navarro, R., R. Carretero-González, and P. G. Kevrekidis: 'Phase separation and dynamics of two-component Bose-Einstein condensates'. *Phys. Rev. A* (2 Aug. 2009), vol. 80: p. 023613 (cit. on p. 2).

[41] Ronen, Shai, John L. Bohn, Laura Elisa Halmo, and Mark Edwards: 'Dynamical pattern formation during growth of a dual-species Bose-Einstein condensate'. *Phys. Rev. A* (5 Nov. 2008), vol. 78: p. 053613 (cit. on p. 2).

[42] Sinatra, A. and Y. Castin: 'Binary mixtures of Bose-Einstein condensates: Phase dynamics and spatial dynamics'. *Eur. Phys. J. D* (2000), vol. 8(3): pp. 319–332 (cit. on pp. 2, 41).

[43] Svidzinsky, A. A. and S. T. Chui: 'Symmetric-asymmetric transition in mixtures of Bose-Einstein condensates'. *Phys. Rev. A* (5 May 2003), vol. 67: p. 053608 (cit. on p. 2).

[44] Timmermans, E.: 'Phase Separation of Bose-Einstein Condensates'. *Phys. Rev. Lett.* (26 Dec. 1998), vol. 81: pp. 5718–5721 (cit. on p. 2).

[45] Trippenbach, M., K. Goral, K. Rzazewski, B. Malomed, and Y. B. Band: 'Structure of binary Bose-Einstein condensates'. *J. Phys. B: At. Mol. Opt. Phys.* (19 Apr. 2000), vol. 33: pp. 4017–4031 (cit. on p. 2).

[46] Wen, L., W. M. Liu, Yongyong Cai, J. M. Zhang, and Jiangping Hu: 'Controlling phase separation of a two-component Bose-Einstein condensate by confinement'. *Phys. Rev. A* (4 Apr. 2012), vol. 85: p. 043602 (cit. on p. 2).

[47] Graham, Robert and Dan Walls: 'Collective excitations of trapped binary mixtures of Bose-Einstein condensed gases'. *Phys. Rev. A* (1 Jan. 1998), vol. 57: pp. 484–487 (cit. on p. 2).

[48] Busch, Th., J. I. Cirac, V. M. Pérez-García, and P. Zoller: 'Stability and collective excitations of a two-component Bose-Einstein condensed gas: A moment approach'. *Phys. Rev. A* (4 Oct. 1997), vol. 56: pp. 2978–2983 (cit. on p. 2).

[49] Skryabin, Dmitry V.: 'Instabilities of vortices in a binary mixture of trapped Bose-Einstein condensates: Role of collective excitations with positive and negative energies'. *Phys. Rev. A* (1 Dec. 2000), vol. 63: p. 013602 (cit. on p. 2).

[50] Gross, Eugene P.: 'Unified Theory of Interacting Bosons'. *Phys. Rev.* (1 Apr. 1957), vol. 106: pp. 161–162 (cit. on pp. 2, 7).

[51] Gross, E. P.: 'Structure of Quantized Vortex in Boson Systems'. *Il Nuovo Cimento* (454 1961), vol. 20 (cit. on pp. 2, 7).

[52] Gross, E. P.: 'Hydrodynamics of a Superfluid Condensate'. *Journal of Mathematical Physics* (195 1963), vol. 4 (cit. on pp. 2, 7).

[53] Ginzburg, V. L. and L. P. Pitaevskii. *Sov. Phys. JETP* (858 1958), vol. 7 (cit. on pp. 2, 7, 43).

[54] C. Sulem, P.L. Sulem: *The Nonlinear Schrödinger Equation: Self-Focusing and Wave Collapse*. Springer, 1999 (cit. on p. 2).

[55] Moerdijk, A. J., B. J. Verhaar, and A. Axelsson: 'Resonances in ultracold collisions of ^{6}Li, ^{7}Li, and ^{23}Na'. *Phys. Rev. A* (6 June 1995), vol. 51: pp. 4852–4861 (cit. on p. 2).

[56] Bradley, C. C., C. A. Sackett, J. J. Tollett, and R. G. Hulet: 'Evidence of Bose-Einstein Condensation in an Atomic Gas with Attractive Interactions'. *Phys. Rev. Lett.* (9 Aug. 1995), vol. 75: pp. 1687–1690 (cit. on p. 2).

[57] Fano, Ugo: 'edited by Guido Pupillo, Alberto Zannoni, and Charles W. Clark, http://arxiv.org/pdf/cond-mat/0502210v1.pdf, n the absorption spectrum of noble gases at the arc spectrum limit, A translation from the Italian original'. *Nuovo Cimento, 12, 154-161* (1935), vol. (cit. on p. 2).

[58] Feshbach, Herman: 'Unified theory of nuclear reactions'. *Annals of Physics* (1958), vol. 5(4): pp. 357–390 (cit. on p. 2).

[59] Courteille, Ph., R. S. Freeland, D. J. Heinzen, F. A. van Abeelen, and B. J. Verhaar: 'Observation of a Feshbach Resonance in Cold Atom Scattering'. *Phys. Rev. Lett.* (1 July 1998), vol. 81: pp. 69–72 (cit. on pp. 2, 11).

[60] Tiesinga, E., B. J. Verhaar, and H. T. C. Stoof: 'Threshold and resonance phenomena in ultracold ground-state collisions'. *Phys. Rev. A* (5 May 1993), vol. 47: pp. 4114–4122 (cit. on p. 2).

[61] Inouye, S., M. R. Andrewsand J. Stenger, H.-J. Miesner, D. M. Stamper-Kurn, and W. Ketterle: 'OObservation of feshbach resonances in a bose-einstein condensate'. *Nature* (Mar. 1998), vol. 392: pp. 151–154 (cit. on p. 2).

[62] Inouye, S., J. Goldwin, M. L. Olsen, C. Ticknor, J. L. Bohn, and D. S. Jin: 'Observation of Heteronuclear Feshbach Resonances in a Mixture of Bosons and Fermions'. *Phys. Rev. Lett.* (18 Oct. 2004), vol. 93: p. 183201 (cit. on pp. 2, 11, 12).

[63] Roberts, J. L., N. R. Claussen, James P. Burke, Chris H. Greene, E. A. Cornell, and C. E. Wieman: 'Resonant Magnetic Field Control of Elastic Scattering in Cold ^{85}Rb'. *Phys. Rev. Lett.* (23 Dec. 1998), vol. 81: pp. 5109–5112 (cit. on pp. 2, 11).

[64] Donley, E. A., N. R. Claussen, S. L. Cornish, J. L. Roberts, E. A. Cornell, and C. E. Wieman: 'Dynamics of collapsing and exploding Bose-Einstein condensates'. *Nature* (4 July 2001), vol. 83: pp. 295–299 (cit. on pp. 2, 11, 14).

[65] Weber, Tino, Jens Herbig, Michael Mark, Hanns-Christoph Nägerl, and Rudolf Grimm: 'Bose-Einstein Condensation of Cesium'. *Science* (2003), vol. 299(5604): pp. 232–235 (cit. on pp. 2, 11, 25).

[66] Cornish, S. L., N. R. Claussen, J. L. Roberts, E. A. Cornell, and C. E. Wieman: 'Stable ^{85}Rb Bose-Einstein Condensates with Widely Tunable Interactions'. *Phys. Rev. Lett.* (9 Aug. 2000), vol. 85: pp. 1795–1798 (cit. on pp. 2, 11).

[67] Lamine, Brahim, Rémy Hervé, Astrid Lambrecht, and Serge Reynaud: 'Ultimate Decoherence Border for Matter-Wave Interferometry'. *Phys. Rev. Lett.* (5 Feb. 2006), vol. 96: p. 050405 (cit. on p. 2).

[68] Hariharan, P.: *Optical Inteferometry*. Elsevier - Academic Press: New York, NY, USA, 2003 (cit. on p. 2).

[69] Fabry, L. and A. Perot. *Ann. Chim. Phys. Théorie et applications dune nouvelle méthode de Spectroscopie Interférentielle 16(7), 115* (1889), vol. (cit. on p. 2).

[70] Fizeau, H. *Ann. Phys. Chem. 3, 457* (1853), vol. (cit. on p. 2).

[71] Michelson, A. A. *Am. J. Sci. 22, 20* (1881), vol. (cit. on p. 2).

[72] Rayleigh, L.: 'On copying diffraction-gratings, and on some phenomena connected therewith'. *Philos. Mag. 11,196* (1881), vol. (cit. on p. 2).

[73] Altschuler, S. and L. M. Franz: 'Matter wave interferometric apparatus'. 3,761,721 (cit. on p. 2).

[74] Clauser, J.F.: 'Rotation, acceleration, and gravity sensors using quantum-mechanical matter-wave interferometry with neutral atoms and molecules'. US Patent 4,874,942. Oct. 1989 (cit. on p. 2).

[75] Chebotayev, V. P., A. P. Kasantsev, V. P. Yakovlev, and B. Ya. Dubetsky: 'Interference of atoms in separated optical fields'. *J. Opt. Soc. Am. B* (Nov. 1985), vol. 2(11): pp. 1791–1798 (cit. on p. 2).

[76] Clauser, J. F.: 'Ultra high sensitivity accelerometers and gyroscopes using neutral atom matter wave interferometry'. *Physica B and C 151, 262* (1988), vol. (cit. on p. 2).

[77] Keith, David W., Christopher R. Ekstrom, Quentin A. Turchette, and David E. Pritchard: 'An interferometer for atoms'. *Phys. Rev. Lett.* (21 May 1991), vol. 66: pp. 2693–2696 (cit. on pp. 2, 66).

[78] Zehnder, L.: 'Ein neuer Interferenzrefraktor'. *Zeitschrift für Instrumentenkunde 11: 275–285* (1891), vol. (cit. on p. 2).

[79] Mach, L.: 'Ueber einen Interferenzrefraktor'. *Zeitschrift für Instrumentenkunde 12: 89–93* (1892), vol. (cit. on p. 2).

[80] Kasevich, M. and S. Chu: 'Atomic interferometry using stimulated Raman transitions'. *Phys. Rev. Lett. 67, 181* (1991), vol. (cit. on pp. 2, 66).

[81] Bouchendira, Rym, Pierre Cladé, Saïda Guellati-Khélifa, Fran çois Nez, and Fran çois Biraben: 'New Determination of the Fine Structure Constant and Test of the Quantum Electrodynamics'. *Phys. Rev. Lett.* (8 Feb. 2011), vol. 106: p. 080801 (cit. on p. 3).

[82] Dimopoulos, Savas, Peter W. Graham, Jason M. Hogan, and Mark A. Kasevich: 'General relativistic effects in atom interferometry'. *Physical Review D* (Aug. 2008), vol. 78(4): p. 042003 (cit. on p. 3).

[83] Dimopoulos, Savas, Peter W. Graham, Jason M. Hogan, and Mark A. Kasevich: 'Testing General Relativity with Atom Interferometry'. *Phys. Rev. Lett.* (11 Mar. 2007), vol. 98: p. 111102 (cit. on p. 3).

[84] Dimopoulos, Savas, Peter W. Graham, Jason M. Hogan, Mark A. Kasevich, and Surjeet Rajendran: 'Atomic gravitational wave interferometric sensor'. *Physical Review D* (Dec. 2008), vol. 78(12): p. 122002 (cit. on p. 3).

[85] Fixler, J. B., G. T. Foster, J. M. McGuirk, and M. A. Kasevich: 'Atom Interferometer Measurement of the Newtonian Constant of Gravity'. *Science* (Jan. 2007), vol. 315(5808). PMID: 17204644: pp. 74–77 (cit. on p. 3).

[86] Lamporesi, G., A. Bertoldi, L. Cacciapuoti, M. Prevedelli, and G. M. Tino: 'Determination of the Newtonian Gravitational Constant Using Atom Interferometry'. *Phys. Rev. Lett.* (5 Feb. 2008), vol. 100: p. 050801 (cit. on p. 3).

[87] McGuirk, J. M., G. T. Foster, J. B. Fixler, M. J. Snadden, and M. A. Kasevich: 'Sensitive absolute-gravity gradiometry using atom interferometry'. *Phys. Rev. A* (3 Feb. 2002), vol. 65: p. 033608 (cit. on p. 3).

[88] Damour, Thibault and John F. Donoghue: 'Phenomenology of the Equivalence Principle with Light Scalars'. *Class. Quant. Grav.* (2010), vol. 27: p. 202001 (cit. on p. 3).

[89] Damour, T.: 'Testing the equivalence principle: why and how?' *Class. Quantum Grav. 13 A33* (1996), vol. (cit. on p. 3).

[90] Berman, P. R.: *Atom Interferometry*. Academic Press, San Diego, CA, 1997 (cit. on pp. 3, 66).

[91] Cronin, Alexander D., Jörg Schmiedmayer, and David E. Pritchard: 'Optics and interferometry with atoms and molecules'. *Rev. Mod. Phys.* (3 July 2009), vol. 81: pp. 1051–1129 (cit. on p. 3).

[92] Will, C. M.: *General Relativity and John Archibald Wheeler*. Astrophysics and Space Science Library, Volume 367, pp 73-93, 2010 (cit. on p. 3).

[93] Kiefer, C.: *Quantum Gravity*. Oxford University Press, Oxford, 2007 (cit. on p. 3).

[94] Damour, T., F. Piazza, and G. Veneziano: 'Violations of the equivalence principle in a dilaton-runaway scenario'. *Phys. Rev. D* (4 Aug. 2002), vol. 66: p. 046007 (cit. on p. 3).

[95] Sandvik, Håvard Bunes, John D. Barrow, and João Magueijo: 'A Simple Cosmology with a Varying Fine Structure Constant'. *Phys. Rev. Lett.* (3 Jan. 2002), vol. 88: p. 031302 (cit. on p. 3).

[96] Fray, Sebastian, Cristina Alvarez Diez, Theodor W. Hänsch, and Martin Weitz: 'Atomic Interferometer with Amplitude Gratings of Light and Its Applications to Atom Based Tests of the Equivalence Principle'. *Phys. Rev. Lett.* (24 Dec. 2004), vol. 93: p. 240404 (cit. on p. 3).

[97] Schlamminger, S., K.-Y. Choi, T. A. Wagner, J. H. Gundlach, and E. G. Adelberger: 'Test of the Equivalence Principle Using a Rotating Torsion Balance'. *Phys. Rev. Lett.* (4 Jan. 2008), vol. 100: p. 041101 (cit. on pp. 3, 65, 66).

[98] Williams, James G., Slava G. Turyshev, and Dale H. Boggs: 'Progress in Lunar Laser Ranging Tests of Relativistic Gravity'. *Phys. Rev. Lett.* (26 Dec. 2004), vol. 93: p. 261101 (cit. on pp. 3, 66).

[99] Bonnin, A., N. Zahzam, Y. Bidel, and A. Bresson: 'Simultaneous dual-species matter-wave accelerometer'. *Phys. Rev. A* (4 Oct. 2013), vol. 88: p. 043615 (cit. on p. 3).

[100] Tino, G. M.: 'Testing gravity with atom interferometry'. *Lecture II in "E. Fermi" School on Atom Interferometry, Varenna*. July 2013 (cit. on p. 3).

[101] Rudolph, J. et al.: 'Degenerate Quantum Gases in Microgravity'. *Microgravity Science and Technology, Volume 23, Issue 3, pp 287-292* (2011), vol. (cit. on p. 3).

[102] Zoest, T. van et al.: 'Bose-Einstein Condensation in Microgravity'. *Science, Vol. 328 no. 5985 pp. 1540-1543* (2010), vol. (cit. on p. 3).

[103] Müller, Holger, Sheng-wey Chiow, Sven Herrmann, Steven Chu, and Keng-Yeow Chung: 'Atom-Interferometry Tests of the Isotropy of Post-Newtonian Gravity'. *Phys. Rev. Lett.* (3 Jan. 2008), vol. 100: p. 031101 (cit. on p. 3).

[104] Geiger, R., V. Ménoret, G. Stern, N. Zahzam, P. Cheinet, B. Battelier, A. Villing, F. Moron, M. Lours, Y. Bidel, A. Bresson, A. Landragin, and P. Bouyer: 'Detecting inertial effects with airborne matter-wave interferometry'. *Nature Communications 2, Article number: 474* (2011), vol. (cit. on p. 3).

[105] Aguilera, D N et al.: 'STE-QUEST—test of the universality of free fall using cold atom interferometry'. *Classical and Quantum Gravity* (2014), vol. 31(11): p. 115010 (cit. on pp. 3, 4, 65, 66, 69, 72).

[106] Tino, G.M. et al.: 'Precision Gravity Tests with Atom Interferometry in Space'. *Nuclear Physics B - Proceedings Supplements, Volumes 243–244* (2013), vol. (cit. on p. 3).

[107] Ammann, Hubert and Nelson Christensen: 'Delta Kick Cooling: A New Method for Cooling Atoms'. *Phys. Rev. Lett.* (11 Mar. 1997), vol. 78: pp. 2088–2091 (cit. on pp. 3, 18).

[108] Chu, S., J. E. Bjorkholm, A. Ashkin, J. P. Gordon, and L. W. Hollberg: 'Proposal for optically cooling atoms to temperatures of the order of 106 K'. *Opt. Lett.* (Feb. 1986), vol. 11(2): pp. 73–75 (cit. on p. 3).

[109] Morinaga, M., I. Bouchoule, J.-C. Karam, and C. Salomon: 'Manipulation of Motional Quantum States of Neutral Atoms'. *Phys. Rev. Lett. 83, 4037* (1999), vol. (cit. on p. 3).

[110] Varoquaux, G., R. A. Nyman, R. Geiger, P. Cheinet, A. Landragin, and P. Bouyer: 'How to estimate the differential acceleration in a two-species atom interferometer to test the equivalence principle'. *New Journal of Physics 11, 113010, 14pp* (2009), vol. (cit. on p. 3).

[111] Mertes, K. M., J. W. Merrill, R. Carretero-González, D. J. Frantzeskakis, P. G. Kevrekidis, and D. S. Hall: 'Nonequilibrium Dynamics and Superfluid Ring Excitations in Binary Bose-Einstein Condensates'. *Phys. Rev. Lett. 99, 190402* (2007), vol. (cit. on p. 3).

[112] Riboli, Francesco and Michele Modugno: 'Topology of the ground state of two interacting Bose-Einstein condensates'. *Phys. Rev. A 65, 063614* (2002), vol. (cit. on pp. 3, 41).

[113] Ketterle, W., D.S. Durfee, and D.M. Stamper-Kurn: 'Making, probing and understanding Bose-Einstein condensates'. *Volume 140: Bose-Einstein Condensation in Atomic Gases*. Ed. by International School of Physics Enrico Fermi, Proceedings of the. The Netherlands: IOS Press Ebooks, 2012: pp. 67–176 (cit. on p. 41).

[114] URL: http://www.iqo.uni-hannover.de/quantus.html (cit. on pp. 3, 35).

[115] team, STE-QUEST: *Space-Time Explorer and QUantum Equivalence Space Test: Assessment Study Report, Yellow Book of STE-QUEST*. Tech. rep. ESA/SRE, 2013 (cit. on pp. 3, 4, 66).

[116] Schuldt, Thilo et al.: 'Design of a dual species atom interferometer for space'. English. *Experimental Astronomy* (2015), vol. 39(2): pp. 167–206 (cit. on pp. 4, 66, 75, 79).

[117] Posso-Trujillo, K., Ahlers H., Schubert C., Hartwig J. Gaaloul N., and Rasel E. M.: 'Interacting quantum mixtures for precision atom interferometry'. Pre-print (cit. on p. 4).

[118] Drake, T. E., Y. Sagi, R. Paudel, J. T. Stewart, J. P. Gaebler, and D. S. Jin: 'Direct observation of the Fermi surface in an ultracold atomic gas'. *Phys. Rev. A* (3 Sept. 2012), vol. 86: p. 031601.

[119] Ho, T.L. and Q. Zhouc: 'Obtaining the phase diagram and thermodynamic quantities of bulk systems from the densities of trapped gases'. *Nature Physics* (2010), vol. 6(2): pp. 131–134.

[120] Hung, C. L., X. Zhang, N. Gemelke, and C. Chin: 'Observation of scale invariance and universality in two-dimensional Bose gases'. *Nature* (Jan. 2011), vol. 470: pp. 236–239.

[121] Ku, Mark J. H., Ariel T. Sommer, Lawrence W. Cheuk, and Martin W. Zwierlein: 'Revealing the Superfluid Lambda Transition in the Universal Thermodynamics of a Unitary Fermi Gas'. *Science* (2012), vol. 335(6068): pp. 563–567.

[122] Nascimbène, S., N. Navon, K. J. Jiang, F. Chevy, and C. Salomon: 'Exploring the thermodynamics of a universal Fermi gas'. *Nature* (Feb. 2010), vol. 463: pp. 1057–1060.

[123] Navon, N., S. Nascimbène, F. Chevy, and C. Salomon: 'The Equation of State of a Low-Temperature Fermi Gas with Tunable Interactions'. *Science* (2010), vol. 328(5979): pp. 729–732.

[124] Sagi, Yoav, Tara E. Drake, Rabin Paudel, and Deborah S. Jin: 'Measurement of the Homogeneous Contact of a Unitary Fermi Gas'. *Phys. Rev. Lett.* (22 Nov. 2012), vol. 109: p. 220402.

[125] Smith, R. P., N. Tammuz, R. L. D. Campbell, M. Holzmann, and Z. Hadzibabic: 'Condensed Fraction of an Atomic Bose Gas Induced by Critical Correlations'. *Phys. Rev. Lett.* (19 Nov. 2011), vol. 107: p. 190403.

[126] Yefsah, Tarik, Rémi Desbuquois, Lauriane Chomaz, Kenneth J. Günter, and Jean Dalibard: 'Exploring the Thermodynamics of a Two-Dimensional Bose Gas'. *Phys. Rev. Lett.* (13 Sept. 2011), vol. 107: p. 130401.

[127] Bogoliubov, N. N.: 'On the theory of superfluidity'. *J. Phys. USSR 11, 23* (1947), vol.

[128] Kagan, Yu., E. L. Surkov, and G. V. Shlyapnikov: 'Evolution and Global Collapse of Trapped Bose Condensates under Variations of the Scattering Length'. *Phys. Rev. Lett.* (14 Oct. 1997), vol. 79: pp. 2604–2607 (cit. on pp. 8, 50, 93).

[129] Y., Castin and Dum R.: 'Bose-Einstein Condensates in Time Dependent Traps'. *Phys. Rev. Lett. 77, 5315* (1996), vol. (cit. on pp. 8, 50).

[130] Volz, Thomas, Stephan Dürr, Sebastian Ernst, Andreas Marte, and Gerhard Rempe: 'Characterization of elastic scattering near a Feshbach resonance in ^{87}Rb'. *Phys. Rev. A* (1 July 2003), vol. 68: p. 010702 (cit. on p. 9).

[131] Bohn, John L. and P. S. Julienne: 'Prospects for influencing scattering lengths with far-off-resonant light'. *Phys. Rev. A* (2 Aug. 1997), vol. 56: pp. 1486–1491 (cit. on p. 12).

[132] Fedichev, P. O., M. W. Reynolds, and G. V. Shlyapnikov: 'Three-Body Recombination of Ultracold Atoms to a Weakly Bound *s* Level'. *Phys. Rev. Lett.* (14 Sept. 1996), vol. 77: pp. 2921–2924 (cit. on pp. 12, 14).

[133] Fatemi, F. K., K. M. Jones, and P. D. Lett: 'Observation of Optically Induced Feshbach Resonances in Collisions of Cold Atoms'. *Phys. Rev. Lett.* (21 Nov. 2000), vol. 85: pp. 4462–4465 (cit. on p. 12).

[134] Theis, Matthias: 'Optical Feshbach Resonances in a Bose-Einstein Condensate'. PhD thesis. Leopold-Franzens-Universitfat Innsbruck, 2005 (cit. on p. 12).

[135] Ruprecht, P. A., M. J. Holland, K. Burnett, and Mark Edwards: 'Time-dependent solution of the nonlinear Schrödinger equation for Bose-condensed trapped neutral atoms'. *Phys. Rev. A* (6 June 1995), vol. 51: pp. 4704–4711 (cit. on p. 13).

[136] Gammal, A., T. Frederico, and Lauro Tomio: 'Improved numerical approach for the time-independent Gross-Pitaevskii nonlinear Schrödinger equation'. *Phys. Rev. E* (2 Aug. 1999), vol. 60: pp. 2421–2424 (cit. on p. 13).

[137] Sirohi, Rajpal: *Optical Methods of Measurement: Wholefield Techniques*. Second. Wholefield Techniques, 2009: p. 46 (cit. on p. 19).

[138] Myrskog, S. H., J. K. Fox, and A. M. Steinberg: 'Nanokelvin of the North'. *Physics in Canada* (July 1999), vol. 55 (cit. on p. 20).

[139] W. Hänsel P. Hommelhoff, T. W. Hänsch and J. Reichel: 'Bose–Einstein condensation on a microelectronic chip'. *Nature* (2001), vol. 413: pp. 498–501 (cit. on p. 25).

[140] Arnold, A. S. and E. Riis. *J. Mod. Optics* (1999), vol. 49: p. 5861 (cit. on p. 25).

[141] Gupta, S., K. W. Murch, K. L. Moore, T. P. Purdy, and D. M. Stamper-Kurn: 'Bose-Einstein Condensation in a Circular Waveguide'. *Phys. Rev. Lett.* (14 Sept. 2005), vol. 95: p. 143201 (cit. on p. 25).

[142] Petrich, Wolfgang, Michael H. Anderson, Jason R. Ensher, and Eric A. Cornell: 'Stable, Tightly Confining Magnetic Trap for Evaporative Cooling of Neutral Atoms'. *Phys. Rev. Lett.* (17 Apr. 1995), vol. 74: pp. 3352–3355 (cit. on p. 25).

[143] Letokhov, V.S. *JETP Lett. 7, 272* (1968), vol. (cit. on p. 25).

[144] Ashkin, A.: 'Trapping of Atoms by Resonance Radiation Pressure'. *Phys. Rev. Lett.* (12 Mar. 1978), vol. 40: pp. 729–732 (cit. on p. 25).

[145] Anderson, B. P. and M. A. Kasevich: 'Macroscopic Quantum Interference from Atomic Tunnel Arrays'. *Science* (1998), vol. 282(5394): pp. 1686–1689 (cit. on p. 25).

[146] Stamper-Kurn, D. M., M. R. Andrews, A. P. Chikkatur, S. Inouye, H.-J. Miesner, J. Stenger, and W. Ketterle: 'Optical Confinement of a Bose-Einstein Condensate'. *Phys. Rev. Lett.* (10 Mar. 1998), vol. 80: pp. 2027–2030 (cit. on p. 25).

[147] Barrett, M. D., J. A. Sauer, and M. S. Chapman: 'All-Optical Formation of an Atomic Bose-Einstein Condensate'. *Phys. Rev. Lett.* (1 June 2001), vol. 87: p. 010404 (cit. on p. 25).

[148] Kinoshita, Toshiya, Trevor Wenger, and David S. Weiss: 'All-optical Bose-Einstein condensation using a compressible crossed dipole trap'. *Phys. Rev. A* (1 Jan. 2005), vol. 71: p. 011602 (cit. on p. 25).

[149] Takasu, Yosuke, Kenichi Maki, Kaduki Komori, Tetsushi Takano, Kazuhito Honda, Mitsutaka Kumakura, Tsutomu Yabuzaki, and Yoshiro Takahashi: 'Spin-Singlet Bose-Einstein Condensation of Two-Electron Atoms'. *Phys. Rev. Lett.* (4 July 2003), vol. 91: p. 040404 (cit. on p. 25).

[150] Grimm R. Weidemüller, Ovchinnikov Yr. B.: 'Optical dipole traps for neutral atoms'. *Advances in Atomic, Molecular and Optical Physics Vol. 42, 95-170* (2000), vol. (cit. on pp. 25, 26).

[151] Bjorkholm, J. E., R. R. Freeman, A. Ashkin, and D. B. Pearson: 'Observation of Focusing of Neutral Atoms by the Dipole Forces of Resonance-Radiation Pressure'. *Phys. Rev. Lett.* (20 Nov. 1978), vol. 41: pp. 1361–1364 (cit. on p. 26).

[152] Christopher Pethick, Henrik Smith: *Bose-Einstein Condensation in Dilute Gases*. Cambridge University Press, 2002 (cit. on p. 26).

[153] Chu, Steven, J. E. Bjorkholm, A. Ashkin, and A. Cable: 'Experimental Observation of Optically Trapped Atoms'. *Phys. Rev. Lett.* (3 July 1986), vol. 57: pp. 314–317 (cit. on p. 26).

[154] Pritchard, David E.: 'Cooling Neutral Atoms in a Magnetic Trap for Precision Spectroscopy'. *Phys. Rev. Lett.* (15 Oct. 1983), vol. 51: pp. 1336–1339 (cit. on p. 27).

[155] Huray, Paul G.: *Maxwell's Equations*. Published by John Wiley and Sons, New Jersey, 2010 (cit. on p. 28).

[156] Krishan K. Sud, Upendra N. Upadhyaya, ed.: *Trends in Atomic and Molecular Physics*. Proceedings of the XII National Conference on Atomic and Molecular Physics. Udaipur, India, 1999 (cit. on p. 29).

[157] Abramowitz and Stegun: *Handbook of Mathematical Functions*. Ed. by Abramowitz, Milton and Irene A. Stegun. Dover Publications, 1964 (cit. on p. 32).

[158] url: http://www.iqo.uni-hannover.de/551.html (cit. on p. 35).

[159] Walters, G. K. and W. M. Fairbank: 'Phase Separation in He^3He^4 Solutions'. *Phys. Rev.* (1 July 1956), vol. 103: pp. 262–263 (cit. on pp. 41, 43).

[160] Gaunt, Alexander L., Tobias F. Schmidutz, Igor Gotlibovych, Robert P. Smith, and Zoran Hadzibabic: 'Bose-Einstein Condensation of Atoms in a Uniform Potential'. *Phys. Rev. Lett.* (20 May 2013), vol. 110: p. 200406 (cit. on p. 44).

[161] Burke, James P., John L. Bohn, B. D. Esry, and Chris H. Greene: 'Prospects for Mixed-Isotope Bose-Einstein Condensates in Rubidium'. *Phys. Rev. Lett.* (10 Mar. 1998), vol. 80: pp. 2097–2100 (cit. on p. 45).

[162] Masahito Ueda, Hiroki Saito: *Bose-Einstein Condensation with Attractive Interaction Fate of a False Vacuum, Macroscopic Quantum Coherence and Quantum Computing*. Springer Science+Business Media New york, 2001 (cit. on p. 47).

[163] Simoni, A., F. Ferlaino, G. Roati, G. Modugno, and M. Inguscio: 'Magnetic Control of the Interaction in Ultracold K-Rb Mixtures'. *Phys. Rev. Lett.* (16 Apr. 2003), vol. 90: p. 163202 (cit. on pp. 47, 48).

[164] Falke, Stephan, Horst Knöckel, Jan Friebe, Matthias Riedmann, Eberhard Tiemann, and Christian Lisdat: 'Potassium ground-state scattering parameters and Born-Oppenheimer potentials from molecular spectroscopy'. *Phys. Rev. A* (1 July 2008), vol. 78: p. 012503 (cit. on p. 48).

[165] Claussen, N. R., S. J. J. M. F. Kokkelmans, S. T. Thompson, E. A. Donley, E. Hodby, and C. E. Wieman: 'Very-high-precision bound-state spectroscopy near a ^{85}Rb Feshbach resonance'. *Phys. Rev. A* (6 June 2003), vol. 67: p. 060701 (cit. on p. 13).

[166] D'Errico, Chiara, Matteo Zaccanti, Marco Fattori, Giacomo Roati, Massimo Inguscio, Giovanni Modugno, and Andrea Simoni: 'Feshbach resonances in ultracold 39 K'. *New Journal of Physics* (2007), vol. 9(7): p. 223 (cit. on pp. 13, 48).

[167] Kitagawa, Masaaki, Katsunari Enomoto, Kentaro Kasa, Yoshiro Takahashi, Roman Ciuryło, Pascal Naidon, and Paul S. Julienne: 'Two-color photoassociation spectroscopy of ytterbium atoms and the precise determinations of s-wave scattering lengths'. *Phys. Rev. A* (1 Jan. 2008), vol. 77: p. 012719 (cit. on p. 49).

[168] Borkowski, Mateusz, Piotr S. Żuchowski, Roman Ciuryło, Paul S. Julienne, Dariusz K ędziera, Łukasz Mentel, Paweł Tecmer, Frank Münchow, Cristian Bruni, and Axel Görlitz: 'Scattering lengths in isotopologues of the RbYb system'. *Phys. Rev. A* (5 Nov. 2013), vol. 88: p. 052708 (cit. on p. 49).

[169] URL: http://sci.esa.int/ste-quest/ (cit. on p. 65).

[170] Hartwig, J, S Abend, C Schubert, D Schlippert, H Ahlers, K Posso-Trujillo, N Gaaloul, W Ertmer, and E M Rasel: 'Testing the universality of free fall with rubidium and ytterbium in a very large baseline atom interferometer'. *New Journal of Physics* (2015), vol. 17(3): p. 035011 (cit. on pp. 65, 66).

[171] Robinson, Matthew: *Symmetry and the Standard Model: Mathematics and Particle Physics*. Springer Verlag, 327 pp, 2011 (cit. on p. 65).

[172] Ciufolini, I. and J. A. Wheeler: *Gravitation and Inertia*. Princeton University Press, 1995: p. 284 (cit. on p. 65).

[173] Rindler, W.: *Essential Relativity: Special, General, and Cosmological*. Springer, Second edition, 1977 (cit. on p. 65).

[174] Will, C. M.: *Theory and experiment in gravitational physics*. Cambridge University Press, 1993 (cit. on p. 65).

[175] Shapiro, Irwin I., Charles C. Counselman, and Robert W. King: 'Verification of the Principle of Equivalence for Massive Bodies'. *Phys. Rev. Lett.* (11 Mar. 1976), vol. 36: pp. 555–558 (cit. on p. 65).

[176] Fischbach and Talmadge: *The Search for Non-Newtonian Gravity*. Springer-Verlag, New York, 1999 (cit. on p. 65).

[177] Carlip, S.: *Quantum Gravity: a Progress Report*. Tech. rep. Rep. Prog. Phys. 64, 885. http://arxiv.org/pdf/gr-qc/0108040. 2001 (cit. on p. 66).

[178] Rovelli, C.: *Notes for a brief history of quantum gravity*. 2000. URL: http://arxiv.org/pdf/gr-qc/0006061.pdf (cit. on p. 66).

[179] Touboul, P., H. Selig, M. Santos Rodrigues, A. Robert, E. Hardy, Q. Baghi, R. Chhun, G. Metris, and J. Berge: *Microscope - Testing the Weak Equivalence Principle in Space, 40th COSPAR Scientific Assembly*. Abstract H0.3-1-14. Aug. 2014. URL: http://adsabs.harvard.edu/abs/2014cosp...40E3377T (cit. on p. 66).

[180] Altschul, Brett et al.: 'Quantum Tests of the Einstein Equivalence Principle with the STE-QUEST Space Mission, Volume 55, Issue 1'. *Advances in Space Research* (2015), vol. (cit. on p. 66).

[181] Kasevich, M. and S. Chu: 'Measurement of the gravitational acceleration of an atom with a light-pulse atom interferometer'. English. *Applied Physics B* (1992), vol. 54(5): pp. 321–332 (cit. on p. 66).

[182] Riehle, F., Th. Kisters, A. Witte, J. Helmcke, and Ch. J. Bordé: 'Optical Ramsey spectroscopy in a rotating frame: Sagnac effect in a matter-wave interferometer'. *Phys. Rev. Lett.* (2 July 1991), vol. 67: pp. 177–180 (cit. on p. 66).

[183] Peters, A, K Y Chung, and S Chu: 'High-precision gravity measurements using atom interferometry'. *Metrologia* (2001), vol. 38(1): p. 25 (cit. on p. 66).

[184] Hogan, Jason M., David M. S. Johnson, and Mark A. Kasevich: *Light-pulse atom interferometry*. Stanford University. 2008. URL: http://arxiv.org/pdf/0806.3261v1.pdf (cit. on p. 67).

[185] Bordé, Ch.J.: 'Atomic interferometry with internal state labelling'. *Volume 140, Issues 1–2, Pages 10–12* (1989), vol. (cit. on p. 69).

[186] Wu, Xinan: 'Gravity Gradient Survey with a Mobile Atom Interferometer'. PhD thesis. Stanford University, 2009 (cit. on p. 69).

[187] Roura, Albert: 'Circumventing Heisenberg's Uncertainty Principle in Atom Interferometry Tests of the Equivalence Principle'. *Phys. Rev. Lett.* (16 Apr. 2017), vol. 118: p. 160401 (cit. on p. 89).

[188] Lee, T. D. and C. N. Yang: 'Many-Body Problem in Quantum Mechanics and Quantum Statistical Mechanics'. *Phys. Rev.* (3 Feb. 1957), vol. 105: pp. 1119–1120 (cit. on p. 92).

[189] Lee, T. D., Kerson Huang, and C. N. Yang: 'Eigenvalues and Eigenfunctions of a Bose System of Hard Spheres and Its Low-Temperature Properties'. *Phys. Rev.* (6 June 1957), vol. 106: pp. 1135–1145 (cit. on p. 92).

[190] Altin, P. A., G. R. Dennis, G. D. McDonald, D. Döring, J. E. Debs, J. D. Close, C. M. Savage, and N. P. Robins: 'Collapse and three-body loss in a ^{85}Rb Bose-Einstein condensate'. *Phys. Rev. A* (3 Sept. 2011), vol. 84: p. 033632 (cit. on p. 93).

[191] Agrawal, G. P.: *Nonlinear Fiber Optics*. Academic Press. (3rd ed.), 2001 (cit. on pp. 119, 120).

[192] Thalhammer, Mechthild and Jochen Abhau: 'A numerical study of adaptive space and time discretisations for Gross–Pitaevskii equations'. *Journal of Computational Physics* (2012), vol. 231(20): pp. 6665–6681 (cit. on p. 120).

[193] Cooley James W.; Tukey, John W.: 'An algorithm for the machine calculation of complex Fourier series'. *Math. Comput. 19: 297–301* (1965), vol. (cit. on p. 120).

[194] Eichler, Rüdiger, Damir Zajec, Patrick Köberle, Jörg Main, and Günter Wunner: 'Collisions of anisotropic two-dimensional bright solitons in dipolar Bose-Einstein condensates'. *Phys. Rev. A* (5 Nov. 2012), vol. 86: p. 053611 (cit. on p. 120).

[195] Press, William H., Saul A. Teukolsky, William T. Vetterling, Brian P. Flannery, and Michael Metcal: *Numerical Recipes in Fortran 90*. Vol. 2. Cambridge University Press, book On-Line. Chap. 16 (cit. on p. 120).

List of Figures

List of Tables

APPENDIX A

Chemical potential for mixtures

The chemical potential μ for a large number of particles of a BEC mixture trapped in a harmonic potential, the atoms experience repulsive interactions which make the spatial radius of the BEcs increase to a value R, detrimental to the momentum of the atoms which scales as $\hbar/R$, this is the kinetic energy is much smaller than the trapping potential energy. Therefore one neglects the kinetic energy in the time-independent GPE to obtain a functional of the BECs densities.

$$n_{1(2)} = \frac{g_{22(11)}\left(\mu_{1(2)} - U_{1(2)}\right) - g_{12}\left(\mu_{2(1)} - U_{2(1)}\right)}{(g_{11}g_{22} - g_{12}^2)} \tag{A.1}$$

The chemical potential defines a parabolic region occupied by the condensate which has a radius.

$$\left[\frac{2\mu_{1(2)}}{m_{1(2)}\omega_{\alpha 1(2)}}\right]^{1/2} = R_{\alpha 1(2)} \quad , \quad \alpha = x,y,z. \tag{A.2}$$

where $U_{1(2)}$ are the trapping potentials, $g_{22(11)}$ and g_{12} are the intra- and inter-species interactions.

By using eq. (A.2), eq. (A.1) can be written as

$$\underbrace{\frac{g_{22}}{N_2(g_{11}g_{22} - g_{12}^2)}\mu_1\left[1 - \sum_\alpha\left(\frac{r_\alpha^2}{R_{\alpha 1}^2}\right)\right]}_{1} - \underbrace{\frac{g_{12}}{N_1(g_{11}g_{22} - g_{12}^2)}\mu_2\left[1 - \sum_\alpha\left(\frac{r_\alpha^2}{R_{\alpha 2}^2}\right)\right]}_{2} = n_1$$

$$\frac{g_{11}}{N_1(g_{11}g_{22} - g_{12}^2)}\mu_2\left[1 - \sum_\alpha\left(\frac{r_\alpha^2}{R_{\alpha 2}^2}\right)\right] - \frac{g_{12}}{N_2(g_{11}g_{22} - g_{12}^2)}\mu_1\left[1 - \sum_\alpha\left(\frac{r_\alpha^2}{R_{\alpha 1}^2}\right)\right] = n_2 \tag{A.3}$$

To apply the normalization conditions $\int_V n_1 d\vec{r} = 1$ and $\int_V n_2 d\vec{r} = 1$ is convenient to make the following substitution

$$u_\alpha = \frac{r_\alpha}{R_\alpha} \quad \therefore \quad du_\alpha = \frac{1}{R_\alpha} dr_\alpha \tag{A.4}$$

normalizing the eqs. (A.3), gives

$$\begin{aligned}
&\frac{8\pi}{15}\frac{1}{N_1\left(g_{11}g_{22}-g_{12}^2\right)}\left[\mu_1 g_{22}\prod_\alpha R_{\alpha 1}-\mu_2 g_{12}\prod_\alpha R_{\alpha 2}\right]=1\\
&\frac{8\pi}{15}\frac{1}{N_1\left(g_{11}g_{22}-g_{12}^2\right)}\left[\mu_1 g_{22}\prod_\alpha R_{\alpha 1}-\mu_2 g_{12}\prod_\alpha R_{\alpha 2}\right]=1
\end{aligned} \tag{A.5}$$

Substituting the radii (A.2) in eq.(A.5) and the intra- and inter-species interaction in terms of the scattering lengths

$$g_{11}=\frac{4\pi}{m_1}a_1; \qquad g_{22}=\frac{4\pi}{m_2}a_2; \qquad g_{12}=\frac{2\pi}{m_{red}}a_{12}; \tag{A.6}$$

m_{red} is the reduced mass of the mixture. It is obtained for the chemical potential,

$$\begin{aligned}
\mu_1&=\frac{m_1^{1/5}}{2}\left[\frac{15}{2}\right]^{1/5}\left[\frac{2a_1 m_{red}N_1+a_{12}m_1N_2}{m_{red}}\right]^{1/5}\bar{\omega}_1^{6/5}\\
\mu_2&=\frac{m_2^{1/5}}{2}\left[\frac{15}{2}\right]^{1/5}\left[\frac{2a_2 m_{red}N_2+a_{12}m_2N_1}{m_{red}}\right]^{1/5}\bar{\omega}_2^{6/5}
\end{aligned} \tag{A.7}$$

where $\bar{\omega}_{1(2)}=\left(\omega_{x1(2)}\omega_{y1(2)}\omega_{z1(2)}\right)^{1/3}$

APPENDIX B

Chemical Potential. Effective 1D BEC

Atomic systems generated in potentials having highly asymmetric configurations do not allow a dimension reduction to facilitate the numerical computations. A substantial part of the previous calculations in realistic traps, detailed in the main text, chapter [2] 2 section 2.2.4, have been based in such potentials, whose study of the dynamics have been approximated to effective 1D calculations.

The purpose of this appendix is to show a calculation of the chemical potential μ^{TF} in a 1D effective interacting system, with a general interaction β_{1D}. To simplify the calculations in order to analyze a non-trivial symmetry in one of the directions of the trap.

Starting with the Thomas-Fermi approximation

$$\Psi^{TF}(x) = \begin{cases} \sqrt{\left(\mu^{TF} - V_{trap}(x)\right)/\beta_{1D}} & , V_{trap}(x) \leq \mu^{TF} \\ 0 & , \text{otherwise} \end{cases} \tag{B.1}$$

where V_{trap} is a general trapping potential, and $\beta_{1D} = \hbar 2Na\omega_{trans}$ is an interaction parameter in 1D, and ω_{trans} is the transverse harmonic oscillator frequency.

By imposing the normalization condition on the wave-function based on the Thomas-Fermi approximation, one determines the value of the chemical potential

$$\|\Psi^{TF}\|^2 = \int_L |\Psi^{TF}(x)|^2 dx = 1 \tag{B.2}$$

Considering a general potential

$$1 = \int_L |\Psi^{TF}(x)|^2 dx = \int\limits_{V_{trap}(x) \leq \mu^{TF}} \frac{\mu^{TF} - V_{trap}(x)}{\beta_{1D}} dx \tag{B.3}$$

For a typical s-wave interaction represented by the scattering length a; and considering a harmonic trap

$$V_{trap}(x) = \frac{1}{2} m\omega_x^2 x^2 \tag{B.4}$$

where m is the mass of the atom, and ω is te angular frequency. The integration limits

are now

$$\frac{m\omega^2 x^2}{2} \leq \mu^{TF} \Rightarrow x \leq \sqrt{\frac{2\mu^{TF}}{m\omega^2}} \quad \text{and} \quad x \geq -\sqrt{\frac{2\mu^{TF}}{m\omega^2}} \tag{B.5}$$

Making the substitution $x = \sqrt{\frac{2\mu^{TF}}{m\omega^2}} x^\star$, as may be seen, the spatial coordiante can be scaled by this term. The normalization condition is now

$$\begin{aligned} 1 = \quad & \int_L |\Psi^{TF}(x)|^2 dx = \int_{-1}^{1} \frac{\mu^{TF} - \mu^{TF} x^{\star 2}}{\beta_{1D}} \frac{\sqrt{2\mu^{TF}}}{m\omega^2} dx^\star \\ = \quad & \frac{\mu^{TF}}{\beta_{1D}} \left(x^\star - \frac{x^{\star 3}}{3} \right) \Big|_{-1}^{1} \frac{\sqrt{2\mu^{TF}}}{m\omega^2} = \frac{\sqrt{2\mu^{TF}}}{m\omega^2 \beta_{1D}} \left(2 - \frac{2}{3} \right) \mu^{TF} \qquad \text{(B.6)} \\ = \quad & \frac{\sqrt{2\mu^{TF}}}{m\omega^2 \beta_{1D}} \frac{4}{3} \mu^{TF} = \frac{2}{3} \frac{\left(2\mu^{TF}\right)^{3/2}}{m\omega^2 \beta_{1D}} \\ \therefore \quad & \mu^{TF} = \frac{1}{2} \left(\frac{3m\omega^2 \beta_{1D}}{2} \right)^{2/3} \qquad \text{(B.7)} \end{aligned}$$

one finds the final expression for the chemical potential of a 1D condensate

$$\mu^{TF} = \left[\frac{9m^2 \left(\beta_{1D} \omega^4 / m \right)^2}{8 \times 4} \right]^{1/3} \tag{B.8}$$

APPENDIX C

Numerical Methods

Numerically speaking we have worked with two types of systems, these are: Time independent Gross Pitaevskii equations and the classical equations for describing the dynamics of the condensate resulting from the scaling approach.

The solution of the Gross Pitaevskii equation has been performed by applying the well-known time step split operator method (TSSO) which is an accurate and stable method by using an efficient implementation of the Fourier Transform known as Fast Fourier Transform (FFT).

From the scaling approach results a set of coupled second order partial differential equations, which is solved by using the Fourth order Runge-Kutta (RK4). In what follows, both algorithms are outlined below.

C.1 Time step Split Operator method (tsSO)

[1] The TSSO computes the Ground sate of the TDGPE at a given time by starting from the formal solution of the TDGPE, which consists in applying the time evolution operator U, defined as $U = e^{-iH\Delta t}$ on a $|\psi>$.

Where H is the Hamiltonian $H = T + V(\vec{r})$, with T defining the kinetic operator and V the potential operator which stay diagonal in momentum space and coordinates space respectively.

therefore $U = e^{-\frac{i}{\hbar}(T+V(\vec{r}))\Delta t}$. By using the Baker-Campbell-Hausdorff formula, which is a general formula for non-commuting operators, as in this case we have kinetic an potential energy operators, U is written

$$U = e^{-\frac{i}{\hbar}(T+V)\Delta t} = e^{-\frac{i}{\hbar}T\Delta t}e^{-\frac{i}{\hbar}V\Delta t}e^{-\frac{i}{\hbar}\frac{-1}{2}[T,V]\Delta t+\mathcal{O}(\Delta t^3)} \tag{C.1}$$

To simplify writing, we have omitted the spatial-dependence of V. By physical reasons, the commutator in eq.(C.1) cannot be neglected because that means to introduce an error or order $\mathcal{O}\left(\Delta t^2\right)$, and since it is computationally unfavorable, it requires additional treatment, this is carried put by splitting one of the operators (T/V) into two parts. Here it is chosen to split T. Consequently, U can be written

$$U(\Delta t) = e^{-\frac{i}{\hbar}(T+V)\Delta t} \approx e^{-\frac{i}{\hbar}\frac{1}{2}T\Delta t}e^{-\frac{i}{\hbar}V\Delta t}e^{-\frac{i}{\hbar}\frac{1}{2}T\Delta t}, \tag{C.2}$$

where some terms which have an associated error of $\mathcal{O}\left(\Delta t^3\right)$ order have been neglected. With having U more easily numerically workable, the next stage is to describe the

1 See [191]

algorithm used to compute the solution of the full TDGPE.

For the sake of simplicity, the explanation of the method is done for a 1D system, named x in coordinates space. The extension to higher dimensions is straightforward.

To calculate the U propagator, which is after projected on the wavefunction ψ, it is strictly required that the kinetic and potential operators do not couple each other, and individually they should be diagonal at any time.

The method discretizes the real space, using a grid of size L containing N sites, with a step size $\Delta x = \frac{L}{N}$, therefore the step size in momentum space is $\Delta k = \frac{2\pi}{L}$.

First of all, the propagator $e^{-\frac{i}{\hbar}\frac{1}{2}T\Delta t}\psi$ is calculated in momentum space by performing a Fourier transform and $e^{-\frac{i}{\hbar}V\Delta t}\psi$ is calculated in real space. Fourier transforms are needed between each calculation, at every time step. The procedure performed for each Δt is the following:

1. Propose a trial function in real space $\psi(x)$.
2. Fourier transform $\psi(x)$ to obtain $\psi(k)$.
3. Multiply by $e^{-\frac{i}{\hbar}\frac{\hbar^2k^2}{2m}\frac{\Delta t}{2}}$.
4. Inverse Fourier transform to real space.
5. Multiply by $e^{-\frac{i}{\hbar}V(r)\Delta t}$.
6. Fourier transform to momentum space
7. Multiply by $e^{-\frac{i}{\hbar}\frac{\hbar^2k^2}{2m}\frac{\Delta t}{2}}$.
8. Inverse Fourier transform to real space.

The TSSO method has found to be unconditionally stable [192]. The Fourier transforms hae been calculated by using the very efficient Fast Fourier Transfrom algorithm [193].

An scheme of the algorithm is as follows

$\mathcal{F}(\psi(x)) \Rightarrow \times\ e^{-i\frac{k^2}{2}\Delta t} \Rightarrow \mathcal{F}^{-1}(\psi(k)) \Rightarrow \times\ e^{-iV(x)\Delta t} \Rightarrow \mathcal{F}(\psi(x)) \Rightarrow \times\ e^{-i\frac{k^2}{2}\Delta t} \Rightarrow \mathcal{F}^{-1}(\psi(k))$

A complete calculation of any of the cases displayed in this thesis requires to firstly, calculate the GS by implementing the imaginary time propagation, or artificial time integration, and then the program is fed with this GS by doing a real-time propagation which allows for tracking the dynamics of the condensate wavefunction at any time, more details of the method can be found in [191, 194].

C.2 Fourth–order Runge-Kutta- RK4

The scaling approach 2.0.2 results in a sytem of coupled ordinary differential equations which can be numerically solved by integrating. Such integration can be carried out by using the simple and robust Fourth–order Runge-Kutta method [195].

The method is presented here for one equation, nevertheless a generalization to higher order derivatives and to a system of several coupled equations can be done straightforwardly.

Given an initial value problem [195].

$$\dot{\lambda} = f(t, \lambda), \quad \lambda(t_0) = \lambda_0 \quad \text{(initial condition)}. \tag{C.3}$$

Where λ is a function, and here is the scaling parameter, which represents, except by a multiplying factor, the dynamical variable describing the size of the expanding atomic

cloud. The parameter λ changes at a rate $\dot{\lambda}$. The function $f(t, \lambda)$ is a general given function, corresponding to the right side of eqs. C.3 which contains the trap information.

In order to solve eq.(C.3), the function λ is approximated by

$$\begin{aligned} \lambda_{n+1} &= \lambda_n + \tfrac{h}{6}\left(k_1 + 2k_2 + 2k_3 + k_4\right) \\ t_{n+1} &= t_n + h \end{aligned} \tag{C.4}$$

with h the time step $h = t_1 - t_0 \ldots = t_{n+1} - t_n$, and the coefficients k_i are found by the formulas

$$\begin{aligned} k_1 &= f(t_n, \lambda_n), \\ k_2 &= f(t_n + \tfrac{h}{2}, \lambda_n + \tfrac{h}{2}k_1), \\ k_3 &= f(t_n + \tfrac{h}{2}, \lambda_n + \tfrac{h}{2}k_2), \\ k_4 &= f(t_n + h, \lambda_n + hk_3). \end{aligned} \tag{C.5}$$

which give the RK4 approximate solution of $\lambda(t_{n+1})$, determined by adding four weighted averages C.5 to the present value λ_n. The error caused by the iteration is of the order $\mathcal{O}\left(h^5\right)$, which makes it a very accurate method.